A Virgo high-resolution Halpha kinematical survey - II. The Atlas

Laurent Chemin, Chantal Balkowski, Véronique Cayatte, Claude Carignan, Philippe Amram, Olivia Garrido, Olivier Hernandez, M. Marcelin, C. Adami, Alessandro Boselli, et al.

Mon. Not. R. Astron. Soc. **366,** 812–857 (2006) doi:10.1111/j.1365-2966.2005.09899.x

A Virgo high-resolution Hα kinematical survey – II. The Atlas

L. Chemin,[1,2]★ C. Balkowski,[2]† V. Cayatte,[3]† C. Carignan,[1]† P. Amram,[4]† O. Garrido,[2,4] O. Hernandez,[1,4]† M. Marcelin,[4]† C. Adami,[4] A. Boselli[4] and J. Boulesteix[4]

[1]*Département de Physique and Observatoire du mont Mégantic, Université de Montréal, C.P. 6128, Succ. centre-ville, Montréal, Qc, Canada H3C 3J7*
[2]*Observatoire de Paris, section Meudon, GEPI, CNRS-UMR 8111 & Université Paris 7, 5 Pl. Janssen, 92195 Meudon, France*
[3]*Observatoire de Paris, section Meudon, LUTH, CNRS-UMR 8102 & Université Paris 7, 5 Pl. Janssen, 92195 Meudon, France*
[4]*Observatoire Astronomique de Marseille Provence, 2 Pl. Le Verrier, 13248 Marseille, France*

Accepted 2005 November 15. Received 2005 November 15; in original form 2005 May 10

ABSTRACT

A catalogue of ionized gas velocity fields for a sample of 30 spiral and irregular galaxies of the Virgo cluster has been obtained by using 3D optical data. The aim of this survey is to study the influence of high-density environments on the gaseous kinematics of local cluster galaxies. Observations of the Hα line by means of Fabry–Perot interferometry have been performed at the Canada–France–Hawaii Telescope, European Southern Observatory 3.6-m telescope, Observatoire de Haute-Provence 1.93-m telescope and Observatoire du mont Mégantic telescope at angular and spectral samplings from 0.4 to 1.6 arcsec and 7 to 16 km s^{-1}. A recently developed, automatic and adaptive spatial binning technique is used to reach a nearly constant signal-to-noise ratio (S/N) over the whole field of view, allowing us to keep a high spatial resolution in high-S/N regions and extend the detection of signal in low-S/N regions. This paper is part of a series and presents the integrated emission-line and velocity maps of the galaxies. Both Hα morphologies and kinematics exhibit signs of perturbations in the form of, for example, external filaments, inner and nuclear spiral- and ring-like structures, inner kinematical twists, kinematical decoupling of a nuclear spiral, streaming motions along spiral arms and misalignment between kinematical and photometric orientation axes.

Key words: instrumentation: interferometers – techniques: high angular resolution – galaxies: clusters: individual: Virgo – galaxies: kinematics and dynamics.

1 INTRODUCTION

Dense environments such as the cores of galaxy clusters are known to give to disc galaxies photometric and spectral properties that may considerably differ from those of galaxies found in lower density environments, like the clusters periphery or the field.

Manifestations of environmental effects in local galaxy clusters are illustrated by the morphology–density relation (Dressler 1980; Binggeli, Tammann & Sandage 1987), the neutral hydrogen deficiency of spiral galaxies in the cluster core (Chamaraux, Balkowski & Gérard 1980; Giovanelli & Haynes 1985; Gavazzi 1987; Cayatte et al. 1990; Bravo-Alfaro et al. 2000), at large clustercentric distances (Solanes et al. 2001; but see Sanchis et al. 2004) or by the occurrence of peculiar Hα morphologies for spirals within the highest galaxy surface density regions (Moss & Whittle 2000; Koopmann & Kenney 2004; Vogt et al. 2004). Centres of nearby clusters are dominated by spheroidals, gas-poor, non-star-forming discs (lenticulars) and ellipticals, while lower-density regions are gas-rich, spiral-disc dominated. Many works have furthermore brought evidence that the properties of cluster spirals strongly evolve with the redshift (see Poggianti 2004, and references therein). This can be seen in the evolution of the morphology–density relation (Dressler et al. 1997; Fasano et al. 2000; Smith et al. 2005) and of galaxy colours (Butcher & Oemler 1978, 1984). Distant, intermediate redshift ($0.2 \lesssim z \lesssim 0.8$) clusters are populated by a larger number of star forming spirals rather than by passive lenticulars. These results raise the question of a possible morphological transformation of spirals into S0s since a redshift of $z \sim 0.5$ and of the evolution of the star formation activity of galaxies (e.g. Couch & Sharples 1987; Balogh et al. 1999; Dressler et al. 1999; Adami et al. 2000). An active star formation period has been rapidly quenched (e.g. Poggianti et al. 1999), leaving the star forming galaxies in a post-starburst phase, a probably important step during their possible evolution towards early-type objects (e.g. Tran et al. 2003). The population of massive elliptical galaxies does not vary as a function of redshift (Dressler

★E-mail: chemin@astro.umontreal.ca
†Visiting astronomers, Canada–France–Hawaii Telescope, Mauna Kea, Hawaii.

et al. 1997; Postman et al. 2005; Smith et al. 2005) and their formation appears to go back to the earliest epochs ($z \gtrsim 2$–3; e.g. Ellis et al. 1997; van Dokkum et al. 1998; van Dokkum & Franx 2001).

The recent theoretical works armed with *N*-body or hydrodynamical numerical simulations have furthermore considerably improved our understanding of the physical processes that could drive the evolutions of the stellar populations and the morphological properties of cluster galaxies. Among several theories, two preferred invoked processes are tidal effects and ram-pressure stripping (RPS). On one hand, simulations of tidal effects can account for a slow morphological change within a time-scale of few Gyr when a galaxy enters a cluster and undergoes several gravitational interactions with other galaxies and with the cluster tidal field. Instances of such models are the 'galaxy harassment' (Moore et al. 1996; Moore, Lake & Katz 1998; Moore et al. 1999) or the 'tidal heating' (Gnedin 2003a,b) models. In these models, low-density galaxies such as low surface brightness discs lose almost all their stars; their remnants appear to become dwarf spheroidal systems and their stripped stars the diffuse intracluster light. Galaxy mergers could participate in the formation of central giant ellipticals and cD galaxies during the earliest phase of the cluster formation (Merritt 1985; Dubinski 1998). On another hand, RPS (Gunn & Gott 1972) could explain the H I deficiency of spirals today, and perhaps why the gas reservoir has been emptied and the star formation stopped in distant spirals. Here, the hot gas of the intracluster medium (ICM) exerts a pressure on the gaseous disc of a galaxy, acting like a wind that can efficiently sweep it in several tens of Myr (Abadi, Moore & Bower 1999; Quilis, Moore & Bower 2000; Schulz & Struck 2001; Vollmer et al. 2001; Roediger & Hensler 2005). Eccentric orbits allow galaxies to go deeper through the cluster core and thus to be more efficiently stripped (Vollmer et al. 2001) and could explain the presence of H I-deficient spirals observed at large clustercentric radius (Solanes et al. 2001). Because this mechanism does not involve gravitational forces, at a first order it cannot influence the (old) stellar population of a disc. At a second order, some simulations claim that the rise of gas surface density when a disc passes close to the cluster core and the gas shocks induced by the return of expelled gas into a parent galaxy can enhance the formation of stars (e.g. Vollmer et al. 2001). This is nevertheless probably not sufficient to explain the observed morphological segregation and the two above-mentioned mechanisms may be both at work to explain the observations (Poggianti et al. 1999).

The kinematical and dynamical properties of cluster galaxies have also been the subject of several works although they have been less studied than their spectrophotometric ones. In local clusters, optical and H I rotation curves are used to study the Tully–Fisher relation of spirals (e.g. Schommer et al. 1993; Dale et al. 1997, 1999; Verheijen 2001) or the shape of the curves and its connection with the environment (e.g. Amram et al. 1993; Sperandio et al. 1995; Amram et al. 1996; Adami et al. 1999; Rubin, Waterman & Kenney 1999; Dale et al. 2001). Rubin et al. (1999) used a large sample of optical rotation curves of Virgo cluster galaxies and found that the curves harbouring the most disturbed shapes have a distribution of systemic velocities very well correlated with that of the Virgo ellipticals and are more and more frequent (relative to the regular rotation curves) as the clustercentric radius from M87 (at the cluster core) increases. Both these results suggest highly eccentric orbits for spirals (see also Adami, Biviano & Mazure 1998). Moreover, the perturbed curves are not found preferentially in H I-deficient galaxies, suggesting that the two mechanisms responsible for the deficiency and the observed kinematical disturbances differ. In distant clusters, observations of galaxies currently concentrate on the study of their Tully–Fisher relation (e.g. Ziegler et al. 2003; Bamford et al. 2005) and it is still too early to learn about any evolution as a function of redshift of their kinematical disturbances.

In this work, we are interested in studying the kinematical and dynamical properties of Virgo spiral galaxies. For that purpose a sample of 30 galaxies obtained using optical data at high angular and spectral resolutions has been observed. Typical questions that are still to be answered and that motivate our study are: how do the properties of gaseous velocity fields, their asymmetries (induced by e.g. a warp, a lopsidedness, a bar or spiral pattern) and of dark matter haloes depend on such a dense environment? Do morphologically disturbed spirals exhibit kinematical perturbations? How does the kinematics correlate with the star formation efficiency? Long-slit spectroscopy data can hardly answer these questions because they only inform us about the kinematics along a few directions (mainly the photometric major axis) and are not appropriate to investigate the full kinematical structure of spiral galaxies. The recent advent of a new generation of 3D optical spectroscopic instruments offers very promising perspectives for the stellar and/or gaseous kinematics of large samples of nearby galaxies spanning large ranges of luminosity and morphology (de Zeeuw et al. 2002; Emsellem et al. 2004; Bershady et al. 2005; Daigle et al. submitted; Hernandez et al. 2005a). These instruments are, for example, fibre-fed or lenslet array integral-field spectrographs (Bacon et al. 2001; Bershady et al. 2004) or Fabry–Perot (FP) spectroimagers (Gach et al. 2002). We want to extend the available data with a sample of gaseous velocity fields of Virgo cluster spirals using the FP interferometry technique. 3D optical data are a good compromise for the study of environmental effects in clusters due to a better distribution and resolution of the gas kinematics than for radio data. Virgo cluster spirals are indeed H I deficient, often showing H I discs smaller than the optical ones (Cayatte et al. 1990). Moreover, the neutral hydrogen often lack their central parts, regions where the molecular gas is mainly present (Sofue et al. 2003a,b). As an additional motivation to our study, the 3D observations of gas will be compared to results of *N*-body and/or hydrodynamical simulations, as already done for a few Virgo galaxies (see e.g. Vollmer et al. 2004). It could help to constrain the evolutionary scenario of peculiar objects in the cluster (e.g. RPS, encounters of galaxies).

This article is the second from a series. The first paper was dedicated to NGC 4438, a prototype of a galaxy interacting with the ICM and with companions (Chemin et al. 2005). This article presents a catalogue of 2D Hα emission-line and kinematical maps for 30 Virgo galaxies observed with the Cigale and FaNTOmM[1] instruments. The article presents the sample of the galaxies, the principles of the data reduction and of the adaptive binning in Sections 2 and 3. Sections 4 and 5 briefly present the results and a discussion. Section 6 resumes the results presented in the article. Comments for the individual galaxies are given in Section A1 and their kinematics is presented in Section A2 of Appendix A.

The data can be obtained from the authors upon request.

2 DEFINITION OF THE SAMPLE

The Virgo cluster of galaxies is the nearest cluster from the Milky Way ($D \sim 16$ Mpc) and is therefore very well appropriate to

[1] Fabry–Perot de Nouvelle Technologie de l'Observatoire du mont Mégantic. See http://www.astro.umontreal.ca/fantomm.

Table 1. Virgo galaxy targets parameters.

VCC (1)	NGC-IC (2)	Messier (3)	α_{2000} (4)	δ_{2000} (5)	Type (6)	B_t^0 (7)	v_{sys} (8)	Distance to M87 (9)	Membership (10)	H I deficiency (11)
0089	NGC 4189		$12^h13^m47\overset{s}{.}3$	$+13°25'29''$	SAB(rs)cd?	12.21	2115	$4\overset{\circ}{.}4$	M	−0.03
0157	NGC 4212		$12^h15^m39\overset{s}{.}3$	$+13°54'05''$	SAc	11.35	−81	$4\overset{\circ}{.}1$	N	0.61
0226	NGC 4237		$12^h17^m09\overset{s}{.}4$	$+15°19'33''$	SAB(rs)bc	12.18	867	$4\overset{\circ}{.}5$	N	0.48
0307	NGC 4254	M99	$12^h18^m49\overset{s}{.}6$	$+14°24'59''$	SA(s)c	10.10	2407	$3\overset{\circ}{.}6$	N	0.01
0465	NGC 4294		$12^h21^m17\overset{s}{.}8$	$+11°30'40''$	SB(s)cd	11.83	359	$2\overset{\circ}{.}5$	N	0.10
0483	NGC 4298		$12^h21^m32\overset{s}{.}8$	$+14°36'22''$	SA(rs)c	11.62	1135	$3\overset{\circ}{.}2$	A	0.34
0567	IC 3225		$12^h22^m39\overset{s}{.}1$	$+06°40'42''$	Sdm:	13.87	2363	$6\overset{\circ}{.}1$	B	0.36
0596	NGC 4321	M100	$12^h22^m54\overset{s}{.}9$	$+15°49'21''$	SAB(s)bc	9.98	1571	$4\overset{\circ}{.}0$	A	0.53
0692	NGC 4351		$12^h24^m01\overset{s}{.}5$	$+12°12'18''$	SB(rs)ab pec:	12.79	2310	$1\overset{\circ}{.}7$	A	0.66
0874	NGC 4405		$12^h26^m07\overset{s}{.}1$	$+16°10'51''$	SA(rs)0/a:	12.83	1747	$4\overset{\circ}{.}0$	A	0.95
1043	NGC 4438		$12^h27^m45\overset{s}{.}6$	$+13°00'32''$	SA(s)0/a pec:	10.49	71	$1\overset{\circ}{.}0$	A	1.33[a]
1110	NGC 4450		$12^h28^m29\overset{s}{.}6$	$+17°05'06''$	SA(s)ab	10.75	1954	$4\overset{\circ}{.}7$	A	0.95
1145	NGC 4457		$12^h28^m59\overset{s}{.}0$	$+03°34'14''$	(R)SAB(s)0/a	11.55	882	$8\overset{\circ}{.}8$	S	0.86
1379	NGC 4498		$12^h31^m39\overset{s}{.}5$	$+16°51'10''$	SAB(s)d	12.33	1507	$4\overset{\circ}{.}5$	A	0.15
1401	NGC 4501	M88	$12^h31^m59\overset{s}{.}2$	$+14°\ 25'14''$	SA(rs)b	9.86	2281	$2\overset{\circ}{.}1$	A	0.55
1508	NGC 4519		$12^h33^m30\overset{s}{.}3$	$+08°39'16''$	SB(rs)d	12.15	1220	$3\overset{\circ}{.}8$	S	−0.26
1554	NGC 4532		$12^h34^m19\overset{s}{.}3$	$+06°28'04''$	IBm	11.92	2012	$6\overset{\circ}{.}0$	S	−0.37
1555	NGC 4535		$12^h34^m20\overset{s}{.}3$	$+08°11'52''$	SAB(s)c	10.32	1961	$4\overset{\circ}{.}3$	S	0.19
1562	NGC 4536		$12^h34^m27\overset{s}{.}1$	$+02°11'16''$	SAB(rs)bc	10.58	1808	$10\overset{\circ}{.}2$	S	0.15
1615	NGC 4548	M91	$12^h35^m26\overset{s}{.}4$	$+14°29'47''$	SBb(rs)	10.79	486	$2\overset{\circ}{.}4$	A	0.80
1673	NGC 4567		$12^h36^m32\overset{s}{.}7$	$+11°15'28''$	SA(rs)bc	11.79	2274	$1\overset{\circ}{.}8$	A	0.43
1676	NGC 4568		$12^h36^m34\overset{s}{.}3$	$+11°14'19''$	SA(rs)bc	11.18	2255	$1\overset{\circ}{.}8$	A	0.58
1686	IC 3583		$12^h36^m43\overset{s}{.}5$	$+13°15'34''$	Sm	13.24	1121	$1\overset{\circ}{.}7$	A	0.79
1690	NGC 4569	M90	$12^h36^m49\overset{s}{.}8$	$+13°\ 09'46''$	SAB(rs)ab	9.79	−235	$1\overset{\circ}{.}7$	A	1.07
1696	NGC 4571		$12^h36^m56\overset{s}{.}4$	$+14°13'03''$	SA(r)d	11.73	342	$2\overset{\circ}{.}4$	A	0.54
1727	NGC 4579	M58	$12^h37^m43\overset{s}{.}6$	$+11°49'05''$	SAB(rs)b	10.29	1519	$1\overset{\circ}{.}8$	A	0.83
1730	NGC 4580		$12^h37^m48\overset{s}{.}4$	$+05°22'06''$	SAB(rs)a pec	12.49	1034	$7\overset{\circ}{.}2$	S	1.03
1943	NGC 4639		$12^h42^m52\overset{s}{.}4$	$+13°15'27''$	SAB(rs)bc	11.85	1010	$3\overset{\circ}{.}1$	E	0.25
1987	NGC 4654		$12^h43^m56\overset{s}{.}6$	$+13°07'35''$	SAB(rs)cd	10.75	1037	$3\overset{\circ}{.}4$	E	−0.29
2058	NGC 4689		$12^h47^m45\overset{s}{.}5$	$+13°45'46''$	SA(rs)bc	11.39	1616	$4\overset{\circ}{.}5$	E	0.90

Notes on columns: (1–3) Galaxy VCC, NGC-IC and Messier names; (4–5) RA and declination (Dec.) (J2000); (6) morphological type, from RC3 (de Vaucouleurs et al. 1991); (7) total *B*-band magnitude, from RC3; (8) systemic velocity (in km s^{-1}), from LEDA (Paturel et al. 1991); (9) projected distance to M87 (in degrees); (10) revised region of membership, as defined in Gavazzi et al. (1999) (A = cluster A, B = cluster B, E = East cloud, M = M cloud, N = North cloud, S = southern extension); (11) H I deficiency parameter from Gavazzi et al. (2005). [a] The value is uncertain for NGC 4438 due to uncertainties on its morphology and optical diameter.

observe in details the galaxy properties. The Virgo Cluster Catalogue (hereafter VCC, Binggeli, Sandage & Tammann 1985; Binggeli, Popescu & Tammann 1993) counts ∼1400 members with a dominating population of dwarf ellipticals. The cluster is not yet relaxed, as shown by the presence of irregular structures in either kinematical or X-ray data (Binggeli et al. 1987; Böhringer et al. 1994; Shibata et al. 2001). The 3D structure of the cluster is very particular (see e.g. Gavazzi et al. 1999), articulated around a main substructure centred on Messier 87 (cluster A) and with several extensions.

The selection criterion was to observe targets among the brightest spiral galaxies of the cluster. This turns out to select objects having a total magnitude in the *B* band brighter than $B_t^0 = 12$. Other galaxies were observed because of their presumably perturbed major-axis kinematics, as derived from long-slit spectroscopy (Rubin et al. 1999), their peculiar morphology (e.g. IC 3225) or their membership within a galaxy pair (e.g. IC 3583). A concern was to specifically observe galaxies in the inclination range between 25° and 80° (with the exception of NGC 4438) in order to avoid problems of disc opacity at optical wavelength for high inclinations and of determination of the circular velocities for low inclinations. The FP catalogue is composed of 30 galaxies whose locations are shown on Fig. 2 and properties given in Table 1. The morphological types of the targets are distributed through three S0/a, one Sa, three Sab, three Sb, seven Sbc, four Sc, three Scd, three Sd, one Sdm, one Sm and one Im galaxies. The targets are mainly located in the cluster core where environmental effects are supposed to be more important, but also in the cluster extension towards M49. Deep Hα imagery is available for all galaxies from this sample (Koopmann, Kenney & Young 2001; Boselli & Gavazzi 2002; Boselli et al. 2002; Gavazzi et al. 2002, 2003).

Optical kinematical data for many individual objects or larger samples of Virgo galaxies have been presented in the past using long-slit spectroscopy of the Hα and [N II] emission lines (e.g. Chincarini & de Souza 1985; Distefano et al. 1990; Sperandio et al. 1995; Rubin et al. 1999; Yoshida et al. 2004). Except for few individual galaxies (e.g. NGC 4254, Phookun, Vogel & Mundy 1993; NGC 4321, Arsenault, Roy & Boulesteix 1990; Knapen et al. 1995; Canzian & Allen 1997; NGC 4522, Vollmer et al. 2000), the mapping of the 2D optical kinematics for several Virgo galaxies has never been done before this study. The kinematics of the molecular and neutral atomic gas have nevertheless already been mapped at millimetre and centimetre wavelengths. The FP catalogue has 10 galaxies in common with the Virgo CO Survey catalogue of (NGC 4212, 4254, 4501, 4535, 4536, 4548, 4569, 4579, 4654 and 4689; Sofue et al. 2003a,b), six with the Berkeley–Illinois–Maryland Association Survey of Nearby Galaxies CO catalogue

Table 2. Telescope and Instrument configuration.

Telescope	Detector	FOV (arcmin)	Detector sampling	Pixel Size (arcsec)
A – OmM (1.60 m)	FaNTOmM	13.7	512 × 512	1.61
B1 – OHP (1.93 m)	Cigale	4.1	256 × 256	0.96
B2 – OHP (1.93 m)	Cigale	5.8	512 × 512	0.68
C1 – CFHT (3.60 m)	FaNTOmM	4.2	512 × 512	0.49
C2 – CFHT (3.60 m)	MOS/FP	4.9	512 × 512	0.57
D – ESO (3.60 m)	FaNTOmM	3.6	512 × 512	0.42

(NGC 4321, 4450, 4535, 4548, 4569 and 4579; Helfer et al. 2003), 15 with the H I catalogue (NGC 4237, 4254, 4321, 4438, 4450, 4501, 4535, 4548, 4567, 4568, 4569, 4579, 4639, 4654 and 4689; Guhathakurta et al. 1988; Cayatte et al. 1990, 1994) and other works like the one and 2D H I data presented in Warmels (1988a,b,c). All of these will allow a comparison of the kinematics of the different gaseous components.

One has to note that not all galaxies of the sample lie at the same distance from us. For instance, accurate estimates based on the observations of Cepheid variable stars put NGC 4535 at a distance of 16.0±1.9 Mpc (Macri et al. 1999) and NGC 4639 at 25.5 ± 2.5 Mpc (Saha et al. 1997). The 3D structure of the Virgo cluster has often been studied (Yasuda, Fukugita & Okamura 1997; Gavazzi et al. 1999; Fouqué et al. 2001; Solanes et al. 2002) but is neglected here and for simplicity reasons it is assumed a distance of 16 Mpc for the cluster and all its galaxies. Therefore, 1 arcsec on the sky corresponds to ∼78 pc at this distance.

3 OBSERVATIONS AND DATA REDUCTION

3.1 Data acquisition

The observations of the 30 galaxies were performed from 1999 to 2005 at the European Southern Observatory (ESO) 3.6-m telescope (Chile), the 3.6-m Canada–France–Hawaii Telescope (CFHT, Hawaii), the 1.93-m Observatoire de Haute-Provence telescope (OHP, France) and the 1.6-m Observatoire du mont Mégantic telescope (OmM, Québec, Canada). Each of our visitor instruments, FaNTOmM (at ESO, CFHT and OmM) and Cigale (at OHP) is a package including a scanning FP interferometer, a series of interference filters and an image photon counting system (IPCS) based on a technology of GaAs amplifier tube having a high sensitivity and a quantum efficiency of ∼28 per cent (Gach et al. 2002; Hernandez et al. 2003). Our focal reducer (named *Cigale* at ESO and OHP, *MOS/FP* at CFHT, *Panoramix*) is attached at the Cassegrain focus of the telescopes and is equipped with our visitor instrument. Tables 2 and 3 give the observational set-up at each telescope and parameters of each galaxy (respectively). Among the 30 galaxies,

Table 3. Observational parameters.

Galaxy	Set-up (1)	Date (2)	p (3)	λ_s (4)	λ_f (5)	FWHM$_f$ (6)	FSR (7)	nb_{ch} (8)	t_{exp} (9)	t (10)	Seeing (11)
NGC 4189	B2	07-03-03	793	6609.08	6612	11	380.71	24	5.0	120.0	⋆
NGC 4212	B2	27-05-01	793	6561.01	6561	12	377.95	24	3.7	88.8	⋆
NGC 4237	B2	10-03-03	793	6581.76	6582	11	379.14	24	5.2	124.8	⋆
NGC 4254	A	14-02-05	765	6615.47	6621	18	395.03	48	5.0	240.0	⋆
NGC 4294	C1	07-04-03	899	6570.64	6575	20	333.87	48	2.5	120.0	⋆⋆
NGC 4298	D	06-04-02	793	6587.63	6589	12	379.48	24	2.3	55.2	⋆⋆
IC 3225	D	04-04-02	609	6614.51	6617	11	496.15	40	2.3	92.0	⋆⋆
NGC 4321	A	25-02-03	899	6597.17	6605	15	335.22	52	5.0	260.0	⋆
NGC 4351	B2	27-04-03	793	6613.35	6614	11	380.96	24	4.5	108.0	⋆
NGC 4405	B2	28-04-03	793	6601.02	6602	12	380.25	24	4.5	108.0	⋆
NGC 4438	D	06-04-02	793	6564.33	6568	12	378.14	24	6.5	156.0	⋆⋆
NGC 4450	D	07-04-02	793	6605.56	6607	12	380.51	24	2.5	60.0	⋆⋆
NGC 4457	B2	10-03-03	793	6582.09	6582	11	379.16	24	5.2	124.8	⋆
NGC 4498	B1	03-03-00	793	6595.77	6593	10	379.95	24	3.2	76.8	⋆
NGC 4501	B1	10-03-00	793	6612.71	6614	11	380.93	24	4.8	115.2	⋆
NGC 4519	C1	04-04-03	899	6589.49	6595	18	334.83	48	2.0	96.0	⋆⋆
NGC 4532	D	05-04-02	793	6606.82	6607	12	380.59	24	2.0	48.0	⋆⋆
NGC 4535	A	06-03-03	899	6605.71	6617	15	335.66	52	3.0	156.0	⋆
NGC 4536	A	14-03-04	765	6602.36	6595	18	394.25	48	3.4	163.2	⋆
NGC 4548	A	07-03-03	899	6573.42	6585	16	334.01	52	2.1	109.2	⋆
NGC 4567	B1	12-04-99	793	6612.56	6614	11	380.92	24	5.0	120.0	⋆
NGC 4568	B1	12-04-99	793	6612.56	6614	11	380.92	24	5.0	120.0	⋆
IC 3583	D	05-04-02	793	6587.32	6588	11	379.46	24	5.0	120.0	⋆⋆
NGC 4569	A	11-03-02	765	6557.64	6569	15	391.58	40	3.8	152.0	⋆
NGC 4571	B1	08-03-00	793	6570.27	6574	12	378.48	24	5.0	120.0	⋆
NGC 4579	D	04-04-02	609	6596.03	6598	10	494.76	40	2.3	92.0	⋆⋆
NGC 4580	B2	08-03-03	793	6585.42	6584	12	379.35	24	5.5	132.0	⋆
NGC 4639	D	05-04-02	793	6584.89	6588	11	379.32	24	3.3	79.2	⋆⋆
NGC 4654	C2	13-02-02	1162	6585.48	6588	11	258.89	24	2.5	60.0	⋆⋆
NGC 4689	A	03-03-03	899	6598.16	6595	18	335.27	52	3.2	166.4	⋆

Notes on columns: (1) observing configuration – see Table 2 for details on the telescope and instrument used during the observations; (2) date of observation (DD-MM-YY); (3) interference order (at the Hα wavelength); (4) scanning wavelength (Å); (5–6) interference filter central wavelength and FWHM (in Å, at the ambient temperature); (7) free Spectral range (at the scanning wavelength, in km s^{-1}); (8) number of channels; (9) total exposure time per channel (in min); (10) total scanning exposure time (in min); (11) ⋆⋆ is for a seeing $<$1.5 arcsec, ⋆ for a seeing $\gtrsim$2.0 and $\lesssim$4.0 arcsec.

NGC 4654 is the only one that has not been observed with an IPCS but with the CCD detector of the MOS/FP module at CFHT.

To reconstruct a spectral profile in a spatial pixel during an exposure, the spectral range (hereafter referred as FSR for free spectral range) of a FP interferometer is scanned through a number of channels (nb_{ch}). This number must satisfy the Nyquist criteria, $nb_{ch} \gtrsim 2 \times F$, where F is the interferometer finesse. The finesse is related to the resolving power R of the interferometer by $R = p_s \times F$, where p_s is the interference order at the scanning wavelength (λ_s). The spectral range at λ_s is given by FSR $= \lambda_s / p_s$ (in Å) or FSR $= c/p_s$ (in km s^{-1}), where c is the speed of the light. Columns 3, 7 and 8 of Table 3 give the interference order (at Hα), the FSR (at λ_s) and the number of channels of the observations. At the Hα wavelength, the finesses of the four used interferometers with interference orders of $p = 609$, 765, 793, 899 and 1162 are between ∼10 and 23. This leads to resolving powers and spectral resolutions ranging between ∼7950 and 0.83 Å ($p = 793$ interferometer) and 21 000 or 0.31 Å ($p = 899$ interferometer). As a comparison, the resolution of long-slit spectroscopy observations (Rubin et al. 1999) is of the order of 1 Å.

During an integration, each channel is scanned many times within a typical time of 15 s. When the sky transparency is not excellent prior to an exposure, the integration time is set to 10 s per channel in order to average more efficiently the effects of transparency changes. The important time for an FP observation is the total exposure time of a spectral sampling element, i.e. the total integration time of one channel (t_{exp}, column 9 of Table 3). The average overall integration time of the whole sample is 3.8 min per channel. The longest times are spent for galaxies observed at the smaller telescopes and for an object like NGC 4438, which has a very low surface brightness, diffuse and filamentary Hα morphology. To ensure an optimal wavelength calibration, a reference data cube of a neon emission line ($\lambda = 6598.95$ Å) is obtained before and after the observation of a galaxy.

3.2 Data reduction

The FP data were all reduced following a homogeneous procedure which proceeds as follows: integration and wavelength calibration of the raw data cube, spectral smoothing (Hanning filtering) of the wavelength-calibrated data cube, night-sky emission lines (hereafter NSEL, generally OH lines) subtraction, signal-to-noise ratio (S/N) treatment of the pixels and computation of the Hα integrated emission and velocity maps. The λ calibration is done relatively to the above-mentioned neon emission line. Notice that no flux calibration of the data cubes is done.

We refer to other papers for a more detailed description of the wavelength calibration (e.g. Laval et al. 1987; Amram 1991). The reduction package consists of IDL[2] routines that were adapted and improved from the ADHOCW software (Boulesteix 1993). The major improvements are for the sky subtraction and the S/N treatment procedures which are explained in detail and illustrated in Daigle et al. (submitted). A brief summary of these major implementations for our data reduction follows.

3.2.1 NSEL subtraction

The often-used sky subtraction method of the ADHOCW software consists in modelling a *single NSEL average profile* which is extracted from field of view (FOV) areas free from galaxy emission and removed from the observation. Instead of this 'classical' NSEL subtraction method, the new procedure constructs an *NSEL data cube* which is fitted to the whole FOV and then subtracted from the observed data cube. Modelling the sky emission for each pixel instead of a unique pixel model reduces the NSEL residuals and thus allows a better detection of galaxy emission in low surface brightness regions (e.g. interarm, external regions, etc.). Notice that if the sky model fit cannot converge to an adequate solution, which can happen when there are two competing NSELs or when the galaxy emission covers a very large majority of the FOV, the 'classical' method is used. This has been done, for example, for NGC 4438 and 4579.

3.2.2 Data cube S/N treatment

An adaptive spatial binning is used in order to increase the S/N of the data, instead of the often-used Gaussian smoothing. For that purpose IDL routines were adapted to our FP data from existing routines developed by Cappellari & Copin (2003) for the SAURON data (de Zeeuw et al. 2002). The method is a Voronoi tessellation and basically consists in spatially binning pixels with their neighbouring pixels until a bin with sufficient S/N is obtained. Consequently, in regions of initial high-S/N (H II regions in the spiral arms, in the disc, in the Galactic Centre, etc.), no spatial binning (or a minimum binning) is done and the angular resolution is kept maximal in these regions, contrary to the Gaussian smoothing method. On another hand, because the binning occurs for pixels having a S/N lower than the target S/N value (low surface brightness and diffuse gas in interarm or outermost regions, etc.), it allows to recover the spectral information over a larger part of a FOV than the Gaussian smoothing method. The data presented here have a minimum S/N of 5 over the FOV. An example of a binned velocity field is shown for the galaxy NGC 4254 in Fig. 1 with spectra of bins (having different sizes) selected at some locations inside and outside the disc.

For three galaxies (NGC 4405, 4438 and 4569), a Gaussian filtering of 3 × 3 pixel full width at half-maximum (FWHM) (3 × 3 and 6 × 6 pixel for NGC 4438) was used instead of the Voronoi

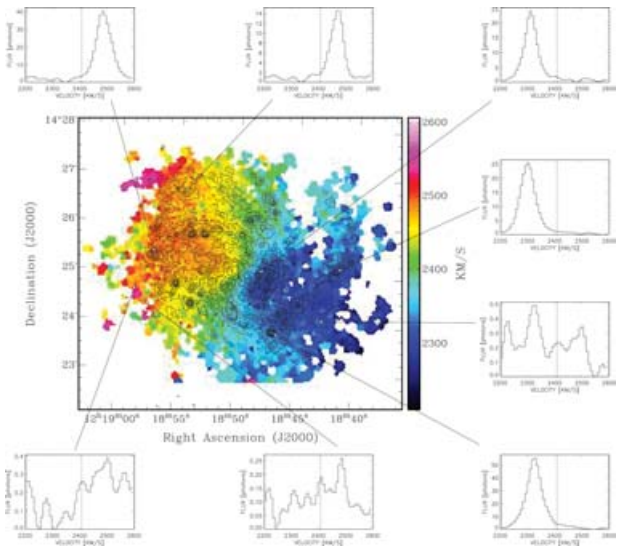

Figure 1. Hα binned velocity field of NGC 4254 obtained by the Voronoi tessellation. The contours represent the Hα integrated emission of the galaxy. For each spectra, a dashed line corresponds to the systemic velocity of NGC 4254.

[2] http://www.rsinc.com

tessellation because the solution of this new procedure was not optimal for them. It can happen when the binning is done on an NSEL residual (and so not on the Hα line of the galaxy) in extremely low surface brightness regions (e.g. filaments of NGC 4438, external arm of NGC 4569).

The CCD data of NGC 4654 had two additional pre-processing procedures. Indeed, the CCD data require a cosmic ray hits subtraction and a photometric correction, procedures which are not yet implemented in our IDL routines. Because each channel is scanned only one time during a CCD exposure with an integration of several minutes per channel, significant sky transparency variations can occur during an exposure and a photometric correction to the data is needed to take into account the sky flux changes. This problem does not exist with an IPCS because each channel is quickly scanned several times during an exposure so that the transparency variations are averaged from the beginning to the end of the overall integration. For the CCD observation of NGC 4654, the cosmic ray hits were removed and a photometric correction was applied to the raw data cube as explained in Boulesteix (1993) before the wavelength calibration.

The final steps of the data reduction consists in integrating the flux under the Hα emission line, deriving its barycentre, dispersion and underlying continuum level following the method described in Daigle et al. (submitted). We are finally left with an integrated Hα emission-line map and an Hα velocity field. All radial velocities presented in this article are given in the heliocentric rest frame and are not absolute values. Notice that no systemic velocities are given in this article; their values which do not present any particular interest for this study are generally in very good agreement with the referred ones (column 8 of Table 1) within less than 15 km s^{-1}.

Regions of galaxies that exhibit several emission lines in their profiles have their velocity fixed to the one of the highest intensity component (e.g. NGC 4438, Chemin et al. 2005). Multiple spectral components are often found in interacting systems (Amram et al. 2004; Rampazzo et al. 2005). The FP continuum map roughly traces the underlying stellar continuum of the Hα line. It is not as deep or accurate as broad *R*-band images because it is integrated over ∼5–10 Å. The FP continuum images have actually very little interest. For this reason, no continuum images are proposed in the article. Their use only concerns the recovery of the data astrometry (see Section 3.3).

3.3 Data astrometry

No reference to the World Coordinate System (WCS) have been obtained during the observations. It is important to know how a data cube is oriented in order to derive the major-axis position angle (hereafter PA) of a disc and the astrometric solution has to be found for the FP data. The koords task in the KARMA package (Gooch 1996) is used to recover it, using a *R*-band map and a FP underlying continuum map as reference and target images, respectively. The task provides a reference pixel, its angular size on the sky plane and a possible rotation angle to align the FOV with the WCS axes. All the FP images presented in Section A2 have their vertical axes aligned with the North. The original FP FOV is very well oriented with the WCS. The orientation angle of the FP FOV vertical axis to the North is lower than 0.5°. The worst misalignments reach ∼2° and are for nine galaxies observed at OmM and OHP. The values of PAs of major axis given in Table 4 have been corrected of such strong misalignments.

Table 4. Virgo galaxy targets parameters.

Galaxy	PA_p (1)	i_p (2)	PA_k (3)	i_k (4)	Offset (5)	(6)
NGC 4189	265	45	251 ± 6	(31 ± 6)	4.3	335
NGC 4212	255	53	259 ± 2	49 ± 6	1.3	101
NGC 4237	108	51	106 ± 2	53 ± 3	2.0	156
NGC 4254	45	28	69 ± 3	31 ± 6	5.2	406
NGC 4294	335	71	335 ± 3	68 ± 6	4.1	320
NGC 4298	320	58	316 ± 3	58 ± 3	1.6	125
IC 3225	213	75	215 ± 4	(70 ± 12)	2.7	211
NGC 4321	153	32	151 ± 3	38 ± 7	6.6	515
NGC 4351	80	49	73 ± 5	(39 ± 54)	2.6	203
NGC 4405	200	54	199 ± 3	57 ± 6	2.2	172
NGC 4450	355	43	351 ± 7	(49 ± 17)	3.6	281
NGC 4457	82	34	88 ± 22	(27 ± 19)	6.1	476
NGC 4498	133	59	136 ± 4	63 ± 4	7.7	601
NGC 4501	140	59	141 ± 2	58 ± 6	4.3	335
NGC 4519	325	40	357 ± 4	40 ± 5	7.3	569
NGC 4532	340	64	355 ± 6	(63 ± 14)	10.3	803
NGC 4535	180	46	180 ± 2	38 ± 10	2.2	172
NGC 4536	310	67	301 ± 2	68 ± 3	9.6	749
NGC 4567	85	49	90 ± 1	53 ± 4	2.7	211
NGC 4568	23	67	27 ± 3	67 ± 3	2.2	172
IC 3583	180	72	178 ± 5	(77 ± 11)	4.4	343
NGC 4569	23.5	65	23 ± 4	67 ± 5	4.0	312
NGC 4571	220	28	220 ± 4	(37 ± 17)	3.2	252
NGC 4579	95	38	91 ± 3	44 ± 8	1.8	140
NGC 4580	165	40	157 ± 3	46 ± 10	0.9	70
NGC 4639	304	49	311 ± 2	48 ± 6	2.4	187
NGC 4654	128	57	125 ± 2	62 ± 7	2.4	187
NGC 4689	163	36	165 ± 2	(36 ± 14)	2.1	164

Notes on columns: (1–2) photometric position angle PA_p and inclination i_p (in degrees) – taken from Rubin et al. (1999), LEDA, UGC; (3–4) kinematical position angle PA_k and inclination i_k (in degrees) (numbers in parentheses indicate that the kinematical inclination has not been chosen to obtain the rotation curve but the photometric value); (5–6) sky-projected offset between the photometric and kinematical centres (in arcsec and parsec, respectively).

4 RESULTS

4.1 Hα emission line and kinematical maps

Fig. 2 gives a global representation of all 30 velocity fields from this sample positioned at the location of galaxies in the Virgo cluster. Section A1 presents a brief description of the observed kinematics for the galaxies of the sample. Section A2 presents their Hα emission line and kinematical maps.

The catalogue is arranged with increasing order of right ascension (RA). For each galaxy, four images are displayed: a *B*-band image (top left-hand panel), a *H*-band image (top right-hand panel), the FP Hα integrated map (middle left-hand panel) and the corresponding Hα velocity field (middle right-hand panel). The *B*- and *H*-band images are taken from the GOLDMine archive (Gavazzi et al. 2003). For IC 3225, the *H*-band image is obtained from the two-Micron All Sky Survey (2MASS) archive (Jarrett et al. 2000). All four maps are WCS oriented and have the same FOV. The scales of the four images are chosen so that both the large-scale stellar morphology and Hα distribution and kinematics are displayed with great detail, with the noticeable exception of NGC 4438. The position–velocity (PV) diagrams are also displayed, using the derived rotation curve projected on to the sky plane (solid line). The data cube slice has a width of 3–4 pixel. No PV diagrams are presented for NGC 4438

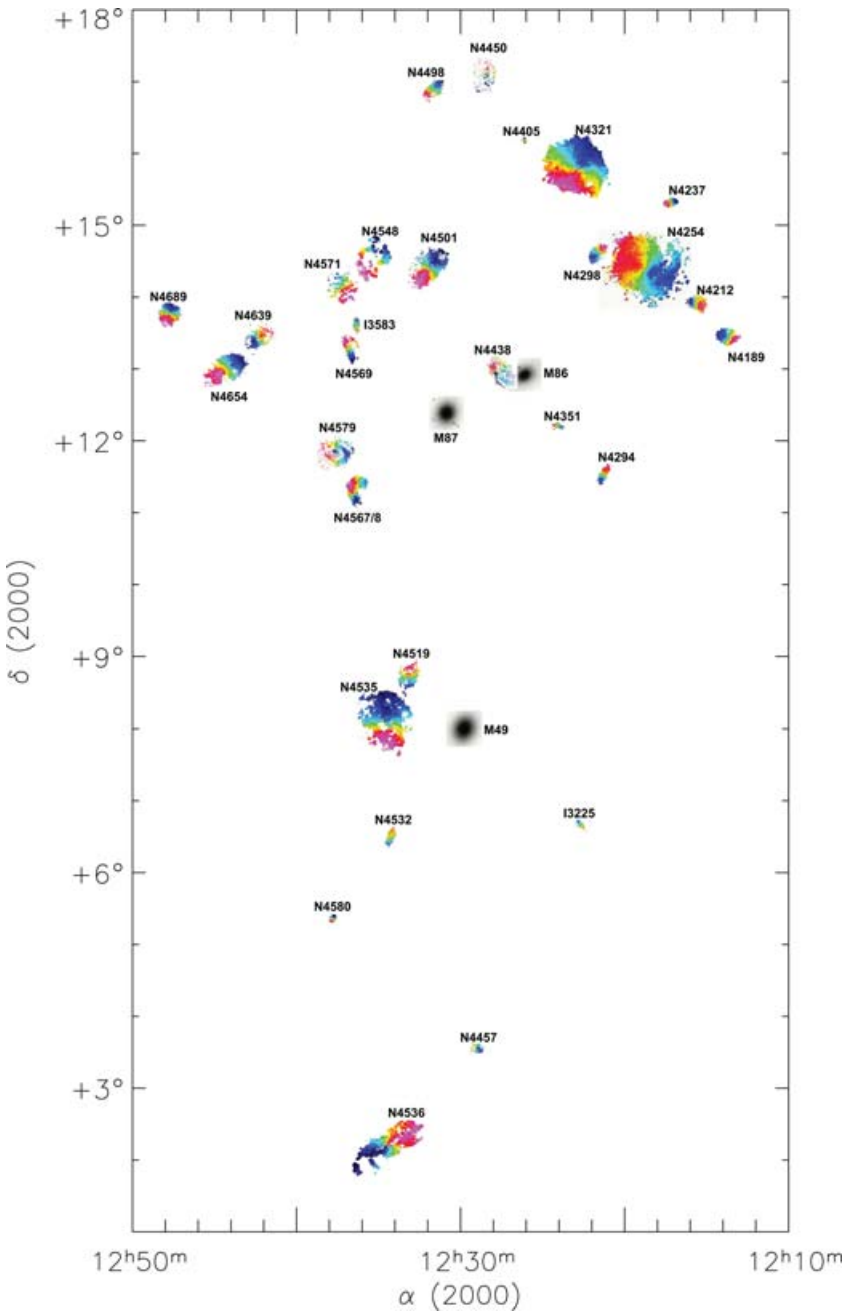

Figure 2. A global view of the Virgo cluster galaxy velocity fields map. For clarity reasons, the angular scale of each galaxy has been enlarged by a factor of ∼9.5 with respect to the real scale. The locations of the three ellipticals M49, M86 and M87 are displayed using broad-band optical images. The colour scale is blue-darker shades (red-lighter shades) for the approaching (receding) side of galaxies. See Section A2 for the velocity scale of each object.

and 4548 for the reasons exposed in Section 4.3. A constant value of PA is adopted for NGC 4457, 4501 and 4579 despite the fact their kinematical PA appeared to vary with radius (see Section 4.3).

Preliminary results for IC 3225, IC 3583, NGC 4298, 4450, 4532, 4569, 4579 and 4639 have been presented in Chemin (2003) and detailed results for NGC 4438 in Chemin et al. (2005). This catalogue presents the first optical kinematical data ever obtained for the galaxies IC 3225, IC 3583, NGC 4405 and 4457. Forthcoming papers from this series will detail more quantitatively results on the whole sample and on individual galaxies.

The FP emission line maps are in agreement with the deep Hα images presented in Koopmann et al. (2001) and in the GOLDMine data base (Gavazzi et al. 2003). The discs have morphological perturbations such as nuclear spiral (NGC 4579), nuclear, inner and outer pseudo-ring (NGC 4321, 4639), off-plane diffuse filaments, arc-like structure and giant H II regions (NGC 4438, 4532, 4569), highly truncated Hα discs (NGC 4405, 4569 and 4580), lopsidedness (e.g. IC 3225, NGC 4298 and 4654), $m = 2$ modes such as a bar or two spiral arms, more complex spiral structure (NGC 4254, 4535 and 4654). The signatures of kinematical perturbations are observed

in the velocity fields in the form of streaming motions along spiral arms or pseudo-ring (e.g. NGC 4254, 4294, 4321, 4639, 4654 and 4689), steep velocity gradients along a bar or a nuclear structure (e.g. NGC 4519, 4536 and 4579), Z shape of the velocities due to the presence of a bar (e.g. NGC 4519, 4532 and 4654), decoupled nuclear spiral (NGC 4579), twist of the kinematical major axis (e.g. NGC 4501) or misalignment between photometric and kinematical major axes (NGC 4254 and 4519), solid-body rise of the velocity in truncated discs. Another (more subtle) perturbation is a kinematical lopsidedness that is only revealed by an in-depth study of the velocity fields with titled-ring models and a harmonic decomposition (see Fig. 5 and Section 5.2). All these perturbations are probably responsible for the observed irregularities of long-slit rotation curves (Rubin et al. 1999).

4.2 Kinematical parameters fitting

An important step of the pre-analysis is to determine the location of the kinematical centre, the orientation parameters of a Galactic disc (its inclination i and angle of the major axis PA) and the recession velocity $v_{\rm sys}$ of the disc from a kinematical map. Except for the inclination that is only a scalefactor of the rotation curve and $v_{\rm sys}$, all the parameters are supposed to be known *before an observation* in long-slit spectroscopy studies. The kinematical and photometric major axes are indeed supposed to be exactly the same and have a constant orientation across the galaxy, allowing the alignment of the slit with the photometric major axis of a disc in order to derive its rotation curve. The dynamical centre is furthermore supposed to be at the location of the photometric one. It will be shown in Section 4.3 that these arguments sometimes do not hold and can lead to significant velocity (and thus mass) discrepancies with respect to the reality.

There are several ways to derive a rotation curve $V_{\rm rot}$ from a velocity field. There are some studies that fit by eye the parameters to the velocity field with efforts to lower the visual difference between the rotation curves of the receding and approaching halves of a disc (e.g. Garrido et al. 2002). They also do not permit any variation of the parameters as a function of radius.

In this work, it is decided to use a more robust, rigorous and automatic fitting routine that fully uses the power of 2D maps and with a minimum of human intervention. We use the rotcur task (Begeman 1987, 1989) of the GIPSY package (van der Hulst et al. 1992). It considers purely axisymmetric motions by fitting the formula $v_{\rm obs} = v_{\rm sys} + V_{\rm rot}\sin(i)\cos(\theta) + V_{\rm rad}\sin(i)\sin(\theta)$ to the observed velocity fields. $V_{\rm rot}$ and $V_{\rm rad}$ are the circular and radial velocities in the galaxy plane. The terms θ, i, $v_{\rm obs}$ and $v_{\rm sys}$ refer to the azimuthal angle in the galaxy plane, the disc inclination, the observed line-of-sight and systemic velocities (respectively). The radial velocity is very frequently not fitted in a velocity field (e.g. Rogstad, Lockart & Wright 1974; Bosma 1981; Begeman 1989; Carignan & Beaulieu 1989; van der Hulst et al. 1993; de Blok et al. 1996; Verheijen 2001) because it is considered very negligible with respect to the rotational term. Using a sample of eight spiral galaxies observed in CO and H I, Wong, Blitz & Bosma (2004) estimate that radial motions of inflow or outflow only reach an upper limit of 3–5 per cent of the circular velocity in only three velocity fields from their sample. It is therefore chosen here to neglect the $V_{\rm rad}$ term during the fittings. The parameters to be adjusted as a function of radius are the coordinates of the centre of mass, $v_{\rm sys}$, i and the PA of the major axis. This latter is the counterclockwise angle that the semimajor axis of the receding half does with the North axis. A good sampling of a ring implies its width to be set to a value which is at least the average seeing of the observation and $\gtrsim$2 times the pixel size. It leads to ring width of $\gtrsim$2 arcsec (for data collected at ESO and CFHT), $\gtrsim$3 arcsec (at OHP) and $\sim$5 arcsec (at Mégantic). Previously, the use of rotcur on Hα velocity fields was not very successful because of the poor spatial coverage limited to the brightest H II regions. But as can be seen in Section A2, the spatial coverage of these new data allows rotcur to converge to accurate results, as with H I data. It is mainly due to the new generation of IPCS detector used and to the new adaptive binning technique that allows us to get information of the diffuse Hα component in interarm regions (see Section 3.2).

The sequence of the computation is similar to that usually used for H I velocity fields (e.g. Carignan & Puche 1990; Verheijen & Sancisi 2001) and proceeds as follows:

(i) Average values of $v_{\rm sys}$ and of the dynamical centre coordinates are found from their fitted radial profile. As an initial guess, the photometric parameters are used. The coordinates of the photometric centre were fitted to near-infrared (NIR) images obtained from the 2MASS and GOLDMine data bases. The average seeing of the NIR images is 1.6 arcsec and the accuracy on the photometric coordinates is less than 1 arcsec. The position of the photometric centre is displayed with a cross in the Figs A1–A30 of Section A2. The photometric PAs of the major axis and the inclination were taken in previous optical kinematical studies (Rubin et al. 1999), in the LEDA data base and the Uppsala General Catalogue of Galaxies (Nilson 1973). Notice that in this first iteration the inclination is kept fixed at the photometric value. Keeping the value of PA fixed or free does not influence the determination of $v_{\rm sys}$ and of the coordinates of the rotation centre.

(ii) Then, another least-square fitting is done with these new values of dynamical centre coordinates and $v_{\rm sys}$ as fixed parameters and with i, PA and the rotation velocity as free parameters. An average value of i and PA is computed from their fitted radial profile.

(iii) A last fitting is done by having i and PA fixed by their new constant value, with the rotation velocity as the only free parameter.

A residual velocity field is finally obtained by subtracting a model to the observation. This map is used to determine when an optimal set of parameters is reached, i.e. when the global average and the dispersion (rms) of the residual velocities are minimum.

All points inside a half-sector of 30° (sometimes up to 50° for large inclinations) around the minor axis were rejected and a $|\cos(\theta)|$ weight was applied to the line-of-sight velocities during the fittings (Begeman 1989). Both allow to minimize the contamination of the closest points to the minor axis where important projections effects occur and where the circular velocity term is fitted with difficulty [$\cos(\theta) \rightarrow 0$]. The average parameters are computed with some restrictions. First, one must avoid the inner regions where the velocities are often affected by non-circular motions. This is noticeably the case for barred galaxies (Hernandez et al. 2005a). Their presence is clearly visible in the PV diagrams of Section A2, where the rotation curves rarely fit the emission-line maxima in the central parts. Then, one should not take into account rings which contain too few points. Results for such rings can give unrealistic or highly uncertain results when compared with other well-populated rings. This basically corresponds to rings having a number of points of less than $\sim$15 per cent that of the most populated ring, i.e. for the very inner and outer rings (see Fig. 3, top panel). Finally, one should avoid the regions where only one-half of the disc is observed, or where the number of points in the fitting is highly dominated by that of only one side of a disc.

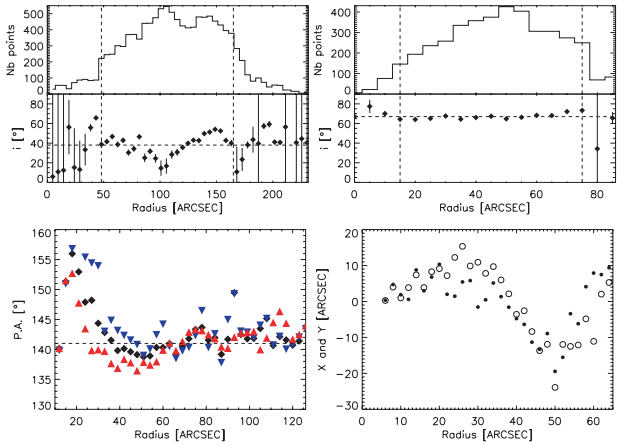

Figure 3. Top: Radial profiles of kinematical inclination for NGC 4535 (left-hand panel) and NGC 4568 (right-hand panel). A dashed horizontal line represents the mean inclination and two dashed vertical lines delineate the radial range within which the mean value is computed. The top panels display the number of points of each annulus. Bottom left-hand panel: Radial profile of kinematical PA for NGC 4501. Blue (red) triangles are for the approaching (receding) half of the disc and filled diamonds for both sides fitted simultaneously. Bottom right-hand panel: Radial profile of the *X*- and *Y*-coordinates (open and filled circles) of the kinematical centre for NGC 4298.

The two 'siamese' galaxies NGC 4567 and 4568 obviously superpose along the line of sight. The fittings should be partly affected by pixels of overlap in their receding halves. The method to decide which of the pixels belong to NGC 4567 or 4568 was to fit models until the residual velocities are minimum in the region of overlap. As a result, it appears that the region of overlap has minimum residual velocities when they are attributed to the NGC 4568 velocity field. This is fully consistent with the photometry where NGC 4568 seems to be projected at the foreground of the pair. The parameters of both galaxies are thus accurately determined.

4.3 Comparison with photometric parameters

Fig. 3 illustrates examples of results from the tilted-ring model fittings to the velocity fields. Table 4 gives the kinematical orientation parameters. The error bar given in Table 4 is the rms (1σ dispersion) of the radial profiles of the inclination or the PA. Fig. 4 shows a comparison between the photometric and kinematical inclinations and PAs of the major axis. A similar comparison is made for the

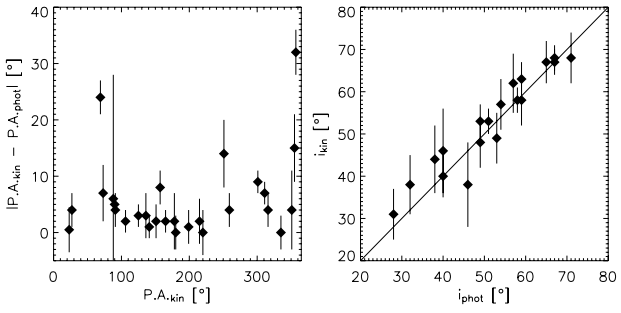

Figure 4. Comparison between photometric and kinematical orientation parameters: absolute value of relative PAs versus the kinematical PA (left-hand panel). Inclination (right-hand panel).

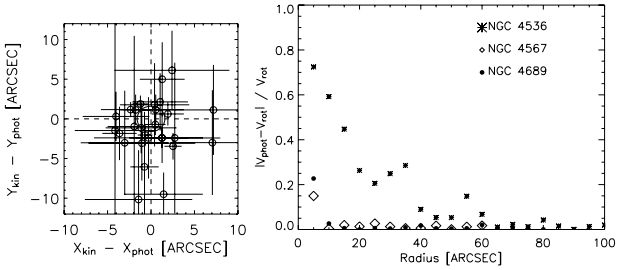

Figure 5. Left-hand panel: Comparison between the kinematical and photometric coordinates. The horizontal and vertical bars are the rms of the kinematical coordinates (respectively) and the circle centred on [0,0] is the mean seeing of the NIR plates, i.e. the error on the position of the photometric centre. Right-hand panel: Comparison between the rotation curves $V_{\rm rot}$ and $V_{\rm phot}$ for NGC 4567, 4536 and 4689. These curves are respectively obtained by fixing the rotation centre at the kinematical and photometric centres.

position of the photometric and kinematical centres in Fig. 5. No fitting has been done for the extremely perturbed galaxy NGC 4438 (as explained in Chemin et al. 2005) and for NGC 4548 (lack of independent points because of too large bins). No PV diagrams are shown for these two galaxies.

4.3.1 Position angle of the major axis

The PA of the major axis is generally the best-determined parameter, with a typical dispersion of 3°. The largest dispersions are for very perturbed galaxies (IC 3583, NGC 4532) or objects having a peculiar kinematics (NGC 4450). A comparison of the kinematical PA with the photometric one is done in Fig. 4 and shows that there is a general good agreement between the two angles. A few galaxies have a misalignment of more than 10° with the photometry (e.g. NGC 4189 and 4519). An analysis of their residual velocity maps confirm that the PA derived from their velocity field is the angle that describes better the gas motions in the disc than when using the photometric PA (see Section 5.1).

For differences lower than 10° (23 galaxies among 28 when removing NGC 4457 which has a strong kinematical twist), the mean absolute difference between the two angles is 3°, which is exactly the typical error bar on the kinematical PA. For those galaxies, the velocity curves derived from long-slit data should give a good representation of the rotational pattern, providing that the position of the photometric centre is also in agreement with the dynamical one.

A few velocity fields exhibit significant kinematical twists (NGC 4457, 4501 and 4579). Kinematical twists are often associated with a warp outside the optical disc and thus with a change of inclination of the H I disc (e.g. Sicotte & Carignan 1997). For NGC 4501 and 4579, the twists occur in the galaxy centres. The NGC 4579 twist is clearly linked to its nuclear spiral (see Section A1) whose orientation differs by ∼90° from that of the large-scale spiral arms. An example is shown in Fig. 3 (bottom) with NGC 4501. Such a twist was also observed in CO data (Wong et al. 2004) and was attributed to an unknown, hidden bar. Its presence remains however to be confirmed by photometry. For those galaxies, a mean value is derived within a radial range where the angle variations are the smallest. It is this mean value which is given in Table 4 and used in the making of their PV diagram. Notice that for NGC 4457, the given PA dispersion remains very large because the PA continuously decreases with radius. For the two remaining galaxies, the PA estimates outside that central region of variation are in good agreement with the photometric values.

4.3.2 Inclination

The kinematical inclination is generally higher than the photometric value but remains in agreement with the photometry within the errors. A large dispersion for the inclination illustrates the difficulty to accurately determine it from high-resolution velocity fields with a tilted-ring model, mainly due to the coupling of the circular velocity and the inclination during the least-square fitting ($V_{\rm rot}\sin(i)$ term of the line-of-sight velocity). The largest dispersions are mainly for inclinations lower than $\sim$50°, as already shown in Begeman (1989) with H I data. Moreover, as for the PA, the inclination of mildly perturbed discs are less accurate than those having a more regular morphology. Fig. 3 shows examples of inclination fittings for the galaxies NGC 4535 ($\sigma = 10°$) and NGC 4568 ($\sigma = 3°$). The kinematical inclinations for IC 3225, IC 3583, NGC 4189, 4351, 4450, 4457, 4532, 4571 and 4689 are very uncertain ($\sigma > 10°$) or very inconsistent with the photometric value (see Table 4). This is not surprising since all these galaxies are either morphologically perturbed discs or have a presumably low photometric inclination. The photometric value was thus used for the extraction of their rotation curve and the modelling of their velocity field.

It is worth noting that $m = 2$ perturbations of the potential of a disc have been shown to also affect the results of inclination and PA fittings in tilted-ring models (Schoenmakers, Franx & de Zeeuw 1997; Schoenmakers 1999; Fridman et al. 2005). The parameter is observed to oscillate around its mean physical value and it results to an increase of the errors on it, as probably observed in many galaxies of this sample. Notice finally that H I velocity maps with lower resolution than the Hα observations logically give lower dispersion of the inclination (e.g. Guhathakurta et al. 1988; Wong et al. 2004), which compare well with our values.

4.3.3 Position of the rotation centre

An example of a radial profile of the kinematical coordinates is displayed in Fig. 3 for the galaxy NGC 4298. The coordinates show a large variation as a function of radius. This implies a large dispersion around the mean coordinates. In view of this quite large variation of the coordinates, getting the most accurate rotation curve with an optical velocity field should perhaps require to leave the centre vary as a function of radius. This is indeed shown to give the most symmetric rotation curves (Beauvais & Bothun 2001). The impact of the oscillations of the coordinates of the dynamical centre on a rotation curve is nevertheless not the purpose of this article. It will be studied in a forthcoming paper. As usually done, it has been decided here to keep the centre fixed and at a constant position. Keeping it constant is precisely what allows to further detect a kinematical lopsidedness in the harmonic analysis that could reflect an environmental effect on a galaxy (see Section 5.2).

Fig. 5 shows the difference between the coordinates of the photometric and kinematical centres (see also in Table 4 and the images of Section A2). The [0,0] location corresponds to that of the photometric centre and a circle to its uncertainty. Its radius is thus given by the seeing of the NIR plates (1.6 arcsec). Though there are very few points inside this circle, the positions of the two centres seem consistent with each other due to the large scatter often observed around the kinematical values (as seen with NGC 4298). The largest departures are for perturbed galaxies (NGC 4457, 4498, 4519 and 4532) but also for large, barred galaxies (NGC 4321 and 4536). For all these objects, it is probably more difficult to determine the position of the photometric centre than for other more regular galaxies. Also, the extinction by dust near a galaxy nucleus could play a role in the determination of the photometric centre, making it harder to find though NIR images are used here for that purpose.

Consequences of centring effects on a rotation curve have been discussed in Beauvais & Bothun (2001). We qualitatively find the same result as them that when choosing the photometric centre instead of the kinematical centre, the velocities of the very innermost annuli of a rotation curve can change drastically. We illustrate this point in Fig. 5 (right-hand panel) with the galaxies NGC 4536, 4567 and 4689. These objects were chosen because the departure between the centres exceeds the NIR plates seeing of 1.6 arcsec. The expression $|V_{\rm phot} - V_{\rm rot}|/V_{\rm rot}$ is displayed, where $V_{\rm phot}$ is the rotation curve derived by fixing the centre at the photometric position (using the kinematical inclination and PA). A systemic velocity corresponding to this centre was fitted and a corresponding residual velocity field was built. The rms of this residual map is generally very few km s^{-1} greater than that of the residual map built using $V_{\rm rot}$ and the kinematical centre. The optical centre is thus not adequately the centre of rotation, though not being necessarily so far from it within the estimated error bars.

The graph of Fig. 5 shows that the difference between the two curves always decreases as a function of radius. The curves only differ by $\sim$2 per cent in the outer regions. The flat part of a rotation curve is therefore not affected by a minor change of centre. In the innermost regions of barred galaxies, differences of up to 70–80 per cent are observed. This difference is not significant because the rotation velocity is highly uncertain, whatever the choice of a centre. This is very likely due to important non-circular motions of the gas kinematics in the central parts of barred galaxies. For non-barred late-type spirals, the velocity of the innermost annuli differ by $\sim$5–25 per cent. This value has to be compared with the formal error bar measured by rotcur at these radii, which is less than 5 per cent of $V_{\rm rot}$. Therefore, contrary to the barred objects, the difference is critical because the velocities at these radii are essential in the determination of the disc mass-to-light ratio in mass models. The choice of the centre is important for this type of galaxies.

5 A SHORT ANALYSIS

This section briefly describes some goals that will be achieved with the high-resolution 3D optical data in future articles from this series.

5.1 Comparison with other Hα works

As we wish to compare our derived rotation curves with results from earlier optical studies (Chincarini & de Souza 1985; Sperandio et al. 1995; Rubin et al. 1999), it is first needed to ensure whether the FP measurements agree with the long-slit data, at least along the *photometric* major axis. An example is illustrated in Fig. 6 with the galaxy NGC 4189. Both long-slit and FP rotation curves extracted along the major axis with a constant PA of 265° agree very well. However, the average kinematical PA (251°) clearly differs from the photometric one. As a consequence, the rotation curve of the galaxy derived with the tilted-ring model differs from the long-slit one (bottom panel of Fig. 6). To check that our result is a better representation of the kinematical pattern than the long-slit one, it is displayed in Fig. 7 the residual velocities obtained by subtracting from the observed two models. A first velocity model is based on the tilted-ring fitting to the FP velocity field (left-hand panel) and another model is based on the smooth long-slit rotation curve with a PA value fixed to the photometric one (right-hand panel). Notice that this smooth model does not take into account the last two points of the long-slit rotation curve and that it does not pass through the

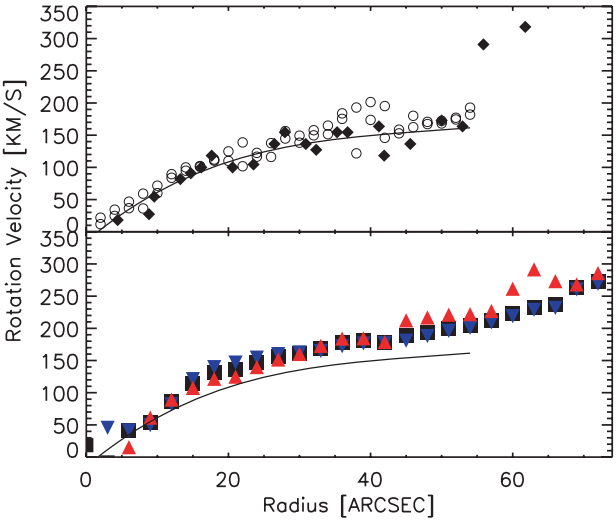

Figure 6. Comparison between the rotation curves of NGC 4189. Top panel: Long-slit rotation curve (Rubin et al. 1999, filled squares), smooth model of long-slit data (solid line) and rotation curve from the FP velocity field extracted along the photometric axis of 265° in a ∼2-arcsec width pseudo-slit (open circles). Bottom panel: Rotation curve of NGC 4189 derived from the tilted-ring model fitting to the velocity field (filled squares and triangles) for a PA value of the major axis of 251°. Blue (red) triangles are for the approaching (receding) half of the disc. The solid line is the smooth model of long-slit data.

zero velocity. This does not change the following result. The figure shows residual velocities more homogeneously distributed in the disc for our model, with a dispersion of 16 km s^{-1} in the residuals, whereas there is an excess of residual velocities on both sides of the major axis for the long-slit model, with a worst dispersion of 28 km s^{-1} in the residuals. This signature is the one expected in a residual map when the model uses an erroneous PA (see Warner, Wright & Baldwin 1973).

As explained in Section 4.3 the photometry and the kinematics are in relatively good agreement, implying that long-slit data should only occasionally give incorrect results, as with NGC 4189 when a strong misalignment is observed. This claim will be tested in a future work for the whole Virgo sample.

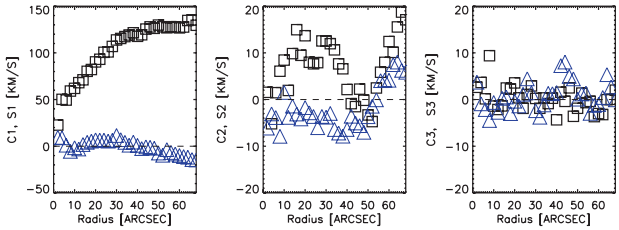

Figure 8. Harmonic decomposition of the velocity field of NGC 4298. Squares (triangles) correspond to the cosine (sine) terms.

5.2 Non-axisymmetry of gaseous velocity fields

Galaxies in clusters are sensitive to the environmental effects. Their structures (gas, stars, dark matter halo) can be perturbed by the cluster tidal field, gravitational encounters with other galaxies, galaxy mergers, accretion of gas, etc. Such external events can trigger internal perturbations in a stellar disc like bars or oval distortions (e.g. Noguchi 1987; Bournaud & Combes 2002), spirals, warps (Huang & Carlberg 1997), polar rings (Bournaud & Combes 2003) or lopsidedness (Bournaud et al. 2005). Ram-pressure stripping is furthermore efficient in creating lopsided gaseous discs and off-plane annular-like gas structures (e.g. Schulz & Struck 2001; Vollmer et al. 2001). All these perturbations are likely responsible for the formation of the kinematical asymmetries observed in our Hα velocity fields (Sections A1 and A2) and in other H I or Hα data (Beauvais & Bothun 1999; Swaters et al. 1999; Beauvais & Bothun 2001; Verheijen & Sancisi 2001), as well as in their optical rotation curves (Rubin et al. 1999; Dale et al. 2001).

Franx, van Gorkom & de Zeeuw (1994), Schoenmakers et al. (1997) or Wong et al. (2004) made an analysis of H I and CO velocity fields by means of Fourier coefficients in order to study the non-axisymmetry of the gas kinematics. A similar approach has been used with stellar kinematics of early-type galaxies by means of kinemetry (Copin et al. 2001; Krajnović et al. 2005). The technique decomposes the line-of-sight velocity along each ring of the tilted-ring model into harmonic terms c_m and s_m of order m following

$$v_{\rm obs} = c_0 + \sum_m c_m \cos(m\Psi) + s_m \sin(m\Psi),$$

where Ψ corresponds to the angle in the plane of the ring, the coefficient c_0 to the systemic velocity of the ring, the first order term c_1

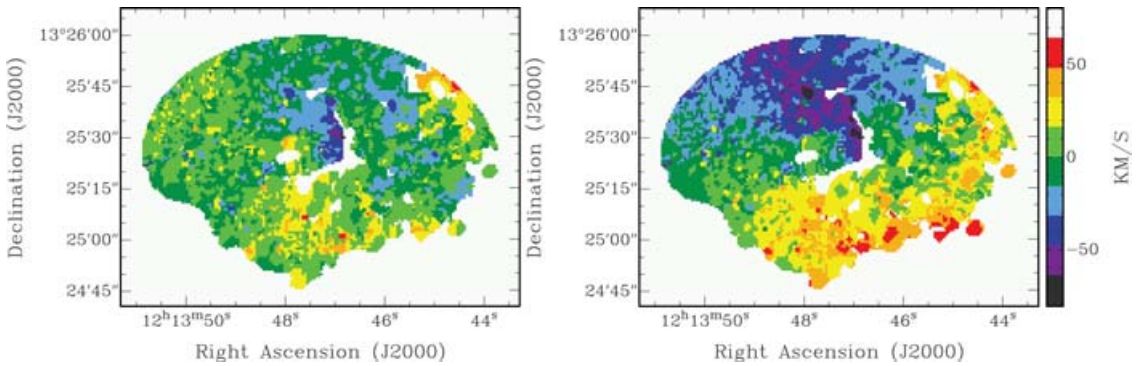

Figure 7. Residual velocity maps of NGC 4189. Left-hand panel: Using the kinematical PA of 251° and the tilted-ring model rotation curve (Fig. 6, bottom). Right-hand panel: Using the photometric PA of 275° and the smooth model of the long-slit data (Fig. 6, top). The velocity range and the colour scale are the same for the two maps.

to more or less the rotation curve and all other terms to non-circular motions (axisymmetric and non-axisymmetric). Schoenmakers et al. (1997) showed that a galaxy perturbed by a distortion of the potential of harmonic order m exhibits terms of order $m - 1$ and $m + 1$ in its velocity field.

This technique has also been applied to ionized gas velocity fields (Krajnović et al. 2005; Simon et al. 2005) and reveals itself here to be successful in detecting the signatures of non-axisymmetry of the 2D Hα kinematics, as seen in Fig. 8. This diagram displays the Fourier coefficients as a function of radius after a harmonic expansion up to an order of $m = 3$ of the velocity field of NGC 4298, using fixed and constant orientation parameters (given in Table 4), kinematical centre position and systemic velocity. The s_1 term is not null and the s_3 term appears to slightly oscillate around zero. There is no bar nor warp in NGC 4298 so that these variations could be due to the presence of a weak $m = 2$ spiral pattern. The most striking feature is the significant variations of the $m = 2$ kinematical terms. This can be caused by $m = 1$ or 3 modes. This latter hypothesis can be rejected because the Hα morphology of NGC 4298 does not show signatures of $m = 3$ structures like, for example, 3 spiral arms. There is no direct evidence of a 'one spiral arm' structure in NGC 4298 so that the $m = 1$ mode could be caused by a kinematical lopsidedness. The presence of the galaxy NGC 4302, companion of NGC 4298 in the sky plane but also in radial velocity, could be at the origin of the observed asymmetries. Beauvais & Bothun (1999) also observed drifting centres in their FP observations. While a large number of galaxies appear to exhibit a *morphological* lopsidedness, as revealed by galaxy imagery (Bournaud et al. 2005) or H I data (Swaters et al. 1999; Noordermeer et al. 2005), evidence of *kinematical* lopsidedness such as the one probably detected here in NGC 4298 seem to be rare in the WHISP sample of Noordermeer et al. (2005).

A forthcoming work will apply the Fourier analysis to the Virgo cluster sample (as well as velocity maps of field galaxies) and will investigate how the kinematical perturbations can be related to the cluster environment.

6 CONCLUSION

This article has presented FP interferometry observations of the ionized gas for a sample of 30 spiral and irregular galaxies of the Virgo cluster. This is the first time that a sample of Hα integrated emission-line maps and velocity fields are collected in order to study the environmental effects on the 2D, high-resolution kinematics of cluster galaxies. Two new improvements in the reduction of the FP data consist in a better sky subtraction and an adaptive binning. Both these procedures allow to achieve an optimal S/N in the FOV and a better detection of the diffuse ionized gas in interarm or external regions.

The galaxies exhibit morphological irregularities like nuclear spiral, nuclear and inner pseudo-ring, off-plane diffuse filaments and arc-like structure, truncated disc, lopsidedness, bar and spiral arms. The velocity fields exhibit typical kinematical perturbations like streaming motions along spiral arms, twist of the major axis, Z shape of velocities due to the presence of a bar, decoupled nuclear spiral or misalignment between photometric and kinematical major axes. Future papers from this series will present the rotation curves and mass models of the galaxies and investigate whether the asymmetries observed in the velocity fields have a relation with such a dense environment.

ACKNOWLEDGMENTS

This paper is based on observations collected at the ESO (program 69.B-0496), the Observatoire du mont Mégantic (Québec, Canada), the Observatoire de Haute-Provence (France) and the CFHT, which is operated by the National Research Council of Canada, the Centre National de la Recherche Scientifique de France and the University of Hawaii. We are grateful to the anonymous referee for valuable comments. We thank all the staffs of the observatories which helped us during different runs. We are very grateful to B. Malenfant and G. Turcotte at the Observatoire du mont Mégantic, to O. Daigle, J.-L. Gach, M.-M. de Denus-Baillargeon, M.-H. Nicol and D. Naudet for their help during the observations or the preparation of the article. LC thanks F. Combes and F. Bournaud for insightful conversations. CB thanks the PPF program at the Observatoire de Paris for financial support. This work was partly funded by the grant Regroupement Stratégique – Observatoire du mont Mégantic of FQRNT (Québec) and by the Ministère de l'Éducation Nationale, de la Recherche et de la Technologie (France). The FaNTOmM project has been carried out by the Laboratoire d'Astrophysique Expérimentale of the Université de Montréal using grant from the Canadian Foundation for Innovation and the Ministére de l'Éducation du Québec. We made use of the HyperLeda data base (http://leda.univ-lyon1.fr) and NASA/IPAC Extragalactic Database (http://nedwww.ipac.caltech.edu) . This research has made use of the GOLDMine data base and products: Galaxy Online Database Milano Network (http://goldmine.mib.infn.it). This publication makes use of data products from the 2MASS, which is a joint project of the University of Massachusetts and the Infrared Processing and Analysis Center/California Institute of Technology, funded by the National Aeronautics and Space Administration and the National Science Foundation.

REFERENCES

Abadi M. G., Moore B., Bower R. G., 1999, MNRAS, 308, 947
Adami C., Biviano A., Mazure A., 1998, A&A, 331, 439
Adami C., Marcelin M., Amram P., Russeil D., 1999, A&A, 349, 812
Adami C., Holden B. P., Castander F. J., Mazure A., Nichol R. C., Ulmer M. P., 2000, A&A, 362, 825
Amram P., 1991, PhD thesis, Université de Provence, France
Amram P., Sullivan W. T., Balkowski C., Marcelin M., Cayatte V., 1993, ApJ, 403, L59
Amram P., Balkowski C., Boulesteix J., Cayatte V., Marcelin M., Sullivan W. T., 1996, A&A, 310, 737
Amran P. et al., 2004, ApJ, 612, L5
Arsenault R., Roy J.-R., Boulesteix J., 1990, A&A, 234, 23
Bacon R. et al., 2001, MNRAS, 326, 23
Balogh M. L., Morris S. L., Yee H. K. C., Carlberg R. G., Ellingson E., 1999, ApJ, 527, 54
Bamford S. P., Milvang-Jensen B., Aragón-Salamanca A., Simard L., 2005, MNRAS, 361, 109
Barth A. J., Ho L. C., Filippenko A. V., Rix H.-W., Sargent W. L. W., 2001, ApJ, 546, 205
Beauvais C., Bothun G., 1999, ApJS, 125, 99
Beauvais C., Bothun G., 2001, ApJS, 136, 41
Begeman K. G., 1987, PhD thesis, Groningen Univ.
Begeman K. G., 1989, A&A, 223, 47
Bershady M. A., Andersen D. R., Harker J., Ramsey L. W., Verheijen M. A. W., 2004, PASP, 116, 565
Bershady M. A., Andersen D. R., Verheijen M. A. W., Westfall K. B., Crawford S. M., Swaters R. A., 2005, ApJS, 156, 311
Binggeli B., Sandage A., Tammann G., 1985, AJ, 90, 1681
Binggeli B., Tammann G., Sandage A., 1987, AJ, 94, 251
Binggeli B., Popescu C., Tammann G., 1993, A&AS, 98, 275

Böhringer H., Brie1 U. G., Schwarz R. A., Voges W., Hartner G., Trumper J., 1994, Nat, 368, 828
Boselli A., Gavazzi G., 2002, A&A, 386, 124
Boselli A., Iglesias-Páramo J., Vílchez J. M., Gavazzi G., 2002, A&A, 386, 134
Bosma A., 1981, AJ, 86, 1825
Boulesteix J., 1993, The ADHOCW Cookbook, Internal Publication of the Observatoire de Marseille (http://www-obs.cnrs-mrs.fr/adhoc/adhocw.htm)
Bournaud F., Combes F., 2002, A&A, 392, 83
Bournaud F., Combes F., 2003, A&A, 401, 817
Bournaud F., Combes F., Jog C. J., Puerari I., 2005, A&A, 438, 507
Bravo-Alfaro H., Cayatte V., van Gorkom J. H., Balkowski C., 2000, AJ, 119, 580
Buta R., Vasylyev S., Salo H., Laurikainen E., 2005, AJ, 130, 506
Butcher H., Oemler A., Jr, 1978, ApJ, 219, 18
Butcher H., Oemler A., Jr, 1984, ApJ, 285, 426
Canzian B., Allen R. J., 1997, ApJ, 479, 723
Cappellari M., Copin Y., 2003, MNRAS, 342, 345
Carignan C., Beaulieu S., 1989, ApJ, 347, 760
Carignan C., Puche D., 1990, AJ, 100, 394
Cayatte V., van Gorkom J. H., Balkowski C., Kotanyi C., 1990, AJ, 100, 604
Cayatte V., Kotanyi C., Balkowski C., van Gorkom J. H., 1994, AJ, 107, 1003
Chamaraux P., Balkowski C., Gérard E., 1980, A&A, 83, 38
Chemin L., 2003, PhD thesis, Université Paris VI, Paris
Chemin L. et al., 2005, A&A, 436, 469
Chincarini G., de Souza R., 1985, A&A, 153, 218
Copin Y. et al., 2001, in Combes F., Barret D., Thévenin F., eds, SF2A-2001, EdP-Sciences
Couch W. J., Sharples R. M., 1987, MNRAS, 229, 423
Daigle O., Carignan C., Amram P., Hernandez O., Chemin L., Balkowski C., Kennicutt R., MNRAS, submitted
Daigle O., Carignan C., Hernandez O., Chemin L., Amram P., MNRAS, submitted
Dale D. A., Giovanelli R., Haynes M. P., Scodeggio M., Hardy E., Campusano L. E., 1997, AJ, 114, 455
Dale D. A., Giovanelli R., Haynes M. P., Hardy E., Campusano L. E., 1999, AJ, 118, 1468
Dale D. A., Giovanelli R., Haynes M. P., Hardy E., Campusano L. E., 2001, AJ, 121, 1886
de Blok W. J. G., McGaugh S. S., van der Hulst J. M., 1996, MNRAS, 283, 18
de Vaucouleurs G., de Vaucouleurs A., Corwin H. G., Buta R. J., Paturel G., Fouque P., 1991, Third Reference Catalogue of Bright Galaxies. Springer-Verlag, Berlin
de Zeeuw P. T. et al., 2002, MNRAS, 329, 513
Distefano A., Rampazzo R., Chincarini G., de Souza R., 1990, A&AS, 86, 7
Dressler A., 1980, ApJ, 236, 351
Dressler A. et al., 1997, ApJ, 490, 577
Dressler A., Smail I., Poggianti B. M., Butcher H., Couch W. J., Ellis R. S., Oemler A. J., 1999, ApJS, 122, 51
Dubinski J., 1998, ApJ, 502, 141
Ellis R. S., Smail I., Dressler A., Couch W. J., Oemler A. J., Butcher H., Sharples R. M., 1997, ApJ, 483, 582
Elmegreen D. M., Chromey F. R., Bissell B. A., Corrado K., 1999, AJ, 118, 2618
Emsellem E. et al., 2004, MNRAS, 352, 721
Evans I. N., Koratkar A. P., Storchi-Bergmann T., Kirkpatrick H., Heckman T. M., Wilson A. S., 1996, ApJS, 105, 93
Fasano G., Poggianti B. M., Couch W. J., Bettoni D., Kjærgaard P., Moles M., 2000, ApJ, 542, 673
Fouqué P., Solanes J. M., Sanchis T., Balkowski C., 2001, A&A, 375, 770
Franx M., van Gorkom J. H., de Zeeuw T., 1994, ApJ, 436, 642
Fridman A. M., Afanasiev V. L., Dodonov S. N., Khoruzhii O. V., Moiseev A. V., Sil'chenko O. K., Zasov A. V., 2005, A&A, 430, 67
Gach J.-L. et al., 2002, PASP, 114, 1043
Garrido O., Marcelin M., Amram P., Boulesteix J., 2002, A&A, 387, 821
Gavazzi G., 1987, ApJ, 320, 96
Gavazzi G., Boselli A., Scodeggio M., Pierini D., Belsole E., 1999, MNRAS, 304, 595
Gavazzi G., Boselli A., Pedotti P., Gallazzi A., Carrasco L., 2002, A&A, 386, 114
Gavazzi G., Boselli A., Donati A., Franzetti P., Scodeggio M., 2003, A&A, 400, 451
Gavazzi G., Boselli A., van Driel W., O'Neil K., 2005, A&A, 429, 439
Giovanelli R., Haynes M. P., 1985, ApJ, 292, 404
Giovanelli R., Haynes M. P., 2002, ApJ, 571, L107
Gnedin O. Y., 2003a, ApJ, 582, 141
Gnedin O. Y., 2003b, ApJ, 589, 752
Goad J. W., Roberts M. S., 1981, ApJ, 250, 79
González Delgado R. M., Pérez E., 1996, MNRAS, 281, 1105
González Delgado R. M., Pérez E., Tadhunter C., Vilchez J. M., Rodriguez-Espinosa J. M., 1997, ApJS, 108, 155
Gooch R., 1996, in Kron R. G., ed., ASP Conf. Ser. Vol. 101, Evolution of the Universe of Galaxies: Edwin Hubble Centennial Symposium. Astron. Soc. Pac., San Francisco, p. 80
Guhathakurta P., van Gorkom J. H., Kotanyi C. G., Balkowski C., 1988, AJ, 96, 851
Gunn J. E., Gott J. R., III, 1972, ApJ, 176, 1
Helfer T. T., Thornley M. D., Regan M. W., Wong T., Sheth K., Vogel S. N., Blitz L., Bock D. C.-J., 2003, ApJS, 145, 259
Hernandez O., Gach J.-L., Carignan C., Boulesteix J., 2003, SPIE, 4841, 1472
Hernandez O., Carignan C., Amram P., Chemin L., Daigle O., 2005a, MNRAS, 360, 1201
Hernandez O., Wozniak H., Carignan C., Amram P., Chemin L., Daigle O., 2005b, ApJ, 632, 253
Hoffman G. L., Lu N. Y., Salpeter E. E., Connell B. M., 1999, AJ, 117, 811
Huang S., Carlberg R. G., 1997, ApJ, 480, 503
Jarrett T. H., Chester T., Cutri R., Schneider S., Skrutskie M., Huchra J. P., 2000, AJ, 119, 2498
Keel W. C., 1983, ApJ, 268, 632
Kenney J. D. P., Yale E. E., 2002, ApJ, 567, 865
Kenney J. D. P., Rubin V. C., Planesas P., Young J. S., 1995, ApJ, 438, 135
Knapen J. H., Beckman J. E., Heller C. H., Shlosman I., de Jong R. S., 1995, ApJ, 454, 623
Knapen J. H., Shlosman I., Heller C. H., Rand R. J., Beckman J. E., Rozas M., 2000, ApJ, 528, 219
Koopmann R. A., Kenney J. D. P., 2004, ApJ, 613, 866
Koopmann R. A., Kenney J. D. P., Young, J., 2001, ApJS, 135, 125
Krajnović D., Cappellari M., Emsellem E., McDermid R. M., de Zeeuw P. T., 2005, MNRAS, 357, 1113
Kranz T., Slyz A., Rix H.-W., 2001, ApJ, 562, 164
Laval A., Boulesteix J., Georgelin Y. P., Georgelin Y. M., Marcelin M., 1987, A&A, 175, 199
Macri L. M. et al., 1999, ApJ, 521, 155
Merritt D., 1985, ApJ, 289, 18
Moore B., Katz N., Lake G., Dressler A., Oemler A., 1996, Nat, 379, 613
Moore B., Lake G., Katz N., 1998, ApJ, 499, L5
Moore B., Lake G., Quinn T., Stadel J., 1999, MNRAS, 304, 465
Moss C., Whittle M., 2000, MNRAS, 317, 667
Nilson P., 1973, UGC of Galaxies, Acta Universitatis Upsaliensis, Nova Acta Regiae Societatis Scientiarum Upsaliensis – Uppsala Astronomiska Observatoriums Annaler
Noguchi M., 1987, MNRAS, 228, 635
Noordermeer E., van der Hulst J. M., Sancisi R., Swaters R. A., van Albada T. S., 2005, A&A, 442, 137
Onodera S., Koda J., Sofue Y., Kohno K., 2004, PASJ, 56, 439
Paturel G., Garcia A. M., Fouque P., Buta R., 1991, A&A, 243, 319
Phookun B., Vogel S. N., Mundy L. G., 1993, ApJ, 418, 113
Pogge R. W., 1989, ApJS, 71, 433
Poggianti B., 2004, in Dettmar R. J., Klein U., Salucci P., eds, Baryons in Dark Matter Halos. SISSA, Proceedings of Science, p. 104
Poggianti B. M., Smail I., Dressler A., Couch W. J., Barger A. J., Butcher H., Ellis R. S., Oemler A. J., 1999, ApJ, 518, 576

Postman M., et al. 2005, ApJ, 623, 721
Quilis V., Moore B., Bower R. G., 2000, Sci, 288, 1617
Rampazzo R., Plana H., Amram P., Bagarotto S., Boulesteix J., Rosado M., 2005, MNRAS, 356, 1177
Roediger E., Hensler G., 2005, A&A, 433, 875
Rogstad D. H., Lockart I. A., Wright M. C. H., 1974, ApJ, 193, 309
Rubin V. C., Waterman A. H., Kenney J. D. P., 1999, AJ, 118, 236
Saha A., Sandage A., Labhardt L., Tammann G. A., Macchetto F. D., Panagia N., 1997, ApJ, 486, 1
Sanchis T., Mamon G.A., Salvador-Solé E., Solanes J. M., 2004, A&A, 418, 393
Schoenmakers R. H. M., 1999, PhD thesis, Groningen Univ.
Schommer R. A., Bothun G. D., Williams T. B., Mould J. R., 1993, AJ, 105, 97
Schoenmakers R. H. M., Franx M., de Zeeuw P. T., 1997, MNRAS, 292, 349
Schulz S., Struck C., 2001, MNRAS, 328, 185
Shibata R., Matsushita K., Yamasaki N. Y., Ohashi T., Ishida M., Kikuchi K., Böhringer H., Matsumoto H., 2001, ApJ, 549, 228
Sicotte V., Carignan C., 1997, AJ, 113, 609
Simon J. D., Bolatto A. D., Leroy A., Blitz L., Gates E. L., 2005, ApJ, 621, 757
Smith G. P., Treu T., Ellis R. S., Moran S. M., Dressler A., 2005, ApJ, 620, 78
Sofue Y., Koda J., Nakanishi H., Onodera S., Kohno K., Tomita A., Okumura S. K., 2003a, PASJ, 55, 17
Sofue Y., Koda J., Nakanishi H., Onodera S., 2003b, PASJ, 55, 59
Solanes J. M., Manrique A., García-Gómez C., González-Casado G., Giovanelli R., Haynes M. P., 2001, ApJ, 548, 97
Solanes J. M., Sanchis T., Salvador-Solé E., Giovanelli R., Haynes M. P., 2002, AJ, 124, 2440
Sperandio M., Chincarini G., Rampazzo R., de Souza R., 1995, A&AS, 110, 279
Swaters R. A., Schoenmakers R. H. M., Sancisi R., van Albada T. S., 1999, MNRAS, 304, 330
Tran K.-V. H., Franx M., Illingworth G., Kelson D. D., van Dokkum P., 2003, ApJ, 599, 865
Tschöke D., Bomans D. J., Hensler G., Junkes N., 2001, A&A, 380, 40
van der Hulst J. M., Skillman E. D., Kennicutt R. C., Bothun G. D., 1987, A&A, 177, 63
van der Hulst J. M., Terlouw J. P., Begeman K. G., Zwitser W., Roelfsema P. R., 1992, in Worrall D. M., Biemesderfer C., Barnes J., eds, ASP Conf. Ser. Vol. 25, Astronomical Data Analysis Software and Systems I. Astron. Soc. Pac., San Francisco, p. 131
van der Hulst J. M., Skillman E. D., Smith T. R., Bothun G. D., McGaugh S. S., de Blok W. J. G., 1993, AJ, 106, 548
van Dokkum P. G., Franx M., 2001, ApJ, 553, 90
van Dokkum P. G., Franx M., Kelson D. D., Illingworth G. D., 1998, ApJ, 504, L17
Verheijen M. A. W., 2001, ApJ, 563, 694
Verheijen M. A. W., Sancisi R., 2001, A&A, 370, 765
Vogt N. P., Haynes M. P., Giovanelli R., Herter T., 2004, AJ, 127, 3300
Vollmer B., 2003, A&A, 398, 525
Vollmer B., Marcelin M., Amram P., Balkowski C., Cayatte V., Garrido O., 2000, A&A, 364, 532
Vollmer B., Cayatte V., Balkowski C., Duschl W. J., 2001, ApJ, 561, 708
Vollmer B., Balkowski C., Cayatte V., van Driel W., Huchtmeier W., 2004, A&A, 419, 35
Warmels R. H., 1988a, A&AS, 72, 19
Warmels R. H., 1988b, A&AS, 72, 57
Warmels R. H., 1988c, A&AS, 72, 427
Warner P. J., Wright M. C. H., Baldwin J. E., 1973, MNRAS, 163, 163
Wong T., Blitz L., Bosma A., 2004, ApJ, 605, 183
Yasuda N., Fukugita M., Okamura S., 1997, ApJS, 108, 417
Yoshida M. et al., 2004, AJ, 127, 90
Ziegler B. L., Böhm A., Jäger K., Heidt J., Möllenhoff C., 2003, ApJ, 598, L87

APPENDIX A: THE KINEMATICAL Hα CATALOGUE OF VIRGO GALAXIES

A1 Comments for individual galaxies

NGC 4189 The velocity field of this barred multi-armed galaxy is slightly perturbed. The PV diagram reveals that the Hα peak in the nucleus has an almost constant velocity, whose signature was already observed in the long-slit data (Rubin et al. 1999). The kinematical and photometric major axes are not aligned.

NGC 4212 The galaxy presents a mildly perturbed velocity field in the northern and western regions. The optical and NIR images clearly reveal an important dust obscuration effect in the galaxy. This may disturb the gaseous kinematics of NGC 4212, as particularly seen in the western region. The long-slit data showed velocities down to $\sim -240\,\mathrm{km\,s^{-1}}$ (Rubin et al. 1999), which are not observed here. As in the CO data (Sofue et al. 2003a), the core exhibits a steeper velocity gradient than the rest of the disc. This could be due to the presence of a hidden bar. A careful analysis of the NIR image by an isophotal ellispses fitting indeed seems to reveal the presence of an elongated inner structure (see also Buta et al. 2005).

NGC 4237 The velocity field shows no real signs of perturbations, except for a clump in the receding half to the South (RA $\sim 12^{\mathrm{h}}17^{\mathrm{m}}12\overset{\mathrm{s}}{.}53$, Dec. $\sim +15^{\circ}18'58''$), which exhibits a lower velocity ($\sim$900 km s^{-1}) than its surroundings ($\sim$950 km s^{-1}). Streamings of gas are also observed.

NGC 4254 The prominent spiral structure is asymmetric in this well-known galaxy, as well as its Hα velocity field. Streaming motions are observed along the spiral arms. Our observation of NGC 4254 is in good agreement with the Hα and H I velocity fields presented in Phookun et al. (1993). Notice a region at RA $\sim 12^{\mathrm{h}}18^{\mathrm{m}}57\overset{\mathrm{s}}{.}56$, Dec. $\sim +14^{\circ}26'55''$, $v_{\mathrm{obs}} \sim 2535\,\mathrm{km\,s^{-1}}$) having a higher velocity than its surroundings ($\sim$2500 km s^{-1}). CO data show a steep velocity rise in the innermost arcseconds (80 km s^{-1}). It could be due to a small bar detected by Kranz, Slyz & Rix (2001).

NGC 4294 With NGC 4299, NGC 4294 belongs to an apparent pair. Streaming motions are seen along the spiral arms. The receding half appears slightly perturbed, with H II regions having lower radial velocities than the local diffuse gas (e.g. at RA $\sim 12^{\mathrm{h}}21^{\mathrm{m}}16\overset{\mathrm{s}}{.}92$, Dec. $\sim +11^{\circ}31'01''$).

NGC 4298 This apparently flocculent galaxy (Elmegreen et al. 1999) has a companion NGC 4302 only at a distance 2.3 arcmin (or 10.7 kpc projected) and with nearly the same systemic velocity ($v_{\mathrm{sys}}^{N4302} = 1149\,\mathrm{km\,s^{-1}}$, Binggeli et al. 1985). According to Koopmann & Kenney (2004), the truncated gas disc is due to RPS and the stellar asymmetry to a tidal interaction with a companion. The velocity field appears however mildly perturbed. Notice that the southern arm presents velocities more redshifted than the nearby parts of the disc at the same azimuthal angles. This perhaps indicates streaming motions along it or, less probably, a locally warped arm. A steep velocity rise is detected in the PV diagram in the core of the galaxy.

IC 3225 This magellanic-type galaxy has an enhanced star formation on the NE, approaching half of its disc whereas very little ionized gas is detected on the SW half. The *B*-band distribution shows an elongated stellar disc to the SW whereas the NIR image has a truncated disc in this direction. As seen in the PV diagram, the velocity smoothly increases with radius. The velocity field thus mainly displays a solid-body rotating pattern. This is typical of highly inclined optically thick discs, which projection effects prevents from observing the true rotation (Goad & Roberts 1981; Giovanelli & Haynes 2002).

NGC 4321 The well-known galaxy NGC 4321 (M100) has often been mapped with FP interferometry (Arsenault et al. 1990; Knapen et al. 1995; Canzian & Allen 1997; Hernandez et al. 2005b). Evidence for three different pattern speeds (nuclear structure, large-scale bar, spiral) has been shown using the Tremaine–Weinberg method on this rather regular velocity field (Hernandez et al. 2005b), which also shows signs of streaming motions (Knapen et al. 2000). The core of the galaxy has a nuclear ring-like structure.

NGC 4351 The galaxy is slowly rotating. It has a peculiar gaseous morphology, showing an arm-like structure to the North. The stellar distribution appears lopsided, also with an arm-like structure in the northern and western regions of the galaxy. The stellar asymmetry could result from a past tidal interaction, or even a merger. This galaxy is also a very good candidate for an ongoing RPS (Koopmann & Kenney 2004).

NGC 4405 The Hα distribution is truncated and the velocity map displays a solid-body rotating pattern. This is understandable in a framework where only the central regions lying in the rising part of a rotation curve are observed.

NGC 4438 Notice the off-plane filamentary morphology of the ionized gas to the West and South of the galaxy disc, which was already seen in Kenney et al. (1995) and Kenney & Yale (2002). No H I was detected in the disc (Cayatte et al. 1990). The ionized gas is the best tracer of the complex morphology and kinematics of the galaxy, which is presented in detail in Chemin et al. (2005).

NGC 4450 Like in the H I data of Cayatte et al. (1990), this anaemic galaxy has a patchy Hα distribution. The Hα spiral appears highly wound around the centre. The velocity field appears significantly dispersed in the galaxy inner parts as well as in the outer ones but to a lesser extent. The nucleus displays a steep gradient ($\sim$200 km s^{-1}), which result was already seen in long-slit data (Rubin et al. 1999). Little CO gas is observed in NGC 4450 (Helfer et al. 2003).

NGC 4457 The distribution and the kinematics of this galaxy are very peculiar. There is little ionized gas in the receding side, which is traced by only few star formation regions while the approaching side consists in a single Hα armlet. The core region surprisingly exhibits the most blue-shifted velocities observed in the galaxy.

NGC 4498 The emission is mostly located in H II regions along the stellar bar-like structure. The kinematics of NGC 4498 is asymmetric: the approaching half is typical of a constant velocity rotational pattern while the receding side has solid-body rotation.

NGC 4501 The Hα velocity map of NGC 4501 (M88) appears regular with the exception of non-circular motions associated to the spiral structure, as particularly seen along the minor axis. NGC 4501 exhibits one of the largest velocity range among all the galaxies presented here, indicating a very massive object. Notice that part of the NW Hα spiral arm is missing in the approaching half of the disc, which is probably due to a dust obscuration effect and to a low transmission of the interference filter. The CO kinematics in the $\pm$4 arcsec region around the photometric centre is complex, as revealed by double peaks in the molecular gas emission (Onodera et al. 2004). The Hα PV diagram also shows a complex central kinematics. Cayatte et al. (1990) showed compressed contours of H I distribution to the SE.

NGC 4519 The galaxy morphology is perturbed, as well as the velocity field where streaming motions are revealed along the multiple spiral arms. Notice the strong Z shape of the velocities due to the presence of the bar. This galaxy has a misalignment between photometric and kinematical major axes.

NGC 4532 The velocity map is very perturbed. It displays a strong Z-shape kinematical pattern, which has already been observed in the H I velocity field (Hoffman et al. 1999). A systemic velocity component ($\sim$2010 km s^{-1}) is observed along the north-western edge of the Hα distribution. NGC 4532 has the highest Hα equivalent width in the sample of Koopmann & Kenney (2004). It is not surprising while regarding its perturbed stellar and gaseous morphologies, with prominent star forming regions (like, e.g. the off-plane one at RA $\sim$ $12^{\rm h}34^{\rm m}21\overset{\rm s}{.}02$, Dec. $\sim$ $+06^{\circ}27'38''$) and stellar extensions. All the perturbations may result from a tidal interaction and/or gas accretion (Hoffman et al. 1999). Notice that an optical reflection of the galaxy was masked, giving artificial sharp edges to the shape of the galaxy in its eastern parts.

NGC 4535 This barred galaxy has a low inclination and an irregular morphology, as mostly seen in the *B*-band and Hα images, with several spiral-like structures arising to the North and South in addition to the main spiral pattern. The velocity field is perturbed in the northern Hα loop and in the southern arm-like extension. Streaming motions are also observed along the arms. The PV diagram shows a steep velocity rise associated with the bright Hα core. The central regions of NGC 4535 have no neutral gas (Cayatte et al. 1990).

NGC 4536 This large barred galaxy displays two main prominent spiral arms and additional spiral-like structures. The only kinematical perturbations are seen in the Z shape of the velocities in the central parts and streaming motions along the arms. As in the CO data (Sofue et al. 2003a), a steep velocity gradient is observed in the Hα data in the galaxy core.

NGC 4548 The observation has a very low initial S/N which causes the bin sizes to be large during the Voronoi tessellation. The disc rotation is nevertheless seen, with a velocity gradient of $\sim$200 km s^{-1}, which is in agreement with that deduced from long-slit spectroscopy (Rubin et al. 1999).

NGC 4567 This galaxy is part of a pair with NGC 4568. The morphology and the velocity field do not show signs of disturbance.

NGC 4568 Here again, no clear signs of velocity disturbance are observed, except perhaps in the external regions of the disc. Koopmann & Kenney (2004) claim that this galaxy pair likely experiences RPS and a tidal interaction. It is however not obvious that a tidal interaction is (or has) occurring (occurred) while regarding the very mildly perturbed kinematics of the pair.

IC 3583 The galaxy presents irregular stellar and gaseous morphologies. Tschöke et al. (2001) revealed the presence of a faint, narrow spur of star formation regions to the South, pointing towards NGC 4569. This spur is also seen in the FP field. A weak rotation is evidenced in the perturbed velocity map ($\sim$100 km s^{-1} in projection).

NGC 4569 The velocity field of the galaxy is perturbed, showing gas streamings along the arm-like structures in the Hα (severely) truncated disc. An off-plane string of H II regions is observed to the West of the disc. It exhibits a velocity gradient that follows the rotation of the disc. This gaseous structure has already been seen in deep Hα image (Tschöke et al. 2001) and in H I data (Vollmer et al. 2004). The giant diffuse gaseous region to the West of the disc (Tschöke et al. 2001) is not detected in the FP observation, which is probably due to a too low S/N or to a likely cut-off in the transmission of the interference filter. Vollmer et al. (2004) proposed an RPS model to explain the H I asymmetry.

NGC 4571 This almost face-on galaxy has a very patchy distribution of H II regions. The interference filter unfortunately cuts part of the emission in the NE region. The 21-cm data show an H I distribution well confined in the optical disc boundaries (van der Hulst et al. 1987). The Hα kinematics is in agreement with the H I data and presents a slightly perturbed velocity field.

NGC 4579 The FP data presents an Hα kinematics of NGC 4579 (M58) which is perturbed by the streaming motions along the large-scale spiral arms and by a rather large velocity dispersion in the receding half (by comparison with the approaching side). The circumnuclear region is particularly interesting because it exhibits a bright 'loop' structure within a radius of ∼1.5 kpc (Keel 1983; Pogge 1989; González Delgado & Pérez 1996) and the nucleus is known to have an extremely broad Hα profile with a full width at zero intensity of up to 18 000 km s^{-1} (Barth et al. 2001). The so-called 'loop' is actually an asymmetric nuclear spiral which displays a very large velocity gradient (∼500 km s^{-1}). The kinematical major axis of the nuclear spiral is almost perpendicular to that of the large-scale spiral structure. The high-resolution data of the molecular gas component showed CO emission concentrated within the core (Helfer et al. 2003; Sofue et al. 2003a) and the neutral hydrogen emission was lying in an annulus-like structure (Cayatte et al. 1990) which is actually the large-scale spiral arms.

NGC 4580 This Hα truncated disc displays little kinematical irregularities and a small velocity gradient. Though the Hα covers the innermost parts of the stellar distribution like in NGC 4405, a constant velocity seems to be reached along the major axis, which was not seen in NGC 4405. The Hα morphology is in the form of a pseudo-ring. No ionized gas is detected in the spiral arms that can be seen in the broad-band images.

NGC 4639 This barred galaxy exhibits a remarkable inner ring (Evans et al. 1996; González et al. 1997). The outer gaseous distribution is furthermore reminiscent of an outer pseudo-ring. This outer structure is visible in the *B*-band image but hardly in the NIR image, which principally shows the bar and the bulge. The velocity field is rather regular, consistent with a flat circular velocity pattern of the disc. It also shows streaming motions in the ring. A steep velocity rise is seen in the galaxy core, as was also observed in Rubin et al. (1999).

NGC 4654 The stellar and gaseous morphologies are very asymmetric. The Hα velocity field is strongly perturbed. Alternating patterns of (decreasing and increasing) solid body and constant velocity are observed through the field, which is well illustrated by the PV diagram. In the approaching half, the transition region between the central solid-body part and the outer decrease occurring at an offset of −1 arcmin leaves a remarkable imprint in the velocity field. In addition, streaming motions are evidenced along the spiral arms. A solid-body rotation is partly associated with the very thin and elongated Hα bar-like structure in the central parts. According to Vollmer (2003), a scenario mixing effects of a tidal interaction with NGC 4639 ∼500 Myr ago and RPS could be responsible for the perturbed stellar and gaseous distributions of NGC 4654. There is a large difference of distance between the two galaxies, ∼22 and ∼25 Mpc for NGC 4639 as estimated from the Tully–Fisher relation (Yasuda et al. 1997) and the Cepheids method (Saha et al. 1997), respectively, and ∼14 Mpc for NGC 4654 (Tully–Fisher relation, Yasuda et al. 1997). This inconsistency of distance points out that the Tully–Fisher distance of NGC 4654 must be highly erroneous if the Vollmer's scenario is valid.

NGC 4689 As for NGC 4571, the Hα emission is very patchy. The velocity field appears slightly perturbed, showing evident signs of streamings associated with the pseudo-spiral arms. The Hα kinematics is in good agreement with the H I (Cayatte et al. 1990) and CO (Sofue et al. 2003a) data.

A2 Observational data

Presentation of the Hα maps of the 30 Virgo galaxies (Figs A1–A30).

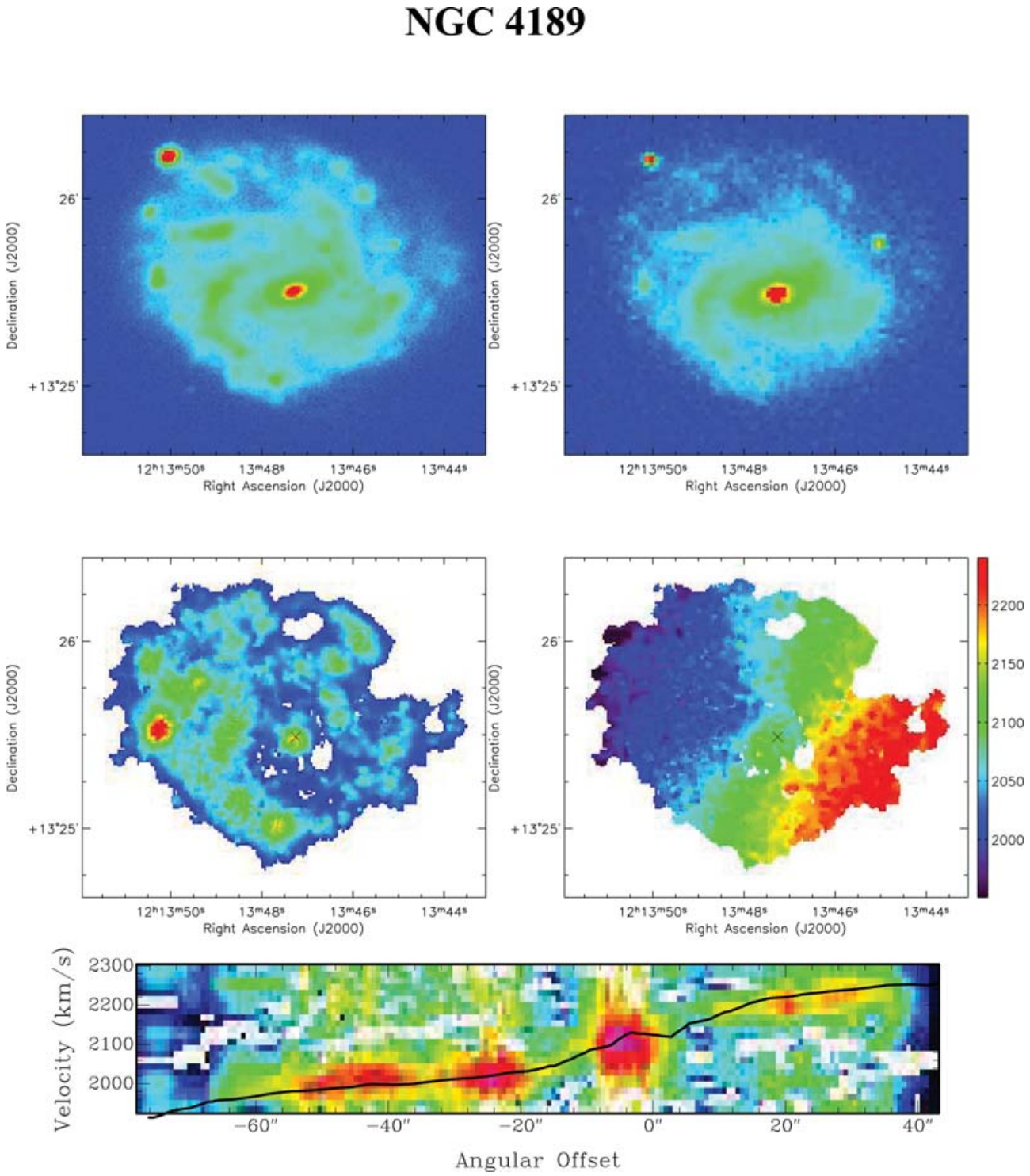

Figure A1. NGC 4189 (VCC 0089). Top: GOLDMine *B*-band (left-hand panel) and *H*-band (right-hand panel) images. Middle: FP Hα integrated map (left-hand panel) and Hα velocity field (right-hand panel). All three images of integrated intensities are displayed using a square root stretch with increasing intensity levels from blue to red colours. In the Hα flux and velocity maps, a cross gives the position of the photometric centre. The velocity field is displayed using a linear scale and are in km s^{-1}. The PV diagram is displayed using a logarithmic stretch. A solid line represents the derived rotation curve of the galaxy (see Section 4). 1 arcmin corresponds to 4.7 kpc.

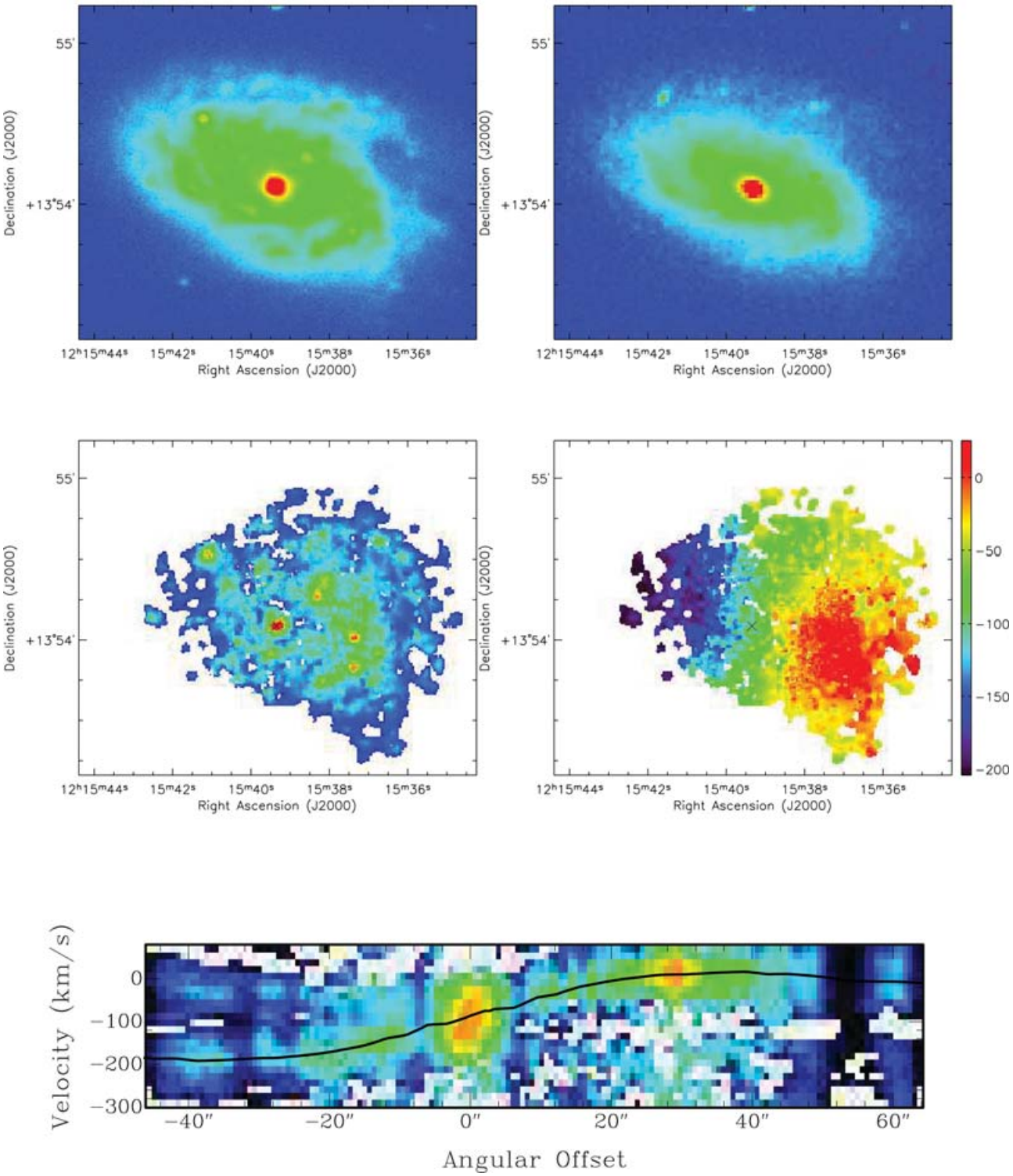

Figure A2. Same as in Fig. A1 for NGC 4212 (VCC 0157).

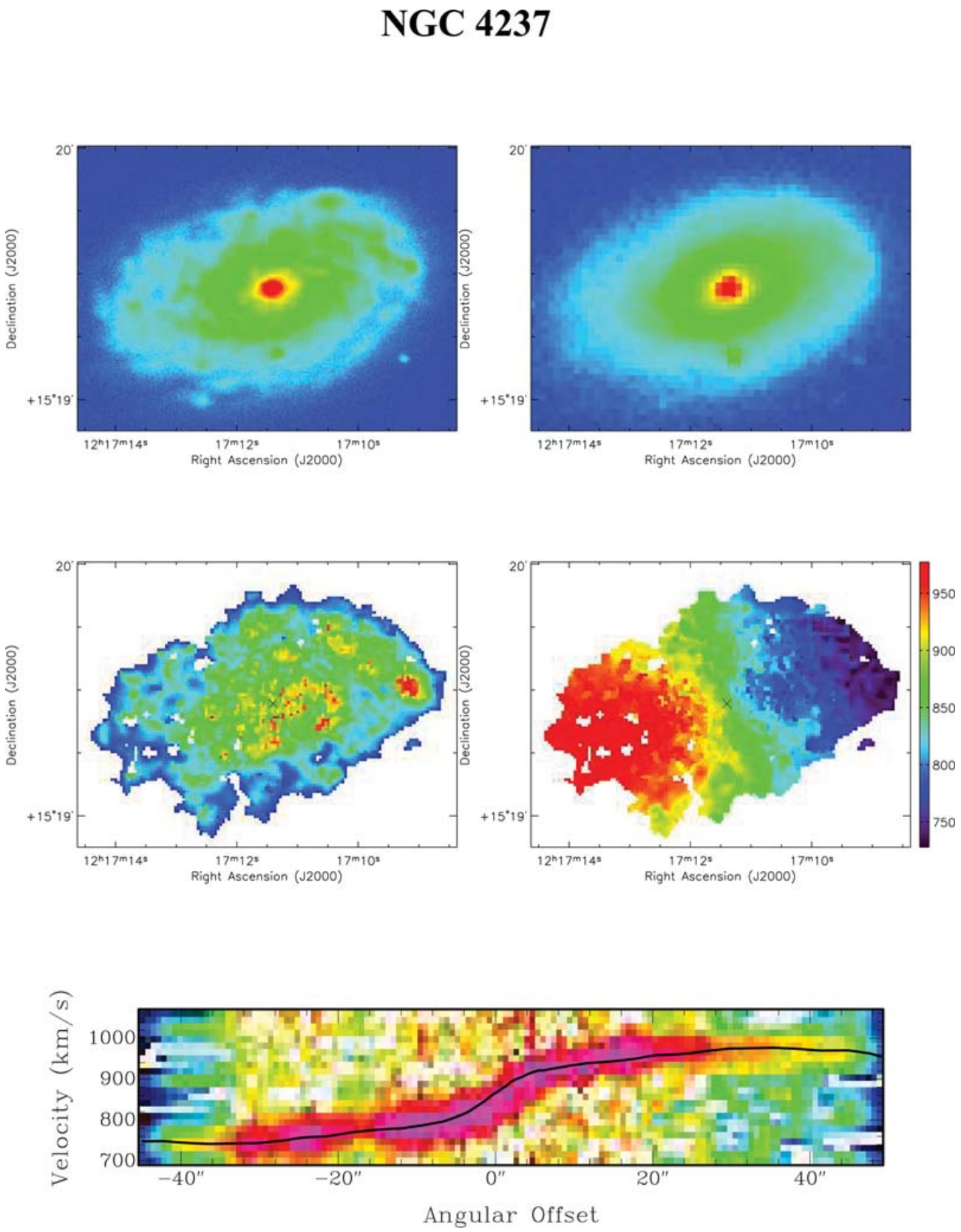

Figure A3. Same as in Fig. A1 for NGC 4237 (VCC 0226).

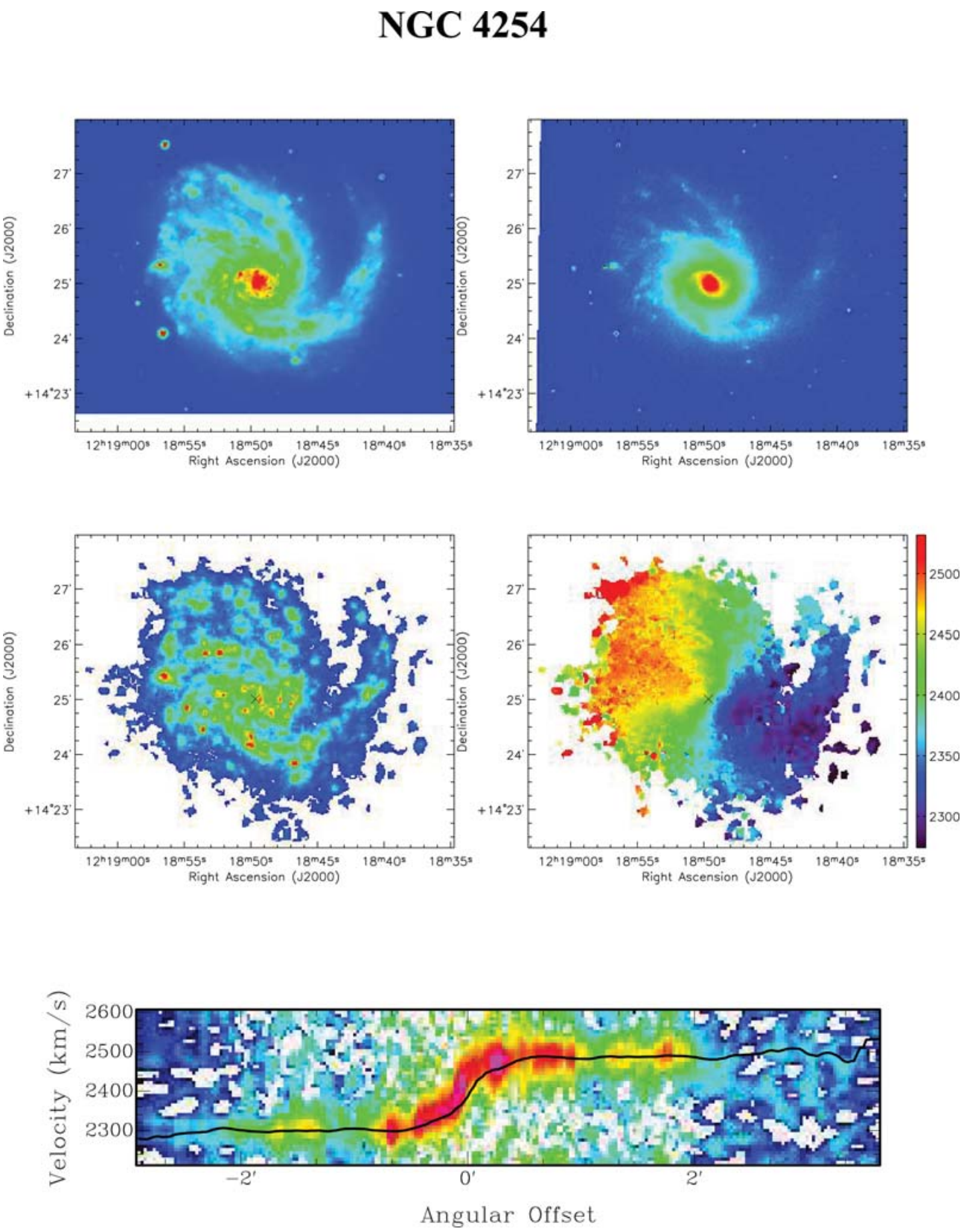

Figure A4. Same as in Fig. A1 for NGC 4254 (VCC 0307).

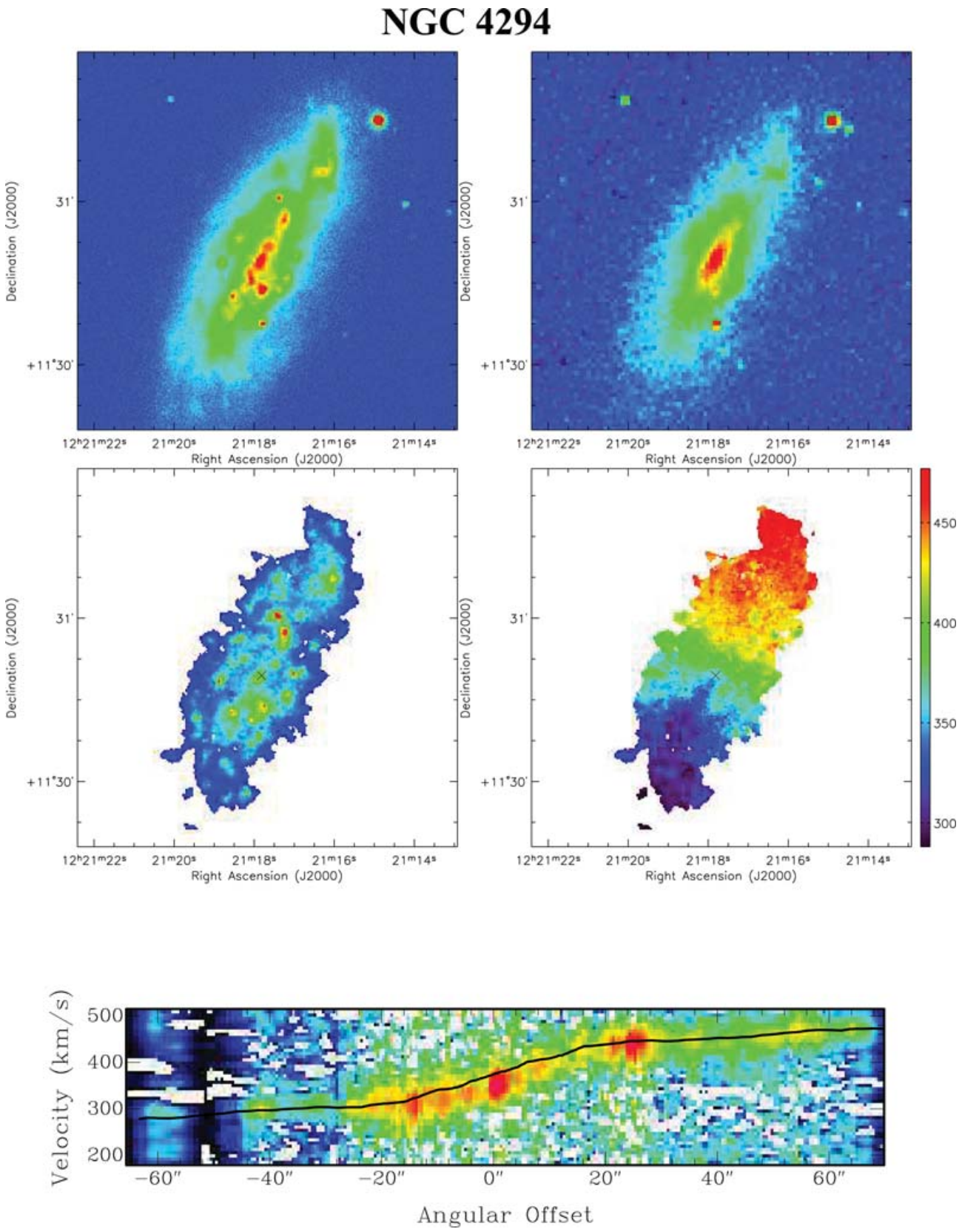

Figure A5. Same as in Fig. A1 for NGC 4294 (VCC 0465).

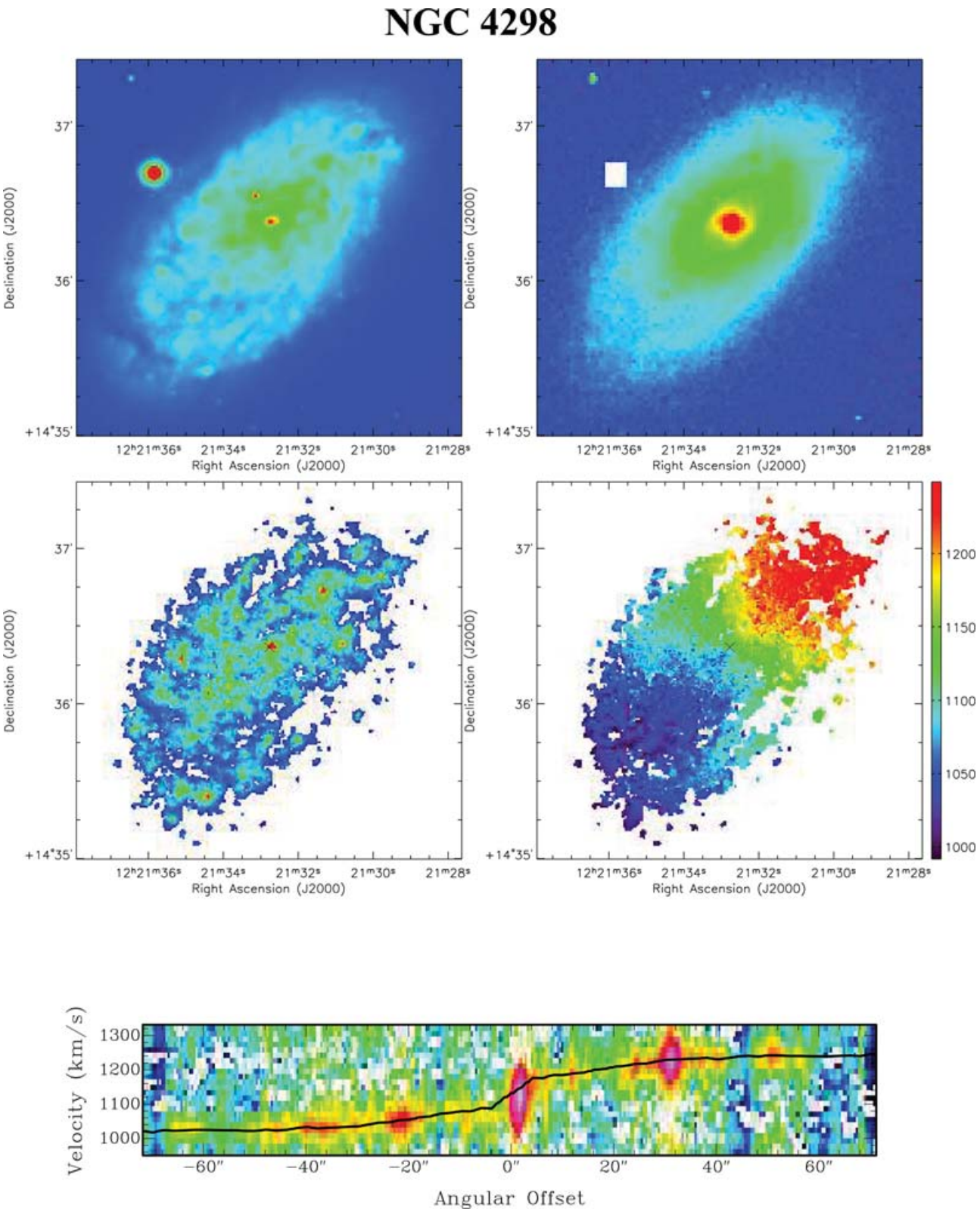

Figure A6. Same as in Fig. A1 for NGC 4298 (VCC 0483).

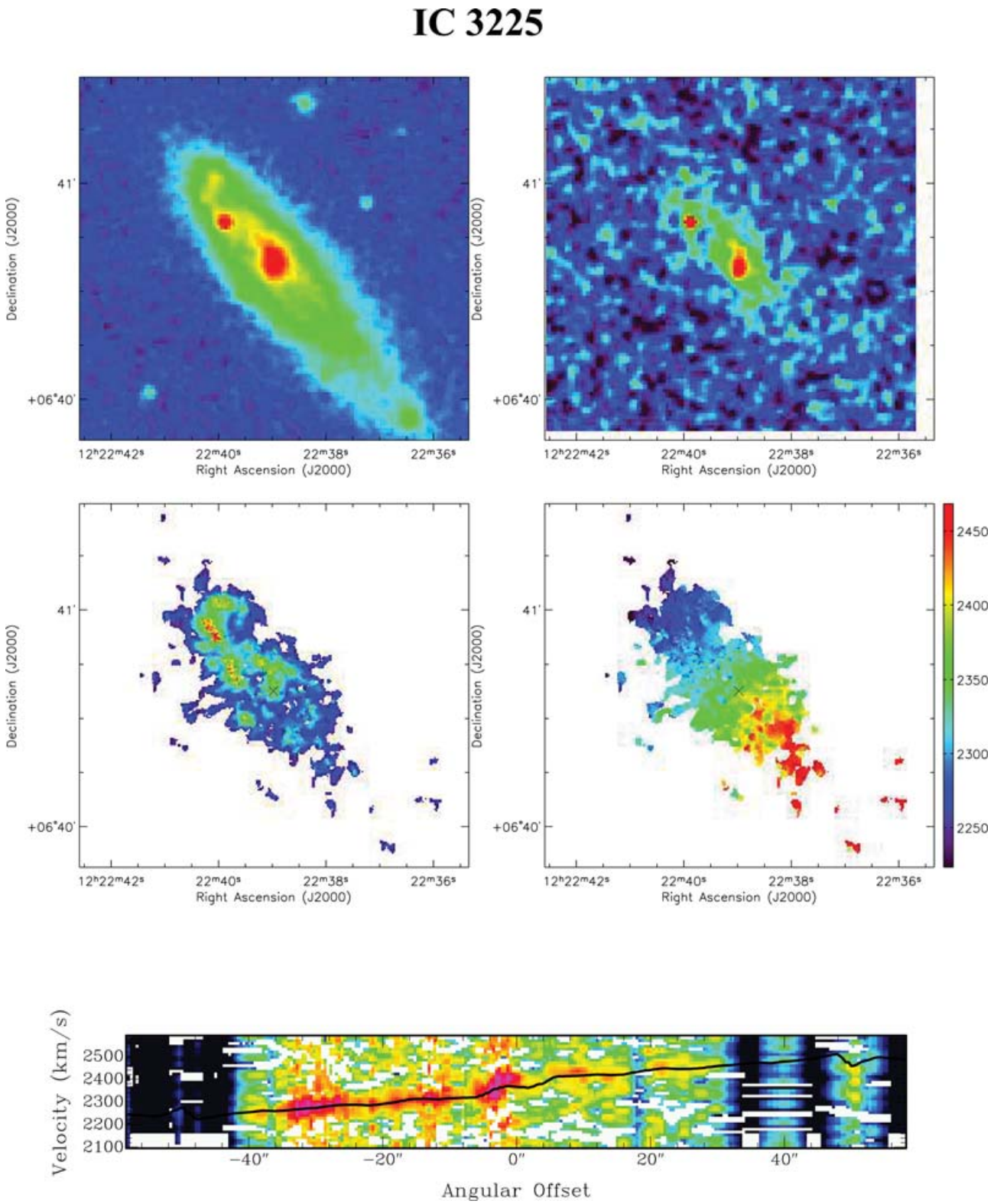

Figure A7. Same as in Fig. A1 for IC 3225 (VCC 0567). The *H*-band image is from the 2MASS data base.

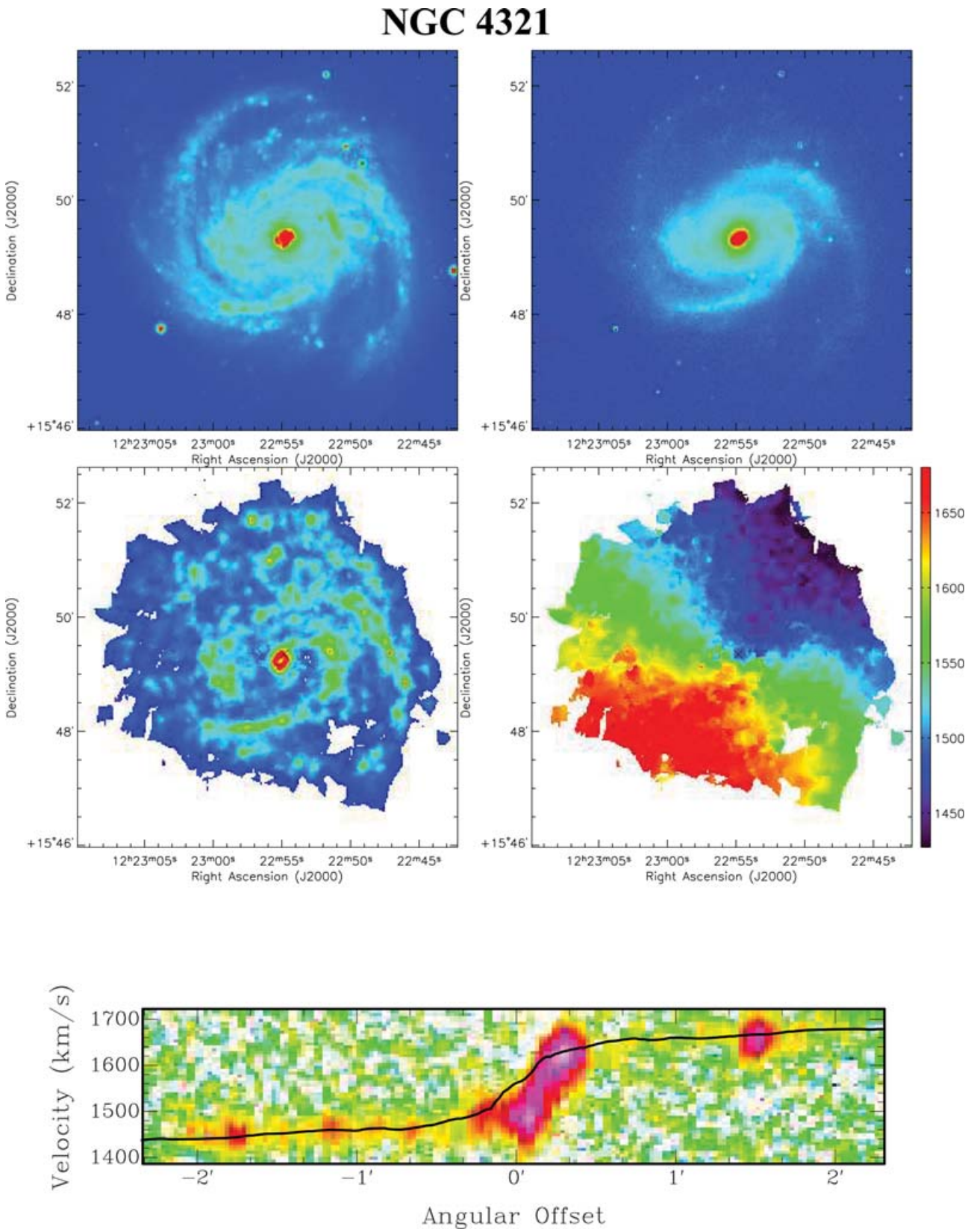

Figure A8. Same as in Fig. A1 for NGC 4321 (VCC 0596).

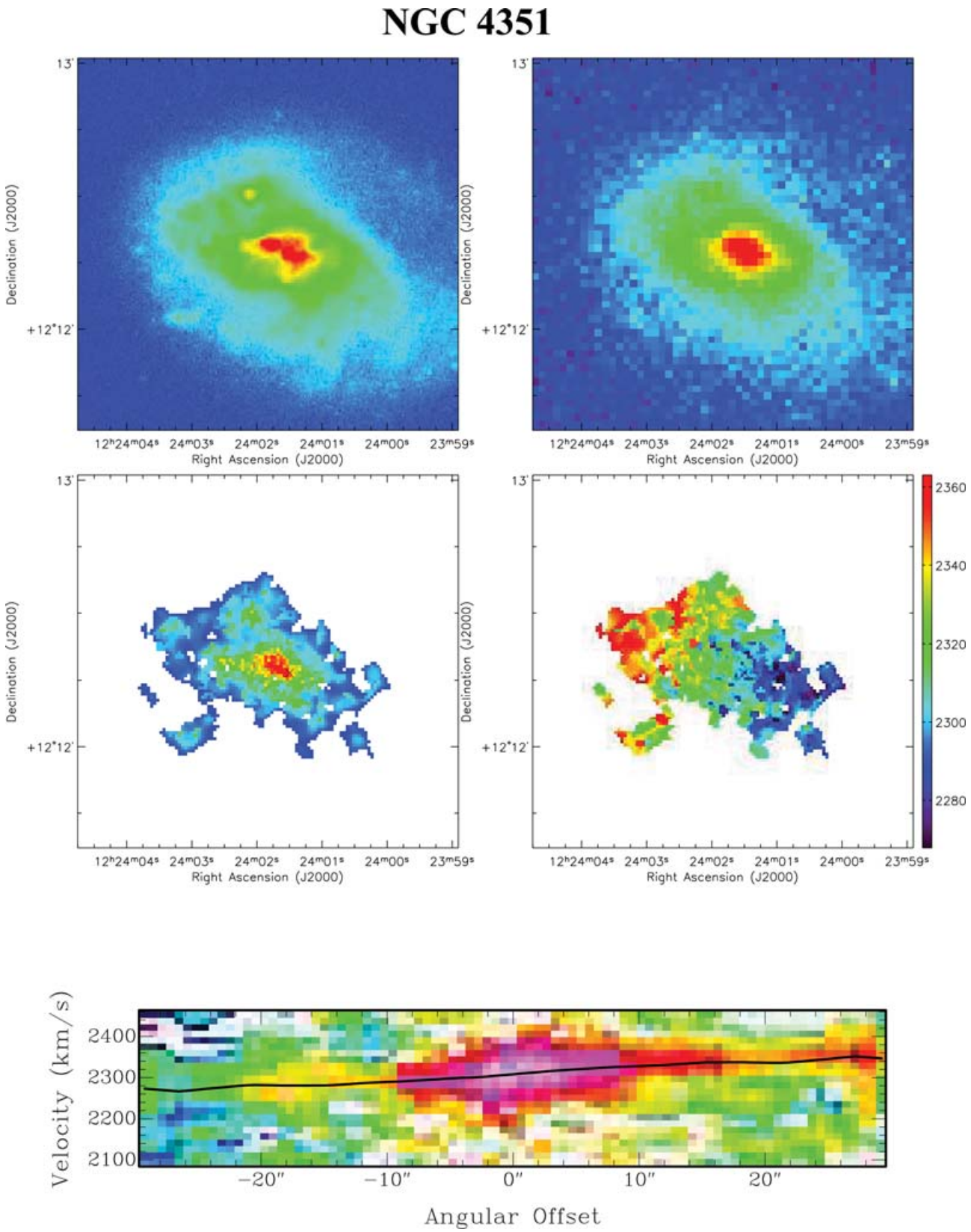

Figure A9. Same as in Fig. A1 for NGC 4351 (VCC 0692).

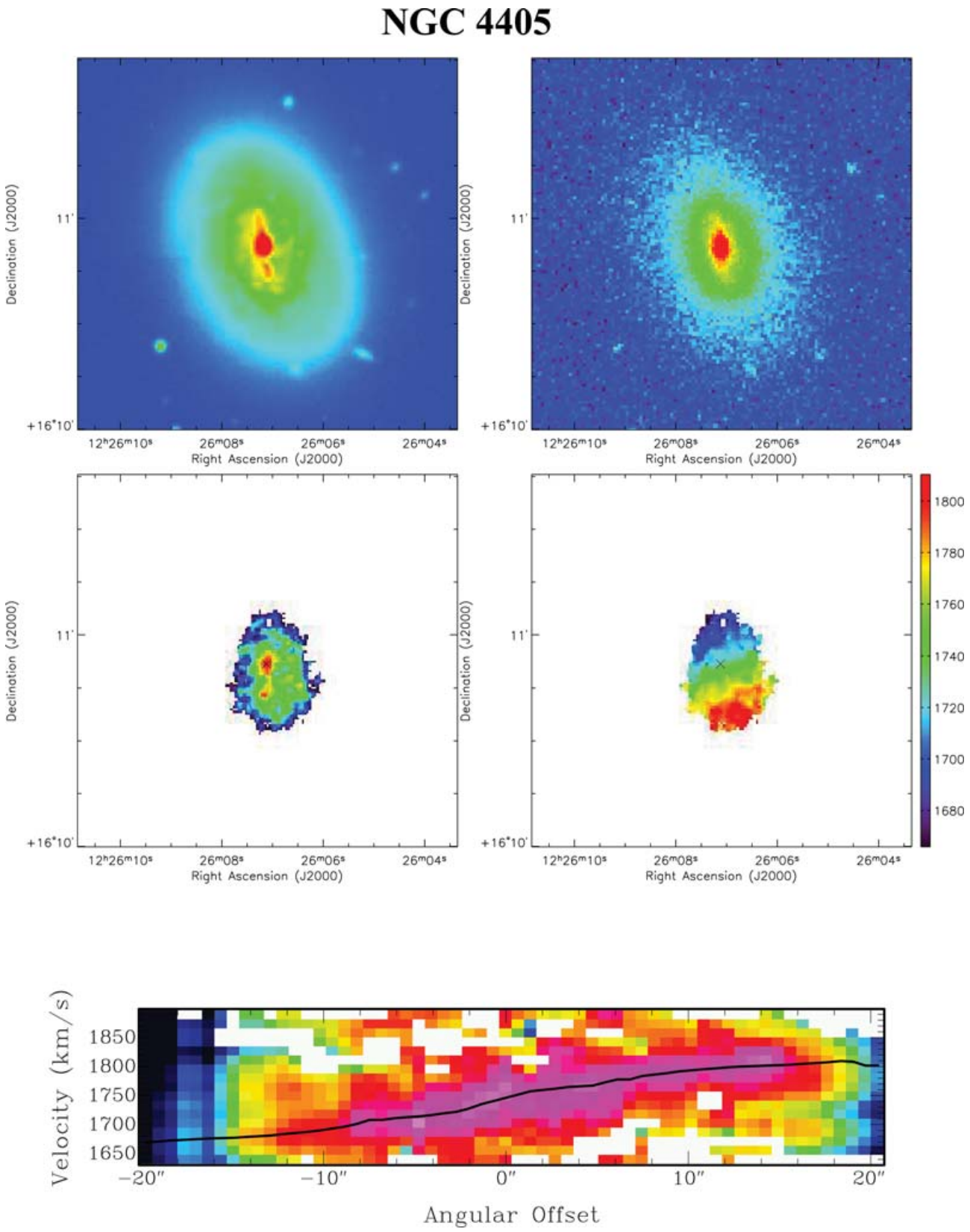

Figure A10. Same as in Fig. A1 for NGC 4405 (VCC 0874).

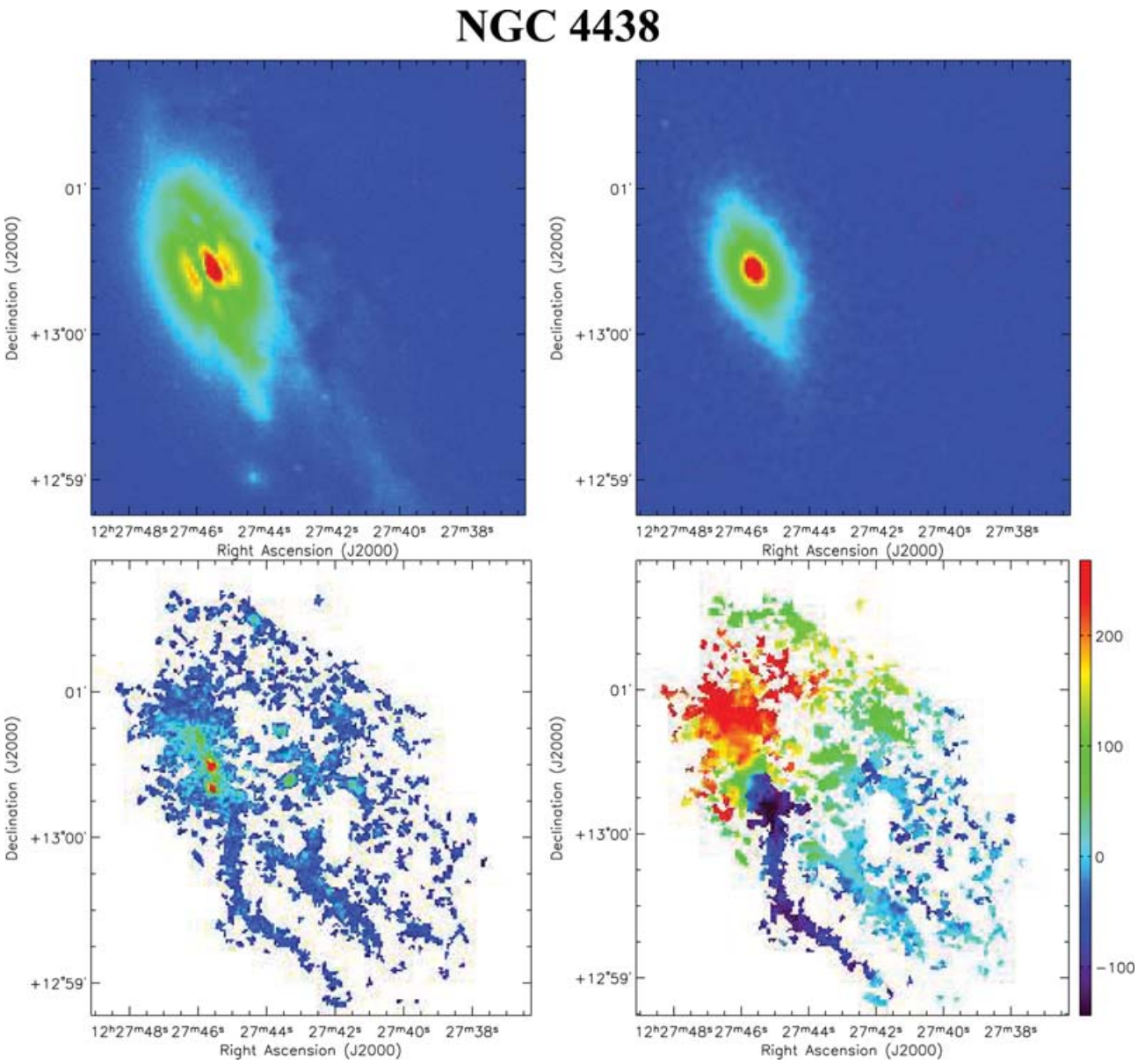

Figure A11. Same as in Fig. A1 for NGC 4438 (VCC 1043).

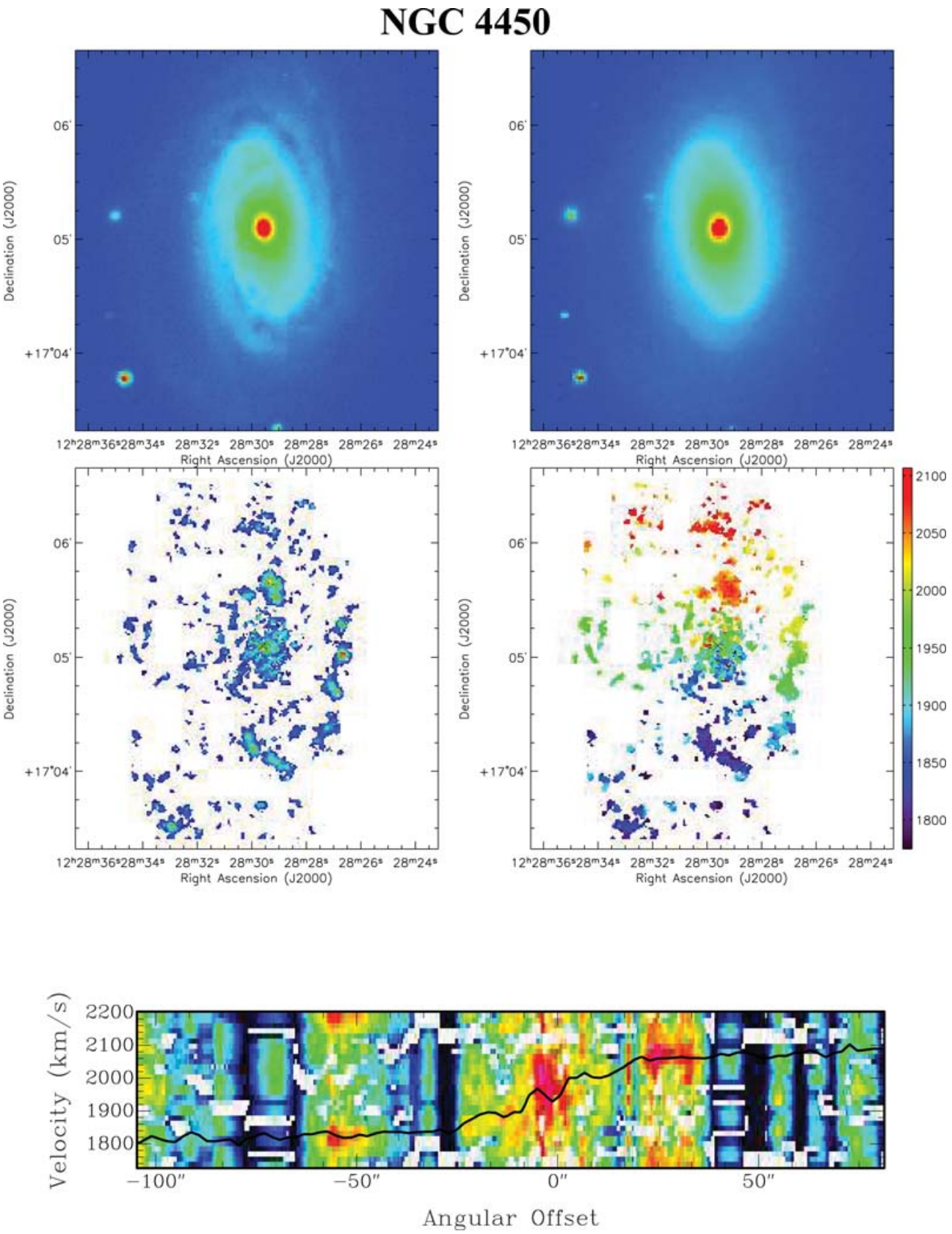

Figure A12. Same as in Fig. A1 for NGC 4450 (VCC 1110).

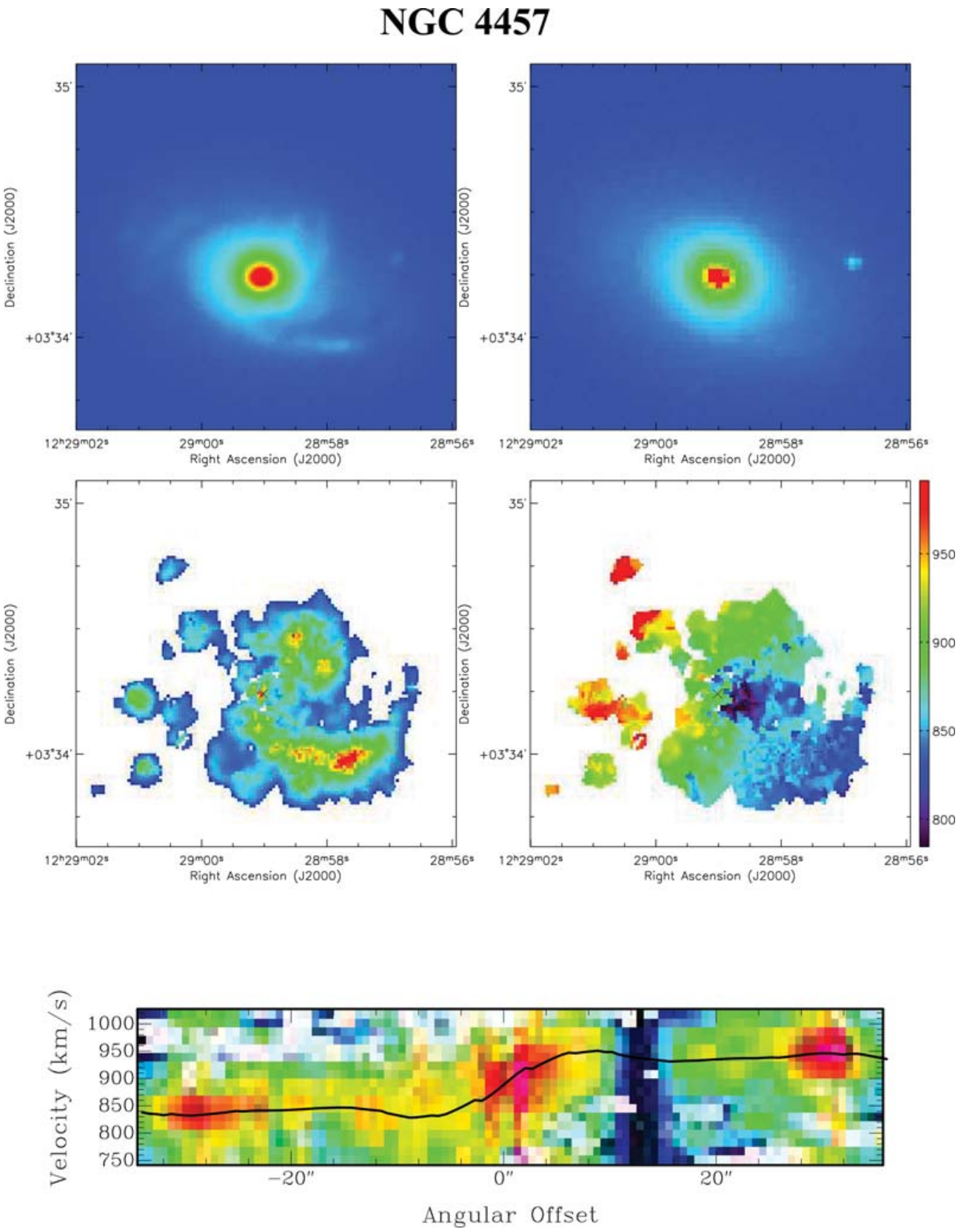

Figure A13. Same as in Fig. A1 for NGC 4457 (VCC 1145).

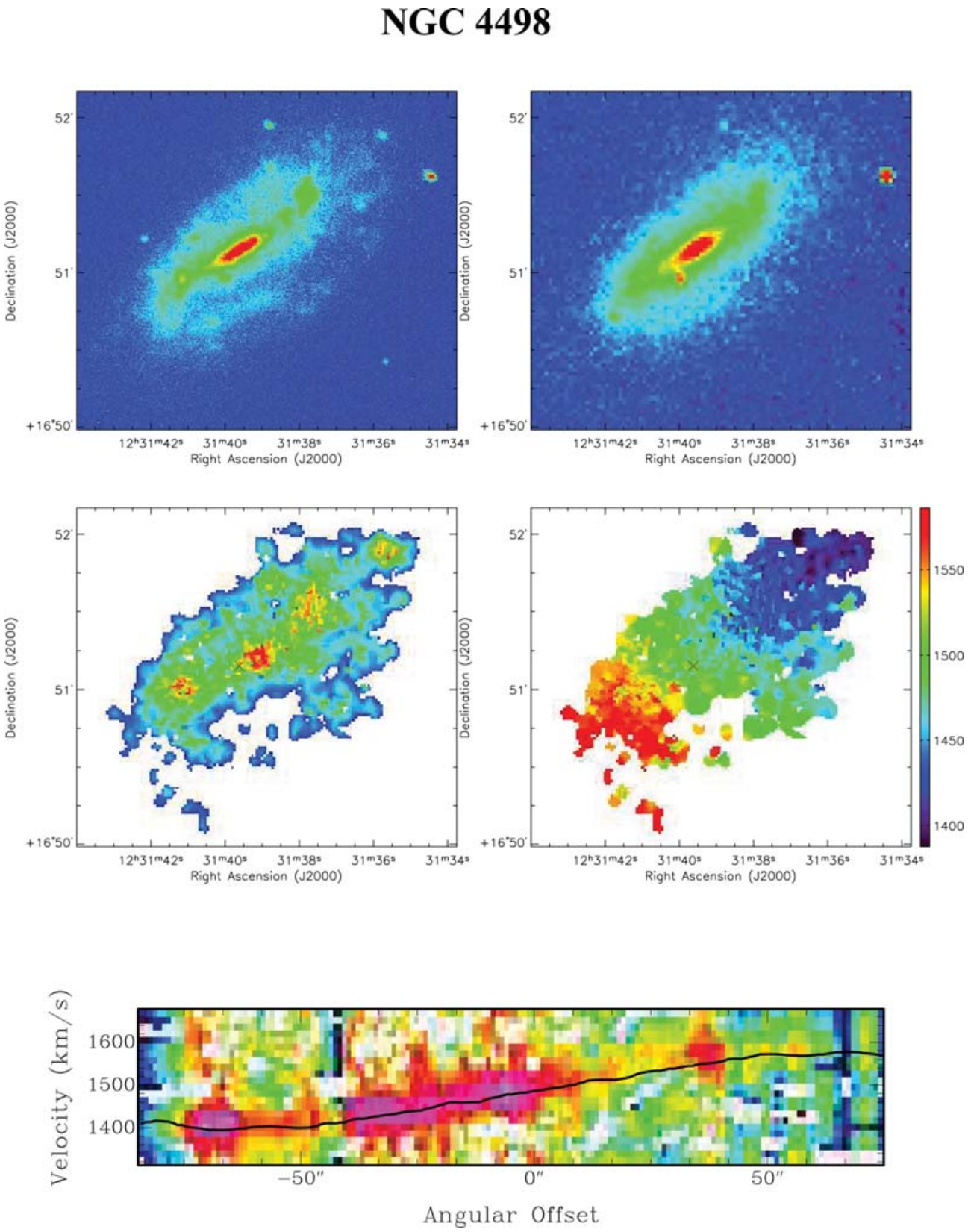

Figure A14. Same as in Fig. A1 for NGC 4498 (VCC 1379).

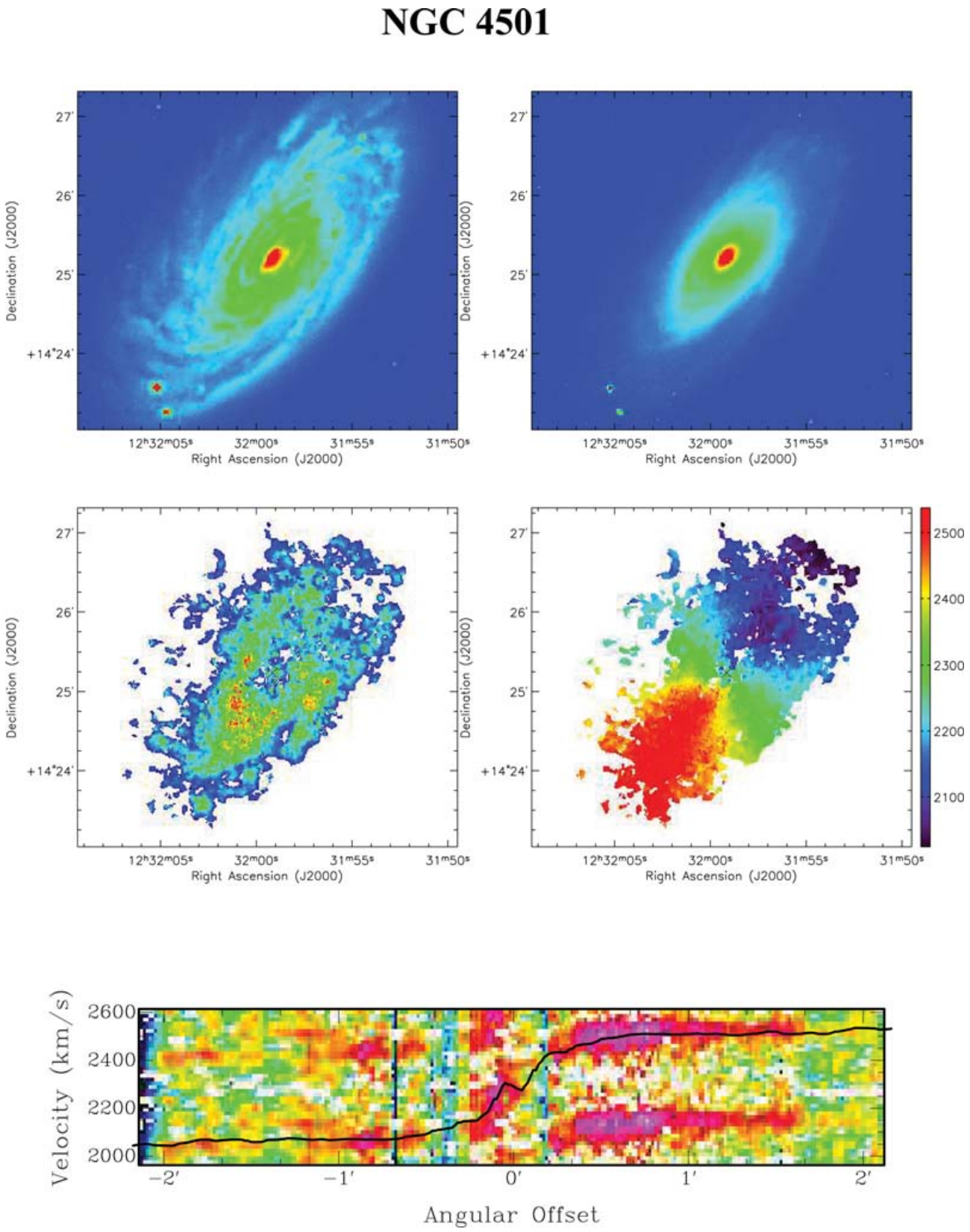

Figure A15. Same as in Fig. A1 for NGC 4501 (VCC 1401).

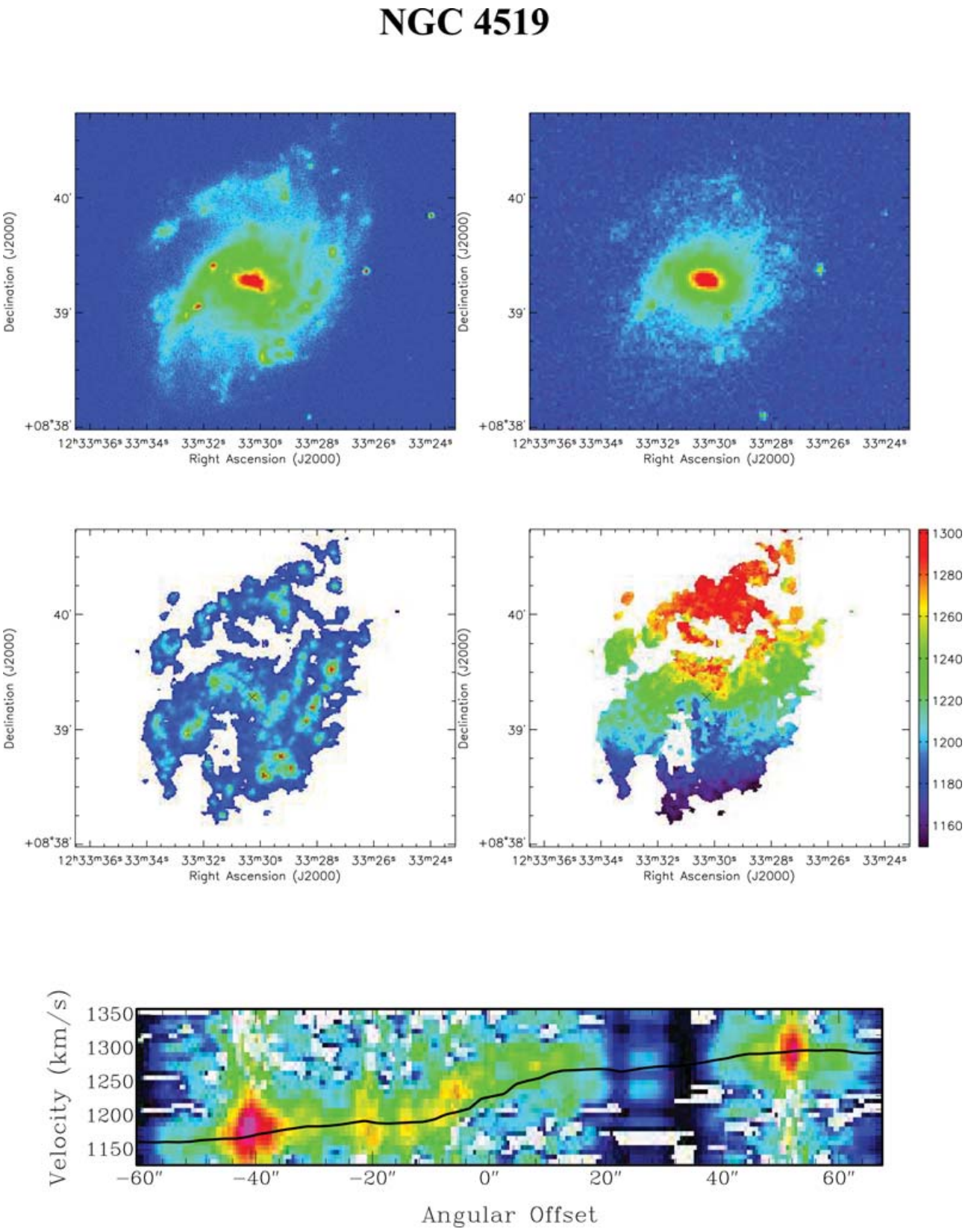

Figure A16. Same as in Fig. A1 for NGC 4519 (VCC 1508).

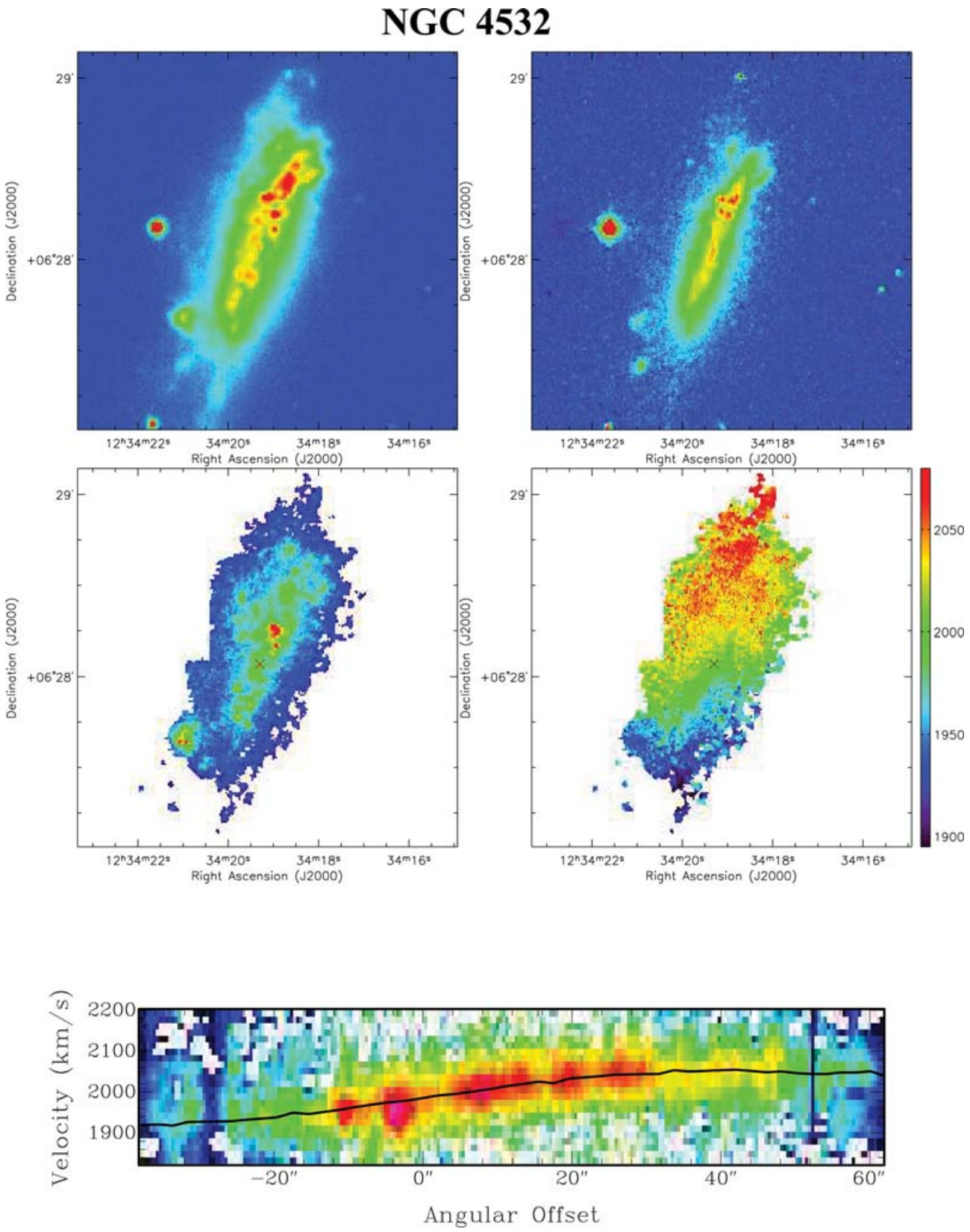

Figure A17. Same as in Fig. A1 for NGC 4532 (VCC 1554).

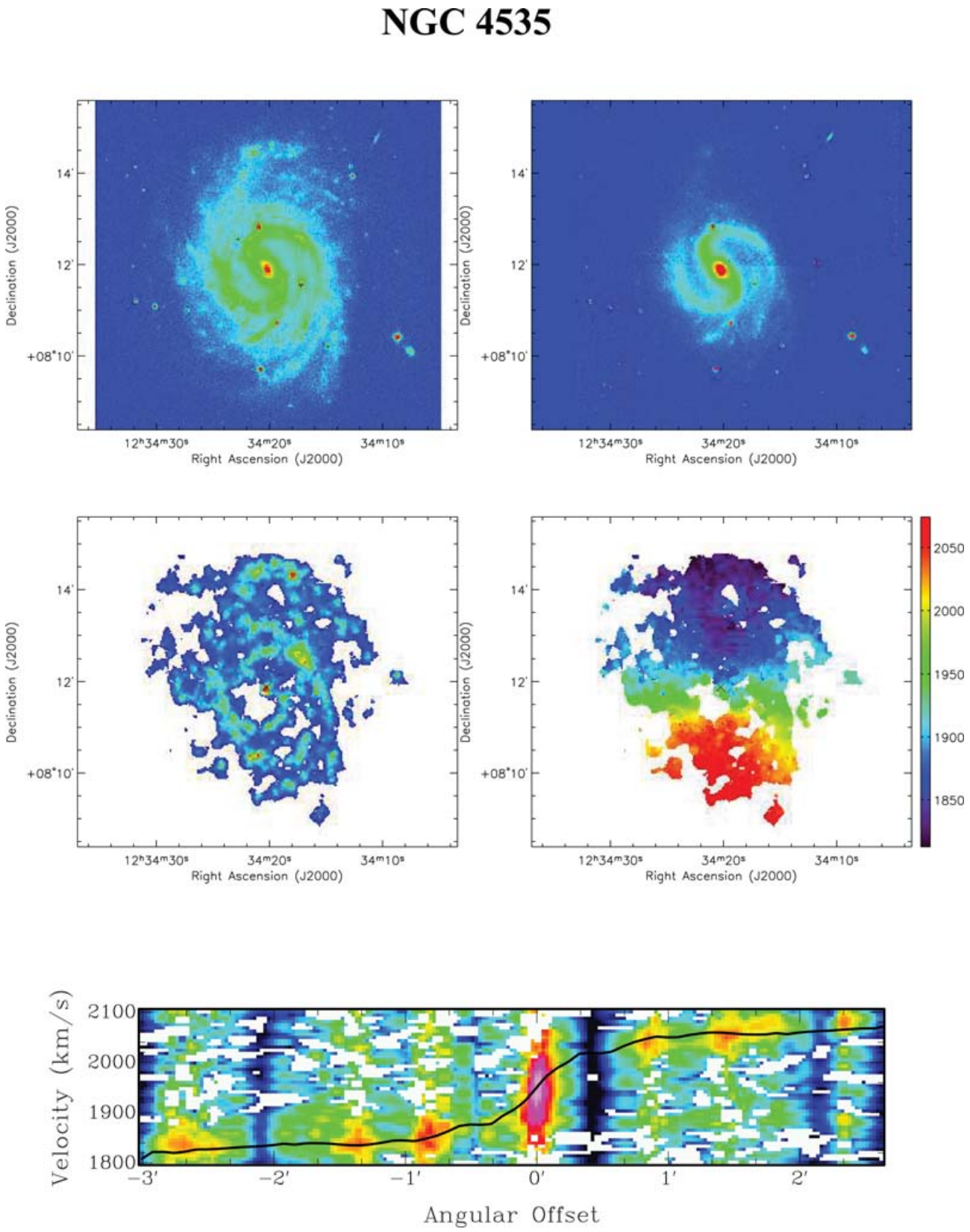

Figure A18. Same as in Fig. A1 for NGC 4535 (VCC 1555).

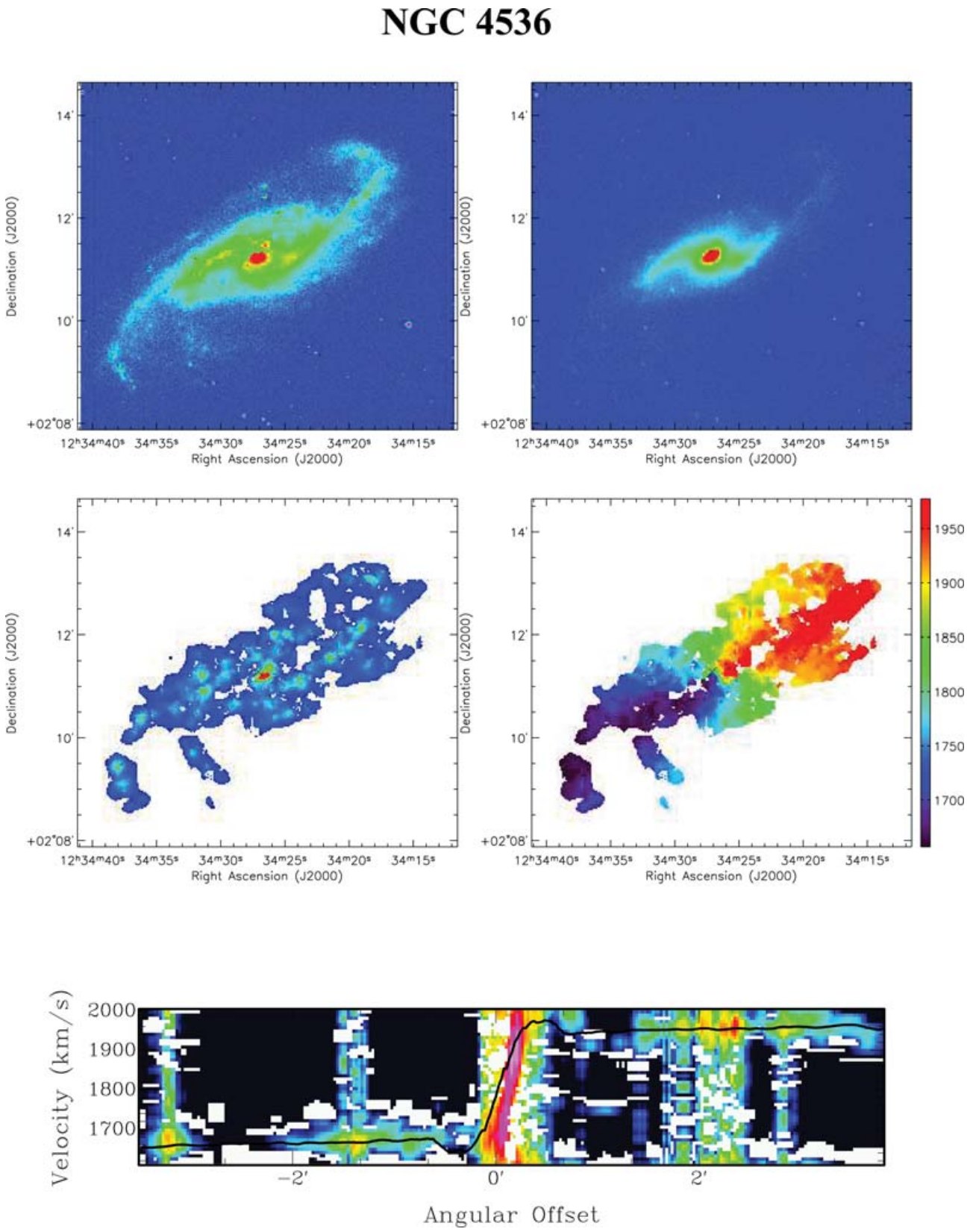

Figure A19. Same as in Fig. A1 for NGC 4536 (VCC 1562).

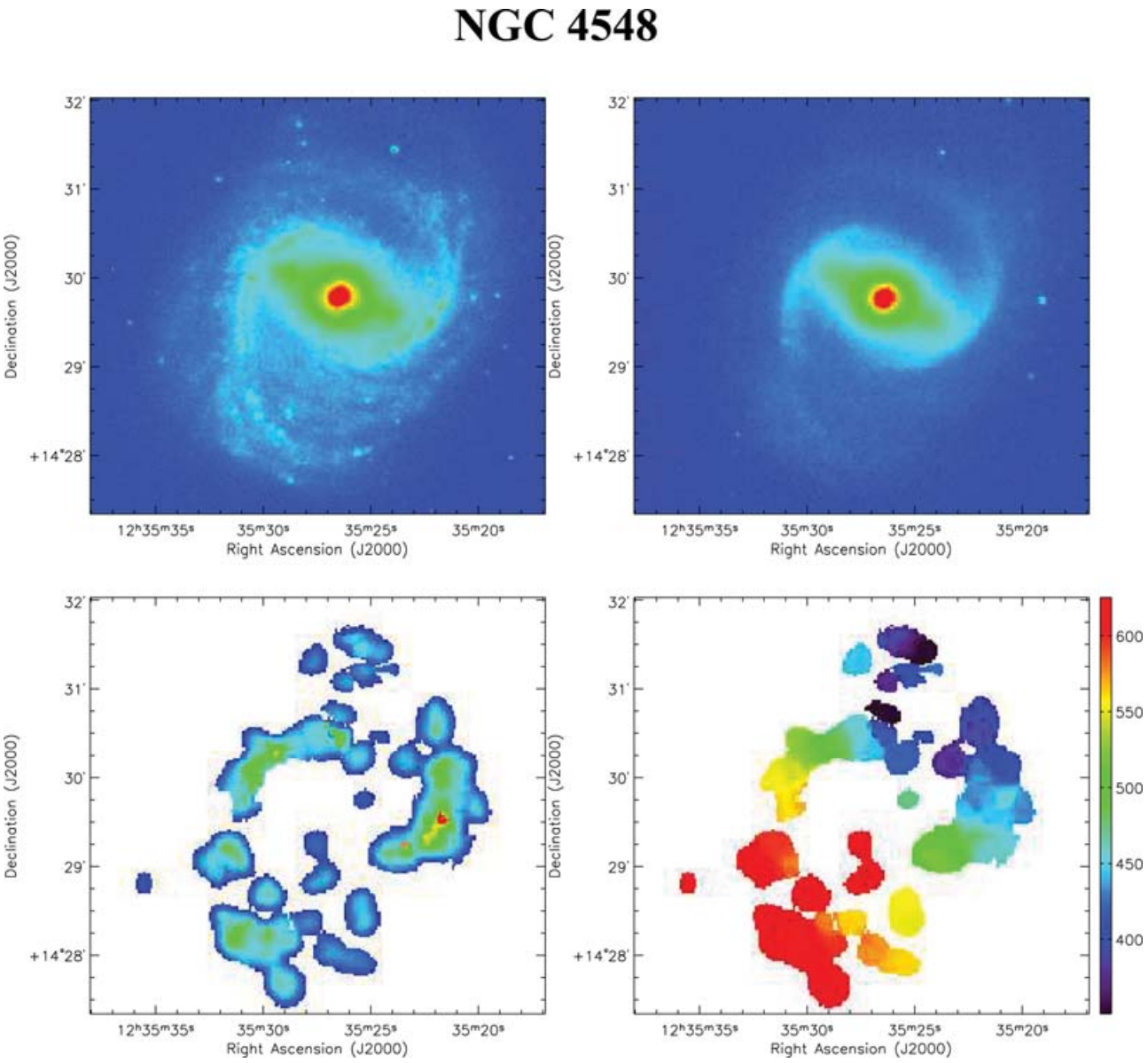

Figure A20. Same as in Fig. A1 for NGC 4548 (VCC 1615).

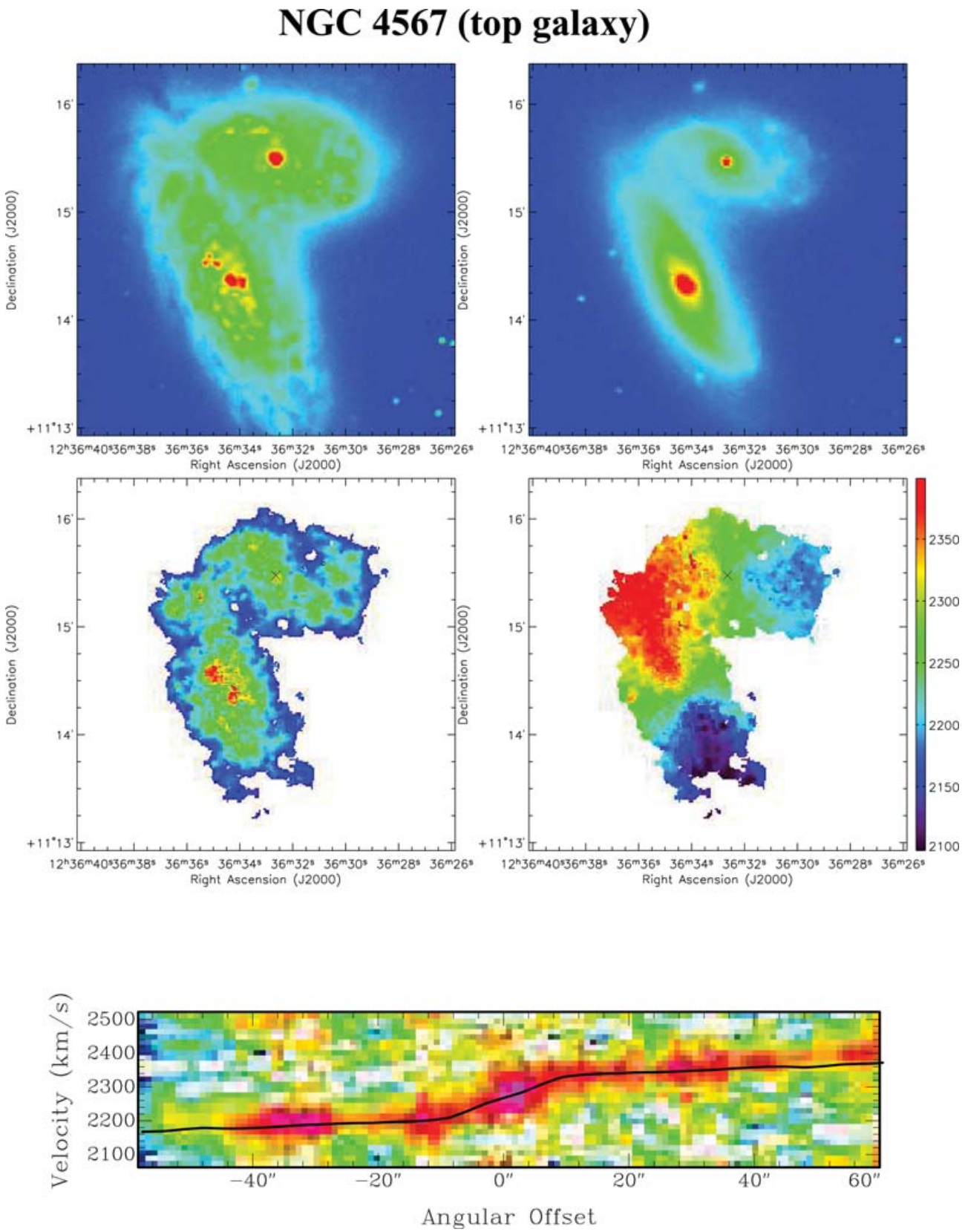

Figure A21. Same as in Fig. A1 for NGC 4567 (VCC 1673).

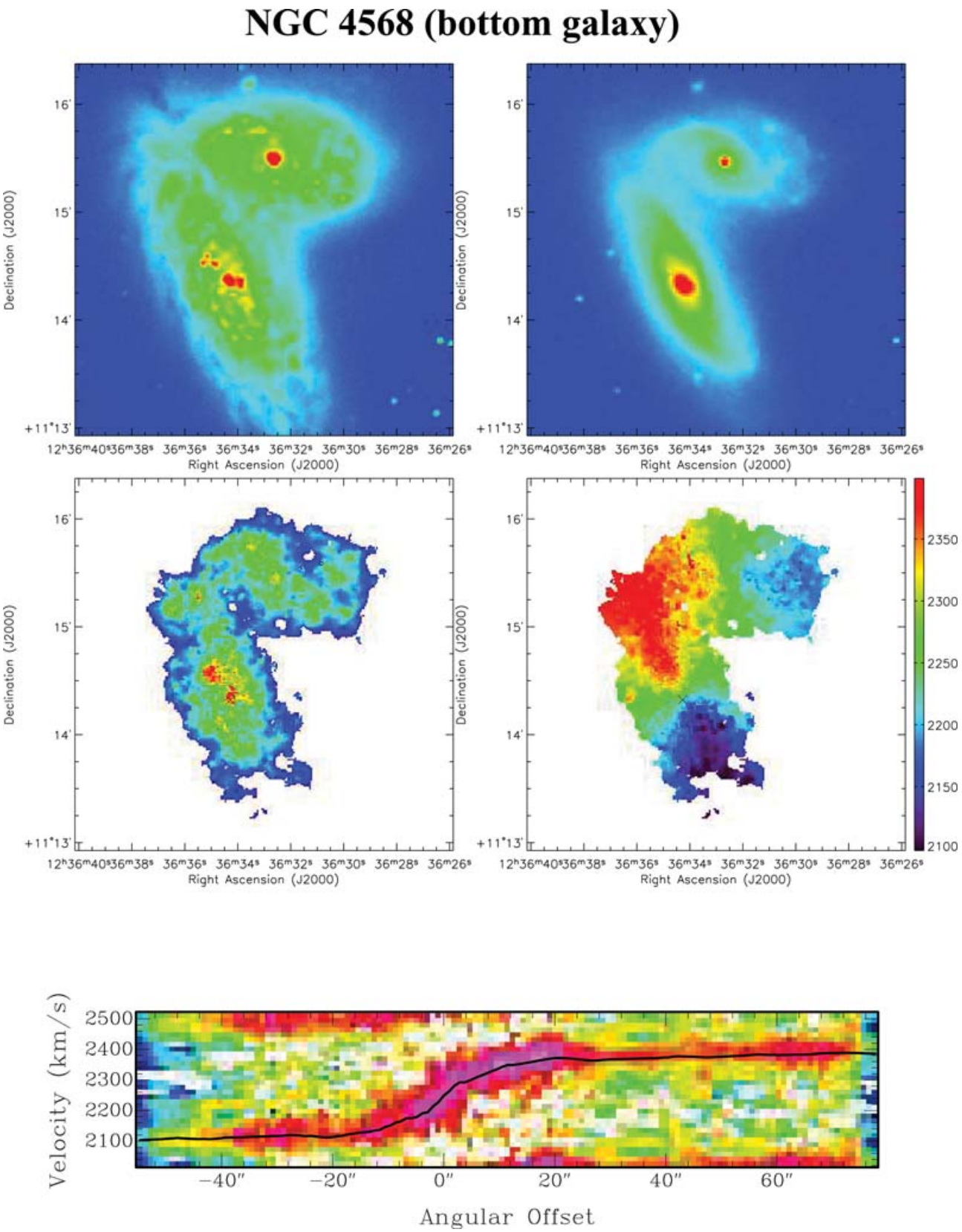

Figure A22. Same as in Fig. A1 for NGC 4568 (VCC 1676).

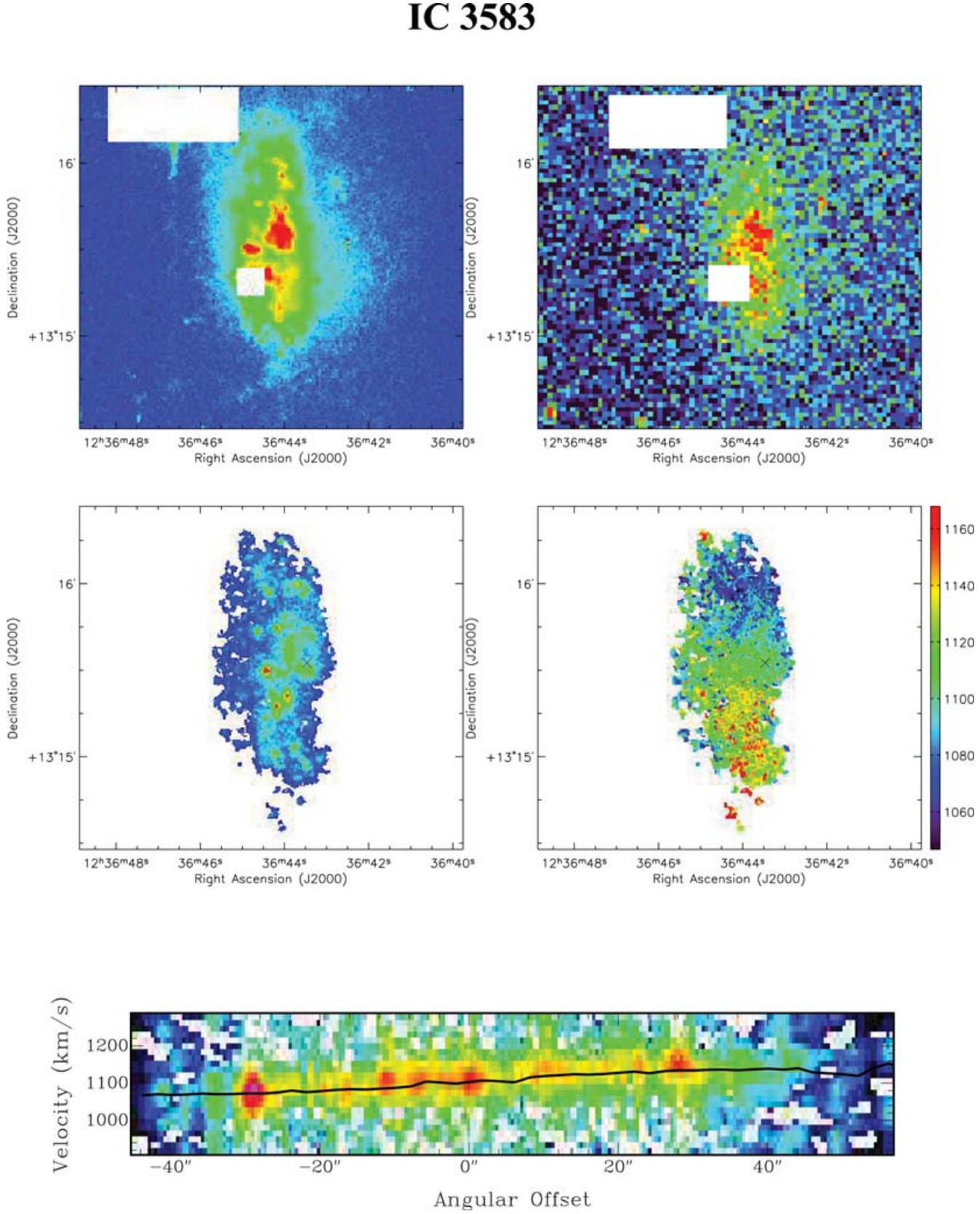

Figure A23. Same as in Fig. A1 for IC 3583 (VCC 1686).

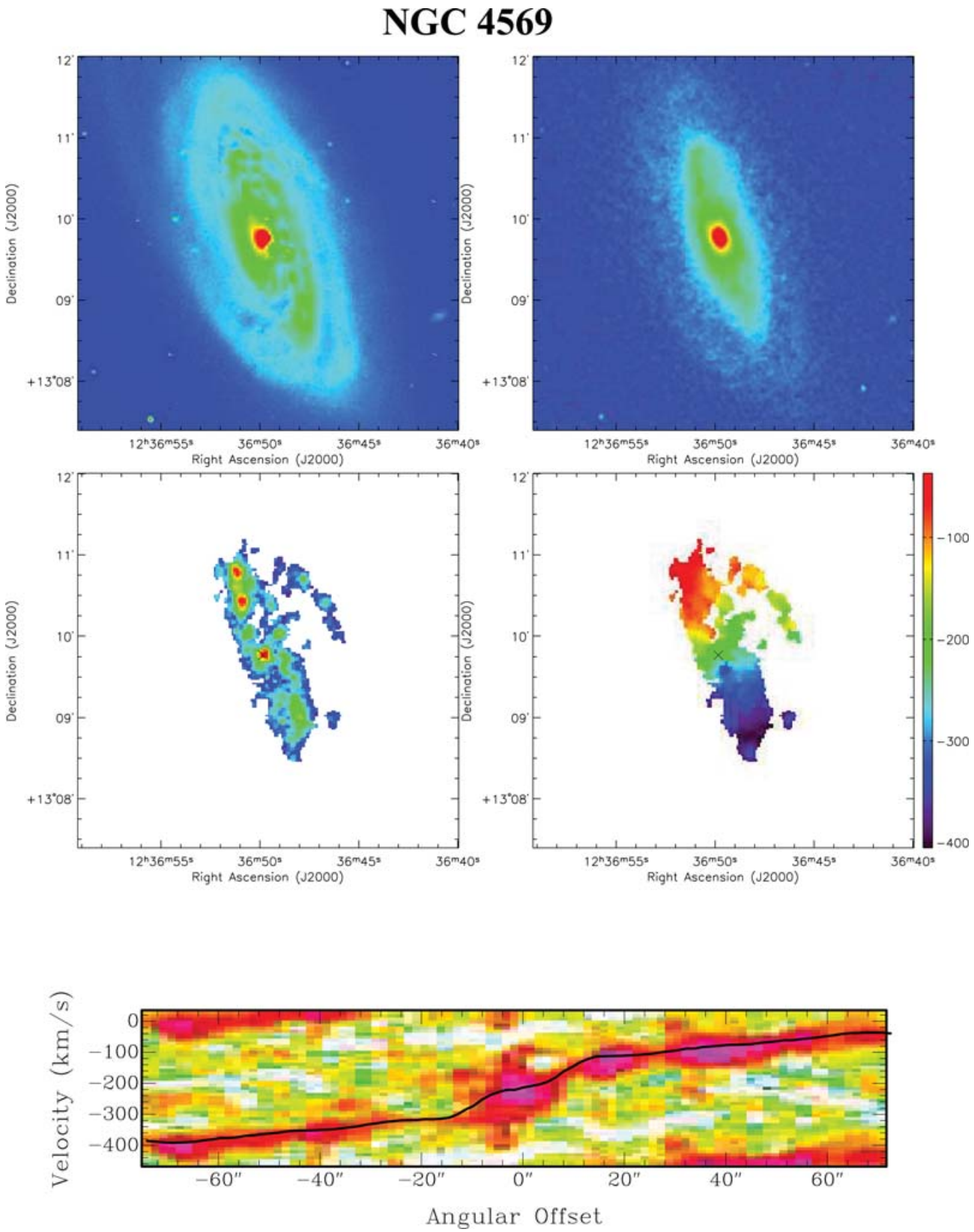

Figure A24. Same as in Fig. A1 for NGC 4569 (VCC 1690).

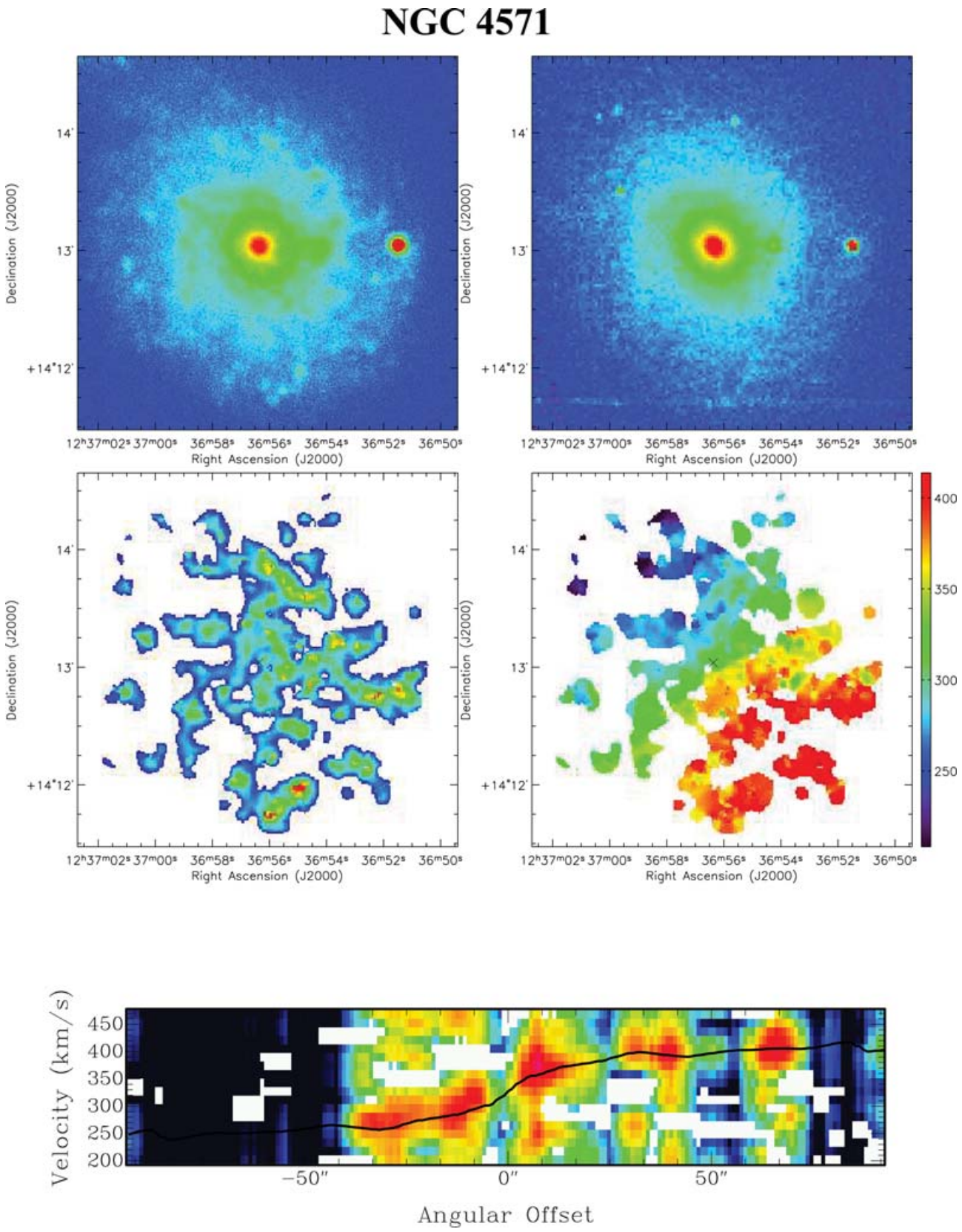

Figure A25. Same as in Fig. A1 for NGC 4571 (VCC 1696).

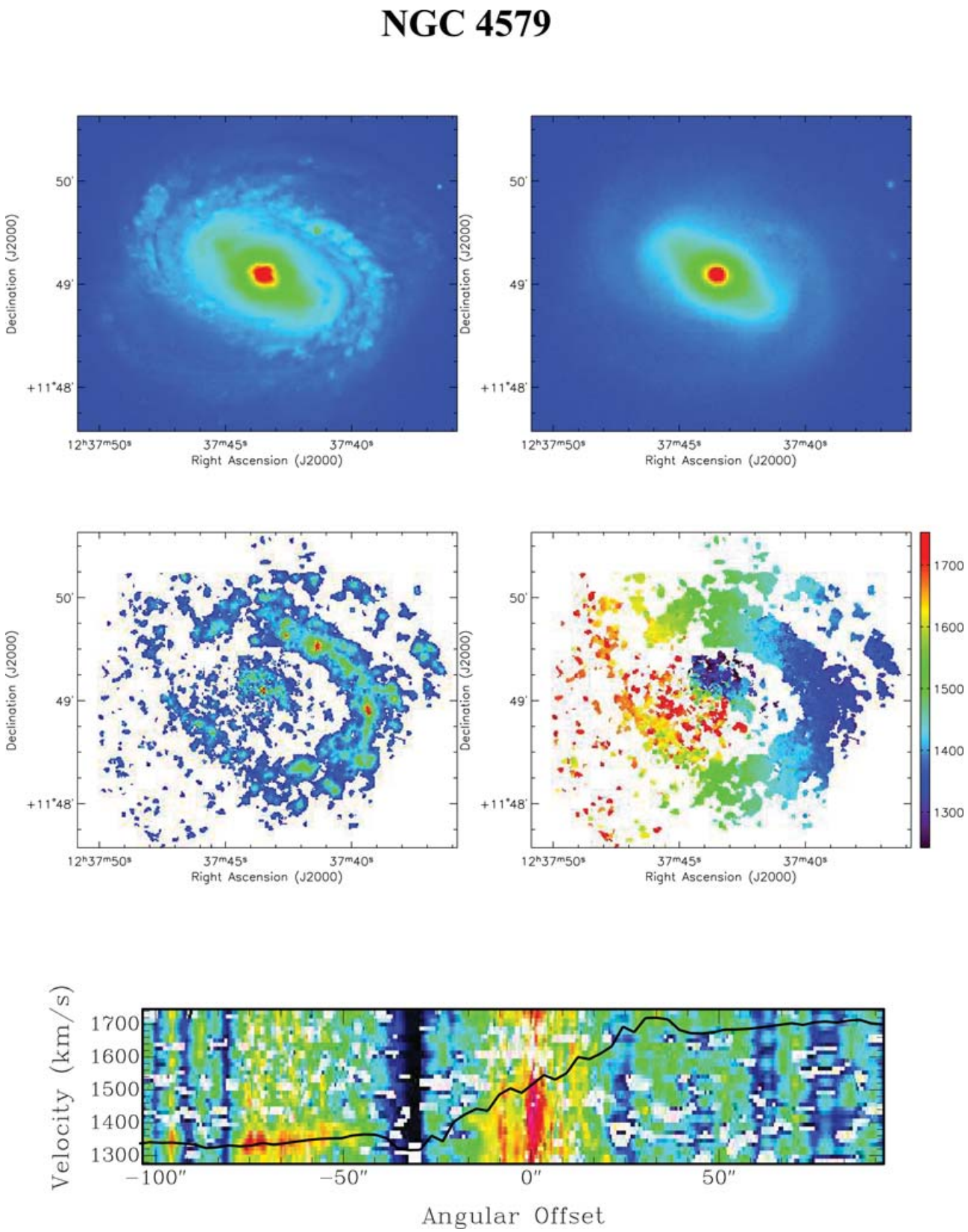

Figure A26. Same as in Fig. A1 for NGC 4579 (VCC 1727).

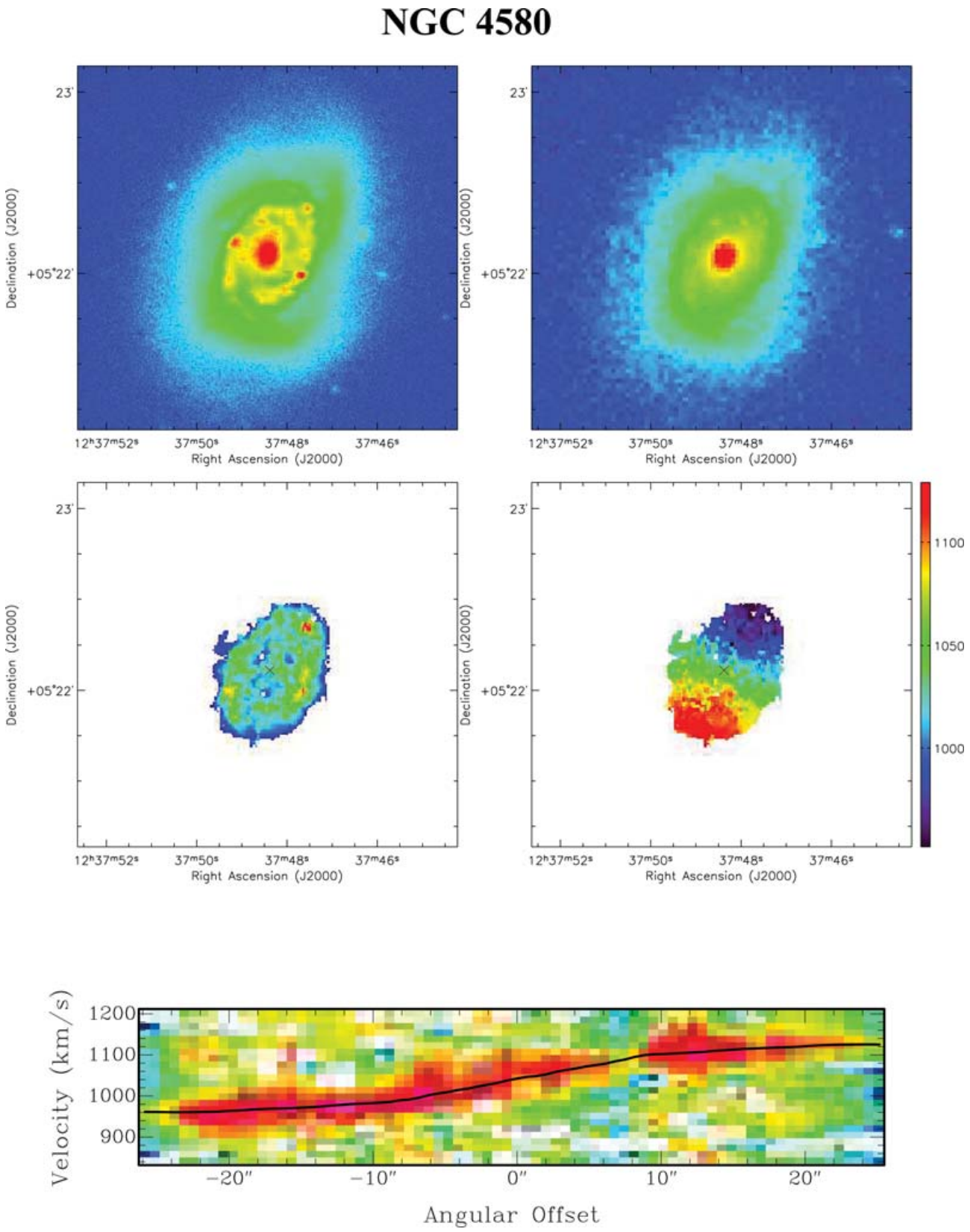

Figure A27. Same as in Fig. A1 for NGC 4580 (VCC 1730).

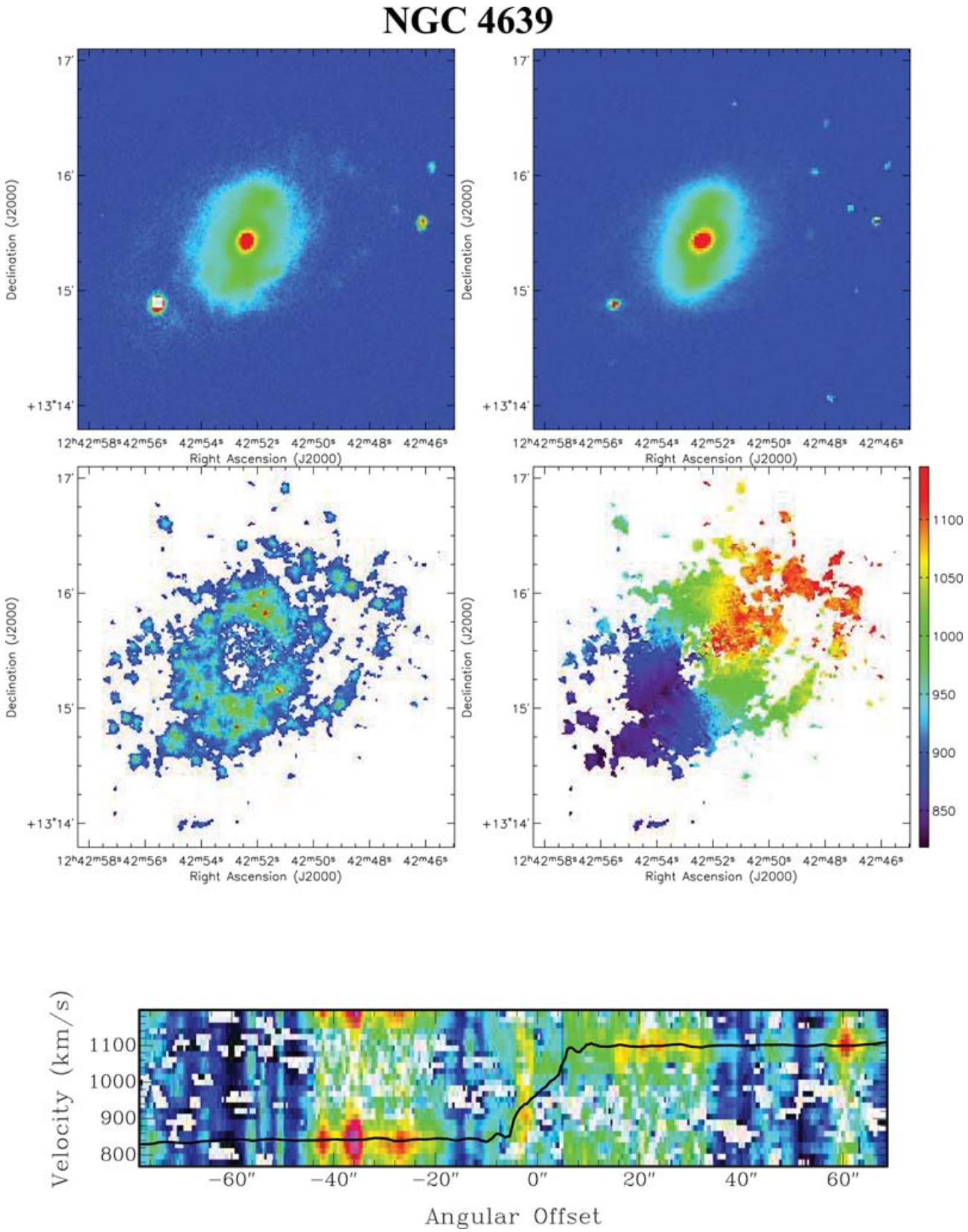

Figure A28. Same as in Fig. A1 for NGC 4639 (VCC 1943).

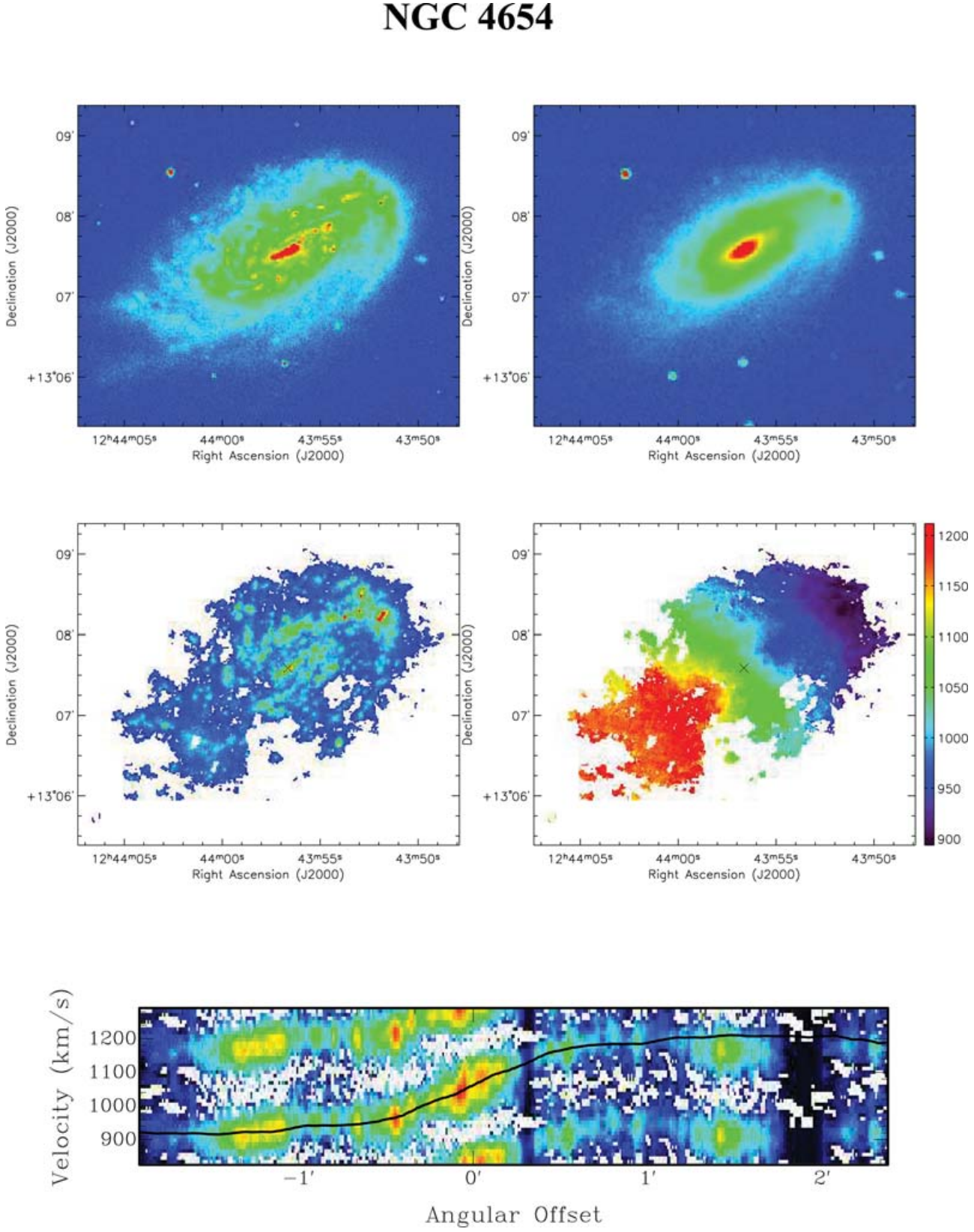

Figure A29. Same as in Fig. A1 for NGC 4654 (VCC 1987).

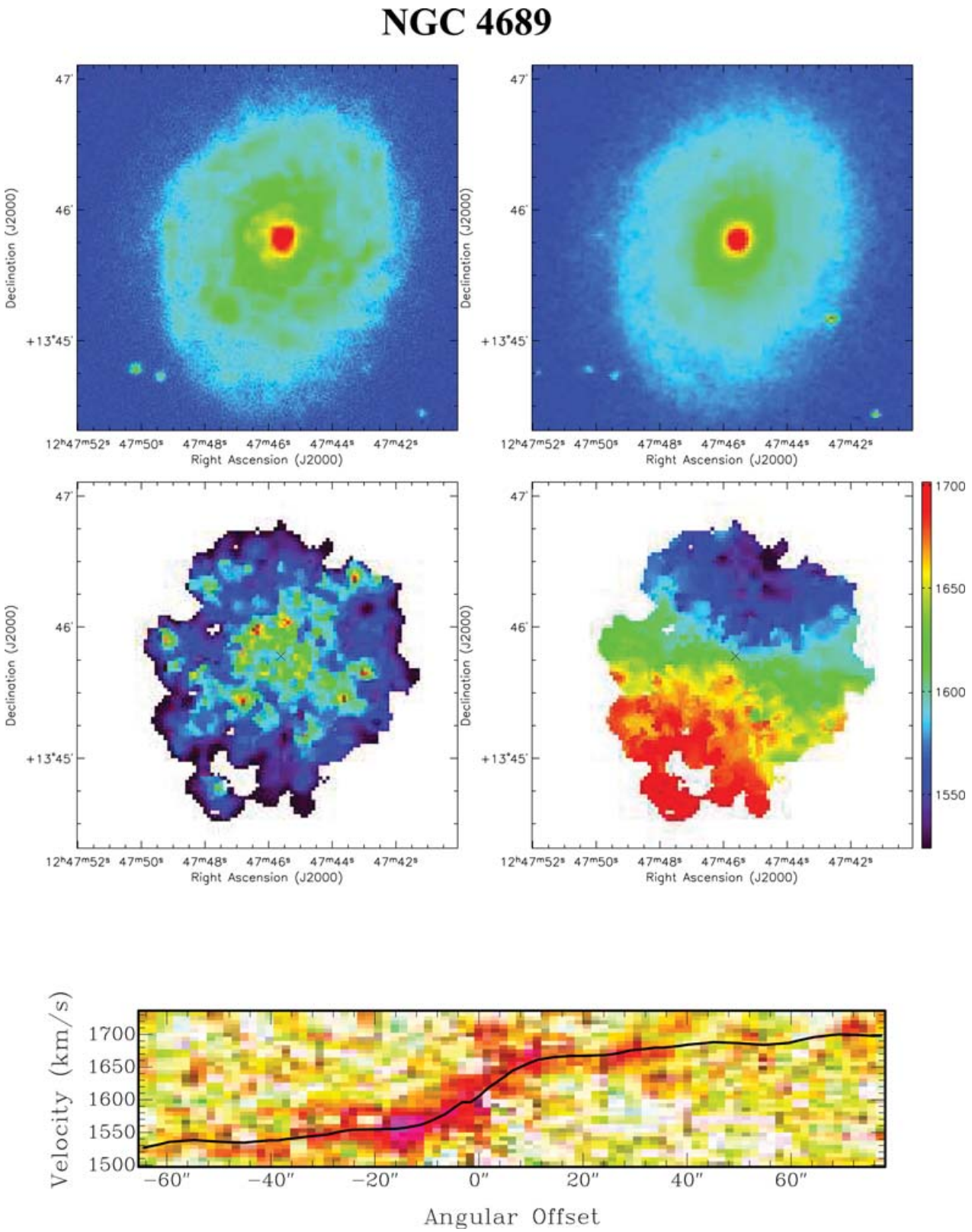

Figure A30. Same as in Fig. A1 for NGC 4689 (VCC 2058).

This paper has been typeset from a TEX/LATEX file prepared by the author.